Investigating the Effect of ZnO Modifications on the Electroluminescence Stability of Quantum-dot Light Emitting Devices and the Underlying Factors

by

Dong Seob Chung

A thesis

presented to the University of Waterloo

in fulfillment of the

thesis requirement for the degree of

Doctor of Philosophy

in

Electrical and Computer Engineering

Waterloo, Ontario, Canada, 2023

© Dong Seob Chung 2023

Examining Committee Membership

The following served on the Examining Committee for this thesis. The decision of the Examining Committee is by majority vote.

External Examiner: Adrian Kitai
Professor, Dept. of Engineering Physics,
McMaster University

Supervisor: Hany Aziz
Professor, Dept. of Electrical & Computer Engineering,
University of Waterloo

Internal Member: Siva Sivoththaman
Professor, Dept. of Electrical & Computer Engineering,
University of Waterloo

Internal Member: Youngki Yoon
Associate Professor, Dept. of Electrical & Computer Engineering,
University of Waterloo

Internal-External Member: Kevin Musselman
Associate Professor, Dept. of Mechanical & Mechatronics Engineering,
University of Waterloo

Author’s Declaration

I hereby declare that I am the sole author of this thesis. This is a true copy of the thesis, including any required final revisions, as accepted by my examiners.

I understand that my thesis may be made electronically available to the public.

Abstract

Quantum dots (QDs) have garnered significant attention as promising materials for next-generation flat panel displays due to their unique luminescence properties. These properties, such as an impressive photoluminescence quantum yield (PLQY) of nearly 100%, narrow emission spectra, and the ability to finely adjust emission wavelengths, have captured the interest of the scientific community. In comparison to state-of-the-art organic light emitting devices (OLEDs) that rely on organic emitting materials, QDs offer the potential to deliver displays with heightened color purity and significantly enhanced color saturation. This has led to endeavors to incorporate QDs into display technologies, initially starting with conventional liquid-crystal displays (LCDs) and OLED displays.

Notably, *Samsung* has introduced commercial displays that leverage QDs in color conversion layers for both LCDs and OLED displays. These implementations have contributed to improvements in color purity and color gamut. However, these devices have yet to fully harness the complete advantages of QDs. As a result, current research endeavors are centered around incorporating QDs into the emission layer of self-emissive devices, allowing them to harness their electroluminescence (EL) properties beyond their function as color conversion layers. Unlike LCDs and OLEDs, where a considerable portion of light output is absorbed by color conversion layers, QDs integrated into the emission layer of LEDs (referred to as QLEDs) offer the potential for enhanced luminance, broader color gamut, and heightened color purity due to their sharper emission spectra, all without requiring additional conversion layers.

Over the last decades, substantial efforts have been dedicated to improving QLED performance. Recent advances have resulted in device efficiencies exceeding 20% in red, green, and blue QLEDs. However, significant challenges still stand in the way of their commercialization. The critical breakthrough needed for QLED commercialization revolves around enhancing their stability. While progress has been made and potential solutions have been proposed for achieving highly stable QLEDs using specific materials and conditions, challenges persist due to the complexity of pinpointing the exact causes of device degradation under diverse external conditions during prolonged operation. Thus, a comprehensive understanding of degradation mechanisms and the factors that limit device lifespan remains imperative.

The central focus of this thesis is twofold: first, to highlight a notable enhancement in QLED stability through novel modification techniques applied to the ZnO electron transport layer (ETL); and second, to unravel the degradation mechanisms intrinsic to QLEDs and the constraints imposed by the ZnO ETL. The overarching goal of this research effort can be summarized in two main objectives:

A. Explores novel approaches for altering the ZnO to improve device stability. This involves two primary approaches: (i) incorporating polymer additives into ZnO to modulate charge distribution within the QLED, and (ii) using chemical treatments, involving plasma and wet processes, to manipulate stoichiometry and defect

distribution in the ZnO, addressing issues related to oxygen vacancies and charge trap states.

B. Explores how the introduced modifications to the ZnO layer influence device stability. This entails examining the effects of different additives within the ZnO ETL on overall device performance. Various investigative techniques are employed, encompassing aspects such as charge distribution estimation, analysis of charge carrier accumulation and annihilation within the QLED, probing recombination centers, measurement of exciton lifetime, and evaluation of the chemical and electronic states of materials.

This research centers on ZnO modifications achieved through the integration of a ZnO-polyethylenimine nanocomposite (ZnO:PEI), ZnO treated with carbon tetrafluoride plasma (FZnO), and ZnO infused with iodine and ferric chloride (I_2:ZnO and $FeCl_3$:ZnO). These modifications represent innovative pathways to bolster the electroluminescence stability of QLEDs. Through extensive investigation, two primary mechanisms responsible for enhancing device stability emerge:

1. ZnO:PEI and FZnO modifications impact charge distribution and electron concentration across the QLED, mitigating the accumulation of holes at the interface of QDs and the hole transport layer (HTL). The typical scenario in QLEDs involves holes accumulating at this interface, which can lead to device degradation. Experimental measurements, including delayed electroluminescence and transient

photoluminescence measurements under bias, capacitance-voltage-luminance analyses, and electroluminescence characteristics assessments involving luminescent marking layers, collectively demonstrate that ZnO:PEI and FZnO treatments lead to an increased presence of electrons at the QDs/HTL interface, thus decreasing hole accumulation and consequently enhancing device stability.

2. The incorporation of I_2 and $FeCl_3$ into the ZnO ETL suppresses the formation of positively charged ZnO species during QLED operation. This is corroborated through X-ray photoemission spectroscopy (XPS) studies and an analysis of changes in electroluminescence and photoluminescence characteristics. These investigations reveal that extended QLED operation leads to a higher concentration of ZnO species with oxidative states, and a direct correlation between the magnitude of electroluminescence loss and the concentration of these species is established. Ultimately, the application of halide treatment to ZnO materials demonstrates its potential for enhancing the stability of green, blue, and red QLEDs alike.

Acknowledgements

Professor Hany Aziz, I would like to express my deepest gratitude to you. You have been, like, a rock-solid pillar of support for me during my time in Canada. I consider you to be *Father in Canada*. You have been supporting me, inspiring me, providing me with great advice, and keeping me motivated. I really appreciate for your embracing of all my behaviors, sometimes picky or peculiar ones. Thank you for everything.

I would like to present my appreciation to committee members: Professor Siva Sivoththaman, Professor Youngki Yoon, and Professor Kevin Musselman for valuable feedbacks and advice to my research work.

I would like to present my appreciation to all the current and past group members: Dr. Hyeonghwa (Cristina) Yu, Dr. Tyler Davidson-Hall, Dr. Mozhgan Sadeghianlemraski, Peng Wang, Fatemeh Samaeifar, Atefeh Ghorbani Koltapeh, Junfei Chen and Mohsen Azadinia, for their productive discussions and critics. I would also like to acknowledge Mr. Richard Barber and Dr. Czang-Ho Lee, for their dedications and valuable technical supports during my experiments.

During my PhD study in Canada, tennis became a significant part of my life. It provided a much-needed break when I was exhausted and often inspired and provided ideas for both my personal life and experiments. I am grateful to my tennis friends, many names that come to mind as I write this. Thanks to exercising together, I have been able to maintain both my work productivity and my physical and mental well-being.

I also want to thank to all my friends in South Korea. You folks always make me get a lot of giggles.

Lastly, I want to express my heartfelt appreciation for the unconditional love and support from my family: my beloved parents (Hyung Keun Chung and Chung Hee Park), my aunt (Wonkeun Chung), and my brother (Yoseob Chung). Despite being more than 10,000 km away, I always felt at home because of your unwavering love and support. Your love recharged my energy. Thank you for always being there for me, no matter what. And I am certain that my grandparents would be proud of me in *Heaven*.

Dedication

To anyone interested in my PhD work and journey.

Table of Contents

Examining Committee Membership.....ii

Author's Declaration.....iii

Abstract.....iv

Acknowledgements.....viii

Dedication.....ix

List of Figures.....xiv

List of Tables.....xx

List of Abbreviations.....xxi

Chapter 1 Introduction.....1

1.1 Introduction to Display Technology.....1

1.1.1 State-of-the-art Display Devices.....1

1.2 Introduction to QLED.....4

1.2.2 Charge Transport and Injection.....6

1.2.3 QLED Architecture and its Working Principle.....10

1.2.4 QLED architecture and its Evolution.....11

1.2.5 Materials in QLED.....13

1.3 QLED Performance Metrics.....17

1.4 Challenges.....19

1.5 Thesis Overview.....20

Chapter 2 Comprehensive Literature Review on the Stability Issues of QLEDs and the Proposed Solutions.....22

2.1 Photoluminescence Stability of QD Emission Layer.....22

2.1.1 Auger Recombination in QDs 23
2.1.2 Environmental Factors affecting PL stability of QDs 25
2.2 Charge Transport Materials 26
2.2.1 Charge Imbalance in the QD EML by Uneven Injection Rate of Electron and Hole 26
2.2.2 Degradation of Organic Materials 27
2.2.3 Accumulation of Charges at Heterointerfaces 28
2.3 Intrinsic Defects in ZnO Electron Transport Materials 29
2.3.1 Defect-mediated Charge Trapping and Exciton Quenching 30
2.3.2 Formation of Charged Species in ZnO 31
2.4 Proposed Solutions 33
2.4.1 Core-shell engineering 33
2.4.2 Ligands engineering for QDs 35
2.4.3 HTL engineering 37
2.4.4 ETL engineering 39
2.5 Summary 41
Chapter 3 Research Objectives and Methodology 43
3.1 Research Approaches and Aims 43
3.2 General Methodology in the Experiments 43
3.2.1 Device Architecture and its Fabrication Process 43
Chapter 4 Approaches to the ZnO Modification for QLED Stability Improvement 59
4.1 ZnO:PEI Nanocomposite Thin Films 59
4.1.1 Blending sol-gel ZnO and PEI for New Form of ETL 59
4.1.2 Results and Discussion 60

4.2 Halogen-incorporating into ZnO Nanoparticles 64

4.2.1 CF_4 Plasma Treatment on ZnO Nanoparticles 65

4.2.2 Introducing I_2 and $FeCl_3$ dopants into ZnO Nanoparticles 72

4.3 Chapter Summary 77

Chapter 5 The Influence of ZnO Modifications on Positive Charge Accumulation at the QD EML/HTL Interface 79

5.1 Changes in Charge Distribution across QLED by ZnO:PEI 80

5.1.1 Deeper Penetration of Electrons into HTL by ZnO:PEI 80

5.1.2 Electron-hole Recombination at the QD EML/HTL Interface 87

5.2 Changes in Electron Concentration within QD EML by FZnO 91

5.2.1 Reducing Trap Density in ZnO by F-incorporation and its Impact on Electron Concentration within QD EML 91

5.2.2 Probing Charge Accumulation and Annihilation within QLED during Device Operation 97

5.2.3 Electron-hole Recombination at the QD EML/HTL Interface 99

5.3 Chapter Summary 102

Chapter 6 Suppressing QLED Degradation via Reducing Positive Charges in the ZnO 103

6.1 The Role of Halides in Nanostructures 103

6.1.1 Investigating Charge Transfer at ZnO/QDs Interface 103

6.1.2 Changes in Electroluminescent Characteristics over QLED Aging 107

6.1.3 Reducing Formation of Positively Charged ZnO Species by Halides 109

6.2 Chapter Summary 121

Chapter 7 Investigating the Effect of Halide Treatment on ETL in Green- and Blue-QLED Performance 123

7.1 Doping ZnO by Halides for Inverted Green-QLED 123

7.2 The Halide Treatment on ETL for Upright Blue-QLED 125

7.2.1 Doping ZnO by Halides for Upright Blue-QLED 125

7.2.2 Doping ZnMgO by Halides for Upright Blue-QLED 127

7.3 Chapter Summary 130

Chapter 8 Summary and Suggestions for Future Work 132

8.1 Summary 132

8.2 Future Work 136

References 138

Appendix A Computation of Charge Trap Density 152

Appendix B Supplementary Information for Chapter 4 155

Appendix C Supplementary Information for Chapter 5 158

Appendix D Supplementary Information for Chapter 6 160

List of Figures

Figure 1.1 Evolution of display technology. 3

Figure 1.2 (a) Changes in density of states by reduction of material dimension. (b) Changes in energy band structure of QDs by reducing their size. 6

Figure 1.3 Electronic structure of solids (a) with small interatomic distance (< 3Å) enough to induce strong interatomic interactions and (b) with large intermolecular distances (> 10 Å). The structure shown in (b) is abbreviated as depicted in (c). The abbreviated structure is used to describe the energy levels of materials in QLEDs in this thesis...... 8

Figure 1.4 An example of energy level diagram of metal/semiconductor interface. The diagram includes work function, ionization potential, electron affinity, and band gap.. 9

Figure 1.5 Schematic diagrams describing the evolution of QLED architecture. 12

Figure 1.6 Schematic diagrams of (a) upright and (b) inverted QLED architecture. 13

Figure 1.7 Basic energy structure of (a) type-I, and (b) type-II core-shell QD structure. ... 15

Figure 1.8 Energy levels of materials examples used in QLEDs. The energy levels of the materials are discussed in the references.[28-31,38,39] 17

Figure 2.1 Energy level diagram showing some of the principal defect levels in ZnO. Reproduced with permission. Copyright 2012, Springer Nature[76]. 31

Figure 2.2 Schematic illustration of the core-shell QDs with ligands. The ligand structure is also represented. 36

Figure 3.1 (a) Layout of the device substrate used in this work. (b) A schematic image of the inverted QLED. 44

Figure 3.2 The current efficiency of QLED at 20 mA cm^{-2}. Each device is fabricated in different humidity conditions. 47

Figure 3.3 Current density and driving voltage dependence on post-annealing temperature of ZnO NP solution coating. 49

Figure 3.4 Pictures of (a) deposition chamber inside, (b) software screen that controls source/sample shutters. 51

Figure 3.5 (a) A picture of N_2-filled test box used in this work and (b) inside of the box where the device substrate is placed. 52

Figure 3.6 A picture of (a) Agilent 4155C semiconductor parameter analyzer and Agilent 15462A electrical channel and (b) silicon photodiodes connected to the electrical channel. 53

Figure 3.7 A picture of an experimental setup on optics table for EL/PL measurements. .. 54

Figure 3.8 A Picture of M6000PLUS OLED lifetime tester: (a) device lifetime test boxes, and (b) the test box inside. 55

Figure 3.9 A schematic image of delayed EL experimental setup. 57

Figure 4.1 (a) Schematic diagram showing the general structure of the QLEDs and the different ETLs investigated in this work. (b) J-V-L characteristics, (c) EQE *vs.* current density, and (d) EL spectra of the QLEDs. 62

Figure 4.2 (a) Relative luminance and (b) changes in driving voltage *vs.* time trends of the QLEDs with the different ETLs under 20 mA cm^{-2} constant current driving conditions. 64

Figure 4.3 (a) Schematic diagram of the plasma treatment setup. (b) XPS spectra of F 1s core level electrons in ZnO and FZnO films and (c) F^- and ZnO^+. All intensity values of TOF-SIMS are normalized by intensity of InO^- signal. O 1s core level electrons in (d) ZnO film and (e) FZnO film. (f) Steady-state PL spectra under 330 nm UV excitation collected from the ZnO and FZnO films. 67

Figure 4.4 (a) Schematic diagram depicting the QLED structure. (b) J-V-L characteristics, (c) EL spectra, and (d) EQE *vs.* current density of QLEDs with ZnO *vs.* FZnO ETLs. 70

Figure 4.5 (a) Luminance decay *vs.* time and (b) driving voltage *vs.* time of ZnO- and FZnO-QLEDs operated at a constant current density of 20 mA cm^{-2}. (c) Measured

LT50 values for different devices with operated at different L_0 values. The slopes correspond to the accelerator coefficients. 72

Figure 4.6 (a) Schematic diagram of the structure of the QLEDs used in this work. (b) J-V-L characteristics, (c) current efficiency *vs.* current density, and (d) EL spectra of QLEDs with ZnO, I_2:ZnO, and $FeCl_3$:ZnO ETLs. 74

Figure 4.7 (a) The initial current efficiency and LT50 at 20 mA cm^{-2} of all 14 QLEDs in each of the three groups. The round symbols and error bars give the average and standard deviation values of the same data for each group. (b) EL *vs.* time, (c) driving voltage *vs.* time, and (d) EL change rate *vs.* time of representative QLEDs from each group (i.e., with ZnO, I_2:ZnO, and $FeCl_3$:ZnO) under 20 mA cm^{-2} constant current driving. 76

Figure 4.8 The LT50s of QLEDs with various ETLs vs. charge balance factors extracted from EQEs of the QLEDs... 78

Figure 5.1 Schematic images of delayed EL measurement setup. Timings of shutter open/close, bias pulse, and EL are illustrated... 81

Figure 5.2 (a) Delayed EL of QLEDs with different ETLs. Reverse bias with 200 μs pulse on-time was applied at 0.2 ms. Delayed EL with increasing reverse bias of QLEDs with (b) ZnO, (c) ZnO/PEI, and (d) ZnO:$PEI_{0.3}$. 85

Figure 5.3 (a) Schematic diagram showing the general structure of the EODs. (b) J-V characteristics of EODs with the different ETLs.. 86

Figure 5.4 (a) Schematic diagram showing the general structure of the QLEDs with the CBP:FIrpic luminescent marking layer. (b) EL spectra from these with the various ETLs under 20 mA cm^{-2}. A spectrum from a ZnO ETL control device without the marking layer is also included for comparison. EL spectra from the QLEDs with the marking layer with (c) ZnO, (d) ZnO/PEI, (e) ZnO:$PEI_{0.1}$, and (f) ZnO:$PEI_{0.3}$ at various forward bias voltages... 91

Figure 5.5 (a) Schematic diagram of the EOD structure and the TRPL measurements scheme. The inset shows the energy levels of QDs/CBP/LiF/Al. (b) J-V characteristics

of EODs with ZnO and FZnO. (c) TRPL signal from the QD layer in the EODs with ZnO and FZnO without bias. (d) The τ_1 values extracted from the TRPL signal under the different bias levels. The error bars indicate the standard deviation in the data collected from 6 samples in each group. Schematic images of exciton dynamics in EODs with (e) ZnO and (f) FZnO. 97

Figure 5.6 (a) The equivalent circuit model used for the C-V analysis. (b) C-V-L characteristics of the QLEDs. 98

Figure 5.7 (a) Schematic diagram depicting the structure of the QLEDs with the FIrpic marking layer. (b) EL spectra from the same QLEDs under 20 mA cm^{-2}. A spectrum from a ZnO-QLED without the marking layer is also included for comparison. Schematic images of device operation in QLEDs with (c) ZnO and (d) FZnO. 101

Figure 6.1 (a) PL spectra of QDs deposited on ZnO, I_2:ZnO, and $FeCl_3$:ZnO. The PL peak heights are normalized to the height of the peak of the ZnO sample (b) A schematic diagram of the structure of the MIS-device and the polarities for forward and reverse bias. (c) QD PL intensity changes over time with ZnO, I_2:ZnO, and $FeCl_3$:ZnO without bias. QD PL intensity without bias and with FWD and REV bias with (d) ZnO, (e) I_2:ZnO, and (f) $FeCl_3$:ZnO. In each case, the QD PL intensities for FWD and REV bias are normalized to the PL intensity at no bias.. 106

Figure 6.2 J-V-L characteristics before (fresh), after electrical aging under 20 mA cm^{-2} constant current driving for 20 hours, and after reaching LT50s of the QLEDs with (a) ZnO, (b) I_2:ZnO, and (c) $FeCl_3$:ZnO. (d-f) The same J-V-L characteristics presented on log-log scales. 109

Figure 6.3 J-V-L characteristics measured under two sweep directions (i.e., 0 V to 10 V and 10 V to 0 V) of QLEDs with (a) ZnO, (b) I_2:ZnO, and (c) $FeCl_3$:ZnO, with the second sweep starting immediately following the first sweep. 110

Figure 6.4 (a) Simulation result showing charge distribution and radiative recombination rate in QLEDs with different dopant concentrations. (b) The hole concentration in ETL with different dopant concentrations. 112

Figure 6.5 Normalized peak intensity of (a) Zn $2p_{3/2}$ and (b) Cd $3d_{5/2}$ XPS spectra for calibration curves. (c) XPS spectra of In 3d core level electrons from 0 s to 500 s sputtering time. XPS spectra of C 1s core level electrons in fresh- and electrically aged-QLEDs measured after 100 s and 300 s sputtering time with (d and g) ZnO, (e and h) I_2:ZnO, and (f and i) $FeCl_3$:ZnO. 114

Figure 6.6 (a) Schematic diagram of the QLED sample used for the XPS measurements showing the removal of the Al electrode by scotch tape after device aging has been completed in order to allow testing the underlying layers by XPS. XPS spectra of Cd $3d_{5/2}$ core level electrons in fresh QLEDs with (b) ZnO, (c) I_2:ZnO, and (d) $FeCl_3$:ZnO and in electrically aged QLEDs with (e) ZnO, (f) I_2:ZnO, and (g) $FeCl_3$:ZnO. 115

Figure 6.7 XPS spectra of Zn $2p_{3/2}$ core level electrons in fresh QLEDs with (a) ZnO, (b) I_2:ZnO, and (c) $FeCl_3$:ZnO and in electrically aged QLEDs with (d) ZnO, (e) I_2:ZnO, and (f) $FeCl_3$:ZnO. XPS spectra of (g) I 3d collected from I_2:ZnO-QLEDs, and (h) Cl 2p in QLEDs with $FeCl_3$:ZnO. The signals collected from ZnO-QLEDs are displayed for comparisons. All the XPS spectra are measured after 300 s sputtering time. (i) Areal ratio changes of higher oxidation state bands in XPS Zn $2p_{3/2}$ spectra between fresh- and electrically aged-QLEDs with the EL decrease rate within 20 hours of the QLEDs. The rate of EL loss in the first 20 hours of each QLED is also presented. .. 118

Figure 6.8 (a) XPS spectra of O 1s core level electrons from the QLEDs with different ETLs. XPS spectra comparison of fresh- and electrically aged-QLEDs with (b) ZnO, (c) I_2:ZnO, and (d) $FeCl_3$:ZnO. (e) Schematic illustration of the effect of halides on the accumulation of holes in the ETL during device operation. 121

Figure 7.1 (a) Schematic diagram of the structure of the green inverted QLEDs. (b) J-V-L characteristics, (c) EL spectra, (d) current efficiency *vs.* current density, and (e) EL *vs.* time under 20 mA cm^{-2} constant current driving of the QLEDs. 125

Figure 7.2 (a) Schematic diagram of the structure of the blue upright QLEDs with ZnO, I_2:ZnO, and $FeCl_3$:ZnO. (b) J-V-L characteristics, (c) EL spectra, (d) current efficiency

vs. current density, and (e) EL *vs.* time under 20 mA cm^{-2} constant current driving of the QLEDs. 127

Figure 7.3 (a) Schematic diagram of the structure of the blue upright QLEDs with ZnMgO, and I_2:ZnMgO. (b) J-V-L characteristics, (c) EL spectra, (d) current efficiency *vs.* current density, and (e) EL *vs.* time under 20 mA cm^{-2} constant current driving of the QLEDs. 129

Figure 7.4 XPS spectra of O 1s core level electrons from (a) ZnO, and (b) ZnMgO. 130

Figure S1.1 (a) Energy level diagram of the MIS-device used for the capacitance-voltage measurement in this experiment. (b) Calculated carrier concentration *vs.* depth of ZnO. 153

Figure S1.2 (a) Calculated trap density *vs.* current density of QLEDs with ZnO and FZnO. 154

Figure S4.1 (a) Current efficiency and (b) LT50 at 20 mA cm^{-2} with various dopant concentrations, and (c) LT50 *vs.* current efficiency for each of 14 individual QLED in each group. 155

Figure S5.1 EL spectra from devices containing the CBP:FIrpic marking layer with (a) ZnO:$PEI_{0.1}$ ETL, and (b) ZnO:$PEI_{0.3}$ ETL, at higher forward bias voltages than in Figure 5.4 (e and f) 158

Figure S5.2 TRPL results of EODs with (a) ZnO and (b) FZnO with reverse bias 158

Figure S6.1 (a) UV-vis absorption spectra of ZnO, I_2:ZnO, and $FeCl_3$:ZnO films. Tauc plots of (b) ZnO, (c) I_2:ZnO, and (d) $FeCl_3$:ZnO films. The $E_{g,optical}$ is estimated from the extrapolated tangent lines of the linear parts on the Tauc plots. 160

List of Tables

Table S4.1 LT50 and EQE of QLEDs with different ETLs. LT50 projection for L_0=100 cd m^{-2} is calculated by lifetime relation equation (1.20). Acceleration factor *n* of 1.8 is used and LT50 is based on a measured value under 20 mA cm^{-2} of constant current.155

Table S4.2 Comparison of the stability performance of the QLEDs reported here with other highly stable devices with CdSe QDs via ETL modifications. LT50s not reported in the original work are estimated using equation (1.20) and an acceleration factor 1.8. 156

Table S5.1 τ and A components extracted from the tri-exponential decay curves. The first two rows correspond to the measurement under reverse bias. 159

Table S6.1 The values of the various parameters used in the SCAPS simulation for (a) ZnO ETL, QD EML, and CBP HTL, and (b) the dopants. 161

List of Abbreviations

AFM: Atomic force microscopy

BCBP: 2,2'-bis(4-(carbazol-9-yl)phenyl)-biphenyl

BLU: Back light unit

CBM: Conduction band minimum

CBP: 4,4′-Bis(N-carbazolyl)-1,1′-biphenyl

CE: Current efficiency

CRT: Cathode ray tube

CTL: Charge transport layer

DDT: 1-dodecanethiol

DoS: Density of states

EA: Electroabsorption

EL: Electroluminescence

EML: Emission layer

EOD: Electron-only device

EQE: External quantum efficiency

ETL: Electron transport layer

F4TCNQ: 2, 3,5, 6-tetrafluoro-7,7,7,7,-tetracyanoquinodimethan

FIrpic: Bis(2-(4,6-difluorophenyl)pyridinato-C2,N) (picolinato) iridium (III)

FWHM: Full width half maximum

HIL: Hole injection layer

HOMO: Highest occupied molecular orbital

HTL: Hole transport layer

IQE: Internal quantum efficiency

ITO: Indium tin oxide

LT50: The lifetime projection of 50 %, measuring the time it takes for the relative luminance to become half of the initial luminance

LUMO: Lowest unoccupied molecular orbital

NP: Nanoparticles

OLED: Organic light emitting device

PE: Power efficiency

PEDOT:PSS: Poly(ethylenedioxythiophene):polystyrene sulfonate

PEI: Polyethylenimine

PF8Cz: Poly((9,9-dioctylfluorenyl-2,7-diyl)-alt-(9-(2-ethylhexyl)-carbazole-3,6-diyl))

PL: Photoluminescence

PLQY: Photoluminescence quantum yield

PMMA: Poly(methyl methacrylate)

PPV: Poly(p-phenylenevinylene)

PVK: Poly(vinylcarbazole)

QD: Quantum-dot

QLED: Quantum-dot light emitting device

RMS: Root mean square

SRH recombination: Shockley-Read-Hall recombination

TCTA: 4,4′,4″-tris- (carbazol-9-yl)triphenylamine

TFB: Poly(9,9-dioctylfluorene-co-N-(4-(3-methylpropyl))diphenylamine

T_g: Glass transition temperature

TOF-SIMS: Time-of-flight secondary ion mass spectroscopy

TRPL: Time resolved photoluminescence

TTA: Triplet-triplet annihilation

VB-FNPD: 9,9-Bis(4-((4-ethenylphenyl)methoxy]phenyl]-N2,N7-di-1-naphthalenyl-N2,N7-diphenyl-9H-Fluorene-2,7-diamine

VBM: Valence band maximum

WF: Work function

XPS: X-ray photoemission spectroscopy

Chapter 1 Introduction

1.1 Introduction to Display Technology

1.1.1 State-of-the-art Display Devices

The display market has witnessed remarkable success with liquid crystal displays (LCD) and organic light emitting diode (OLED) displays, outperforming various other display devices.[1] LCDs gained significant traction in the early 2000s, successfully overcoming the technological limitations of cathode ray tube (CRT) displays. LCDs showcased distinct advantages, including high luminance, relatively low operating voltage, and affordability compared to their predecessor displays. LCDs operate by polarizing light through the arrangement of liquid crystals via bias application. This requires a backlight unit (BLU), through which light passes, interacting with the specific liquid crystal orientation and additional color conversion layers that achieve the desired colors. However, LCDs face certain operational drawbacks, including slow response times due to molecular motion limitations, compromised color purity and contrast due to challenges in achieving a complete 'dark' state, inefficiencies due to light waste at the color conversion layer, and the necessity of a BLU that hinders the manufacturing of thin display products. On the other hand, OLED displays entered the market with notable advantages that address several of the LCD's drawbacks. OLEDs incorporate a self-emissive layer, offering significant benefits in terms of color quality and streamlined processing for creating thin and large display products, eliminating the need for a BLU. OLEDs have found applications across a wide spectrum of display use cases. Currently, these two display types command the largest market share in various domains of display products, spanning television, computer screens, and smartphone screens.

Technological convergence leads to the transformation of traditional linear media into highly interactive formats, causing visual content to become pervasive in society as an everyday element.[2] In the context of this widespread visual display environment, the imperative to establish connections between humans and machines through visual information

has elevated the significance of high-performance luminescent devices. These devices play a central role in realizing present and future display technologies, including innovations like VR/AR devices, window and outdoor screen displays, wearable display units, and holography displays. These technologies essentially create *ubiquitous scenarios for visual information*. Among these pioneering display devices, the reliance on OLEDs and LCDs is pronounced today. As the bedrock of electronic visual displays, the growth of these advanced display technologies hinges on attributes such as high resolution, efficiency, stability, and a wide color gamut in light emitting devices. To achieve a vibrant visual environment, substantial improvement in color purity is essential, surpassing the capabilities of current state-of-the-art display devices. While contemporary OLEDs can provide respectable color purity (with a full width at half maximum of EL wavelength spectra < 50 nm), there is still room for enhancement.[3] Furthermore, device stability during operation poses another formidable challenge. Given the increasing duration of display device usage, attaining exceptionally high device stability is of paramount importance. OLEDs have encountered stability concerns, exemplified by issues like burn-in, attributed to the inherent limitations of organic materials.

To overcome these challenges, inorganic quantum dots (QDs) have been actively researched as a prominent material for display devices. Capitalizing on their distinct luminescence properties, which encompass nearly 100% photoluminescence quantum yield (PLQY), narrow emission spectra, and the flexibility to adjust their emission wavelength, QDs have captured considerable attention within the scientific community. In comparison to state-of-the-art OLEDs that employ organic emitting materials, QDs present a remarkable potential for significantly enhanced color purity and a substantial expansion in color gamut and saturation. As a result, endeavors have been made to integrate QDs into display technologies, commencing with traditional LCDs and OLED displays. *Samsung*, for instance, has brought to market displays that leverage QDs in color conversion layers for both LCDs and OLEDs, enhancing color saturation due to the precisely tuned emission spectra of QDs.[4] However, these devices have yet to fully exploit the comprehensive advantages offered by QDs. Consequently,

ongoing research is concentrated on leveraging QDs within the emission layer of self-emissive devices, utilizing their electroluminescence (EL) characteristics, rather than confining their role to color conversion layers alone. Unlike LCDs and OLEDs, where a substantial portion of light output is absorbed by the color conversion layer, QDs within an LED emission layer (QLED) can deliver heightened luminance and color purity, accompanied by a broader color gamut. This is achieved through their sharper emission spectra, all without necessitating supplementary conversion layers.

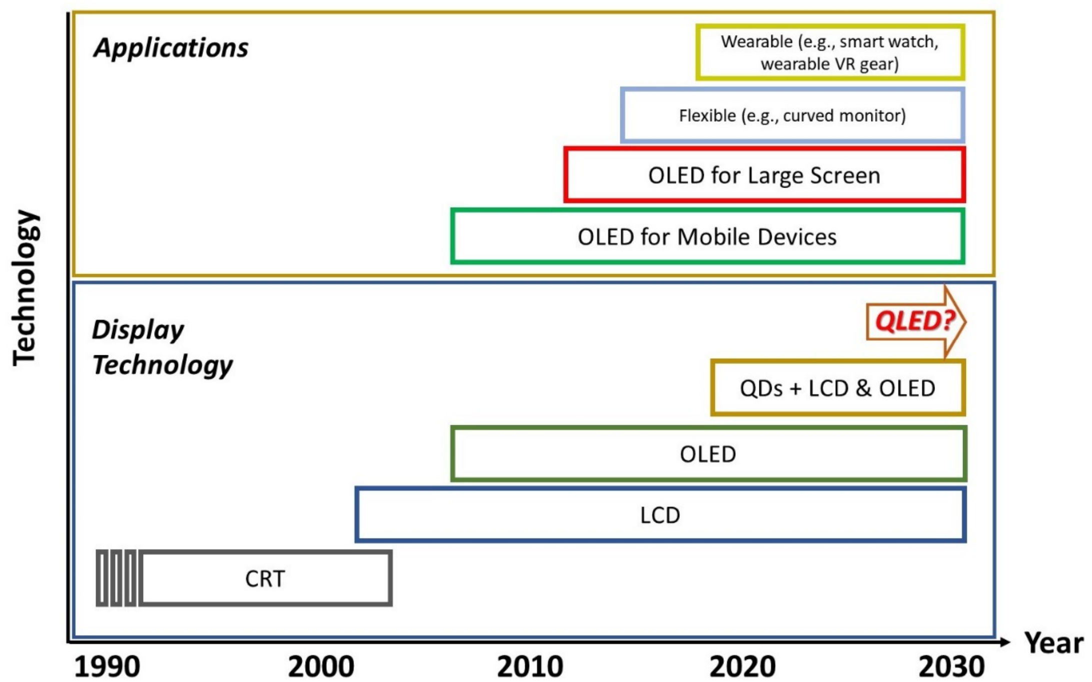

Figure 1.1 Evolution of display technology.

1.2 Introduction to QLED

1.2.1 Characteristics of QDs

The luminescence mechanism of QDs is governed by the excitation and subsequent relaxation of carriers within the QDs through external energy input. The creation of excitons within the QDs dictates the radiative recombination process. The prevailing explanation for excitons in inorganic QD materials is the Wannier-Mott exciton model,[5-7] which conceptualizes an exciton as an electron-hole pair held together by Coulombic attraction. Complementary insights into the exciton system are provided by the Bohr model. The exciton radius, signifying the distance between the electron and hole within the exciton, can be understood in a manner analogous to the Bohr radius within the hydrogen atom model. The exciton Bohr radius r_B is described by[5-7]

$$r_B = \frac{4 \cdot \pi \cdot \varepsilon \cdot \hbar^2}{q^2} \cdot \left(\frac{1}{m_e} + \frac{1}{m_h}\right) \tag{1.1}$$

where q is an elementary charge, ε is a dielectric constant of the material, $\hbar$ is a reduced Planck constant. m_e and m_h are an effective mass (m_{eff}) of electron and hole, respectively. The most fascinating property of the QDs stems from the quantum confinement effect resulting from their dimension reduction. As the crystal size (often consider the radius, r) diminishes and approaches the r_B, the material's energy state becomes quantized. This quantization of energy state is governed by the Schrödinger equation within a spherical, three-dimensional infinite potential well system. Further elaboration on the detailed solution can be found in the referenced source[5]. The confinement energy state for the ground state ($n = 1$) is then described by[5-7]

$$E_{n=1} = E_g - \frac{q^2}{2\varepsilon \cdot r_B} + \frac{\pi^2 \cdot \hbar^2}{2m_{eff} \cdot r^2} \tag{1.2}$$

where E_g is energy band gap. This equation delineates the alterations in the energy states as the material's radius undergoes change. The quantum confinement effect (i.e., $r_B > r$) governs

the density of states (DoS) within the material, leading to quantization of electronic states. As depicted in Figure 1.2 (a), the relationship between DoS *vs.* energy takes on a delta-function-like form as dimensions reduce. Consequently, each energy state is accompanied by a wave function bearing resemblance to atomic behavior. Consequently, QDs possess quantized energy states at their band edges, thus manifesting atomic-like traits. This characteristic facilitates the adjustment of emission wavelengths through size variations, as illustrated in Figure 1.2 (b). Additionally, the atomic-like structure relaxes the momentum conservation rule within QDs due to the broken translational symmetry, alongside intensified Coulombic interaction between charge carriers. This heightened interaction enhances the probability of energy relaxation via Auger recombination. Auger recombination is delved into further in Chapter 2, given its involvement in various phenomena within QDs.

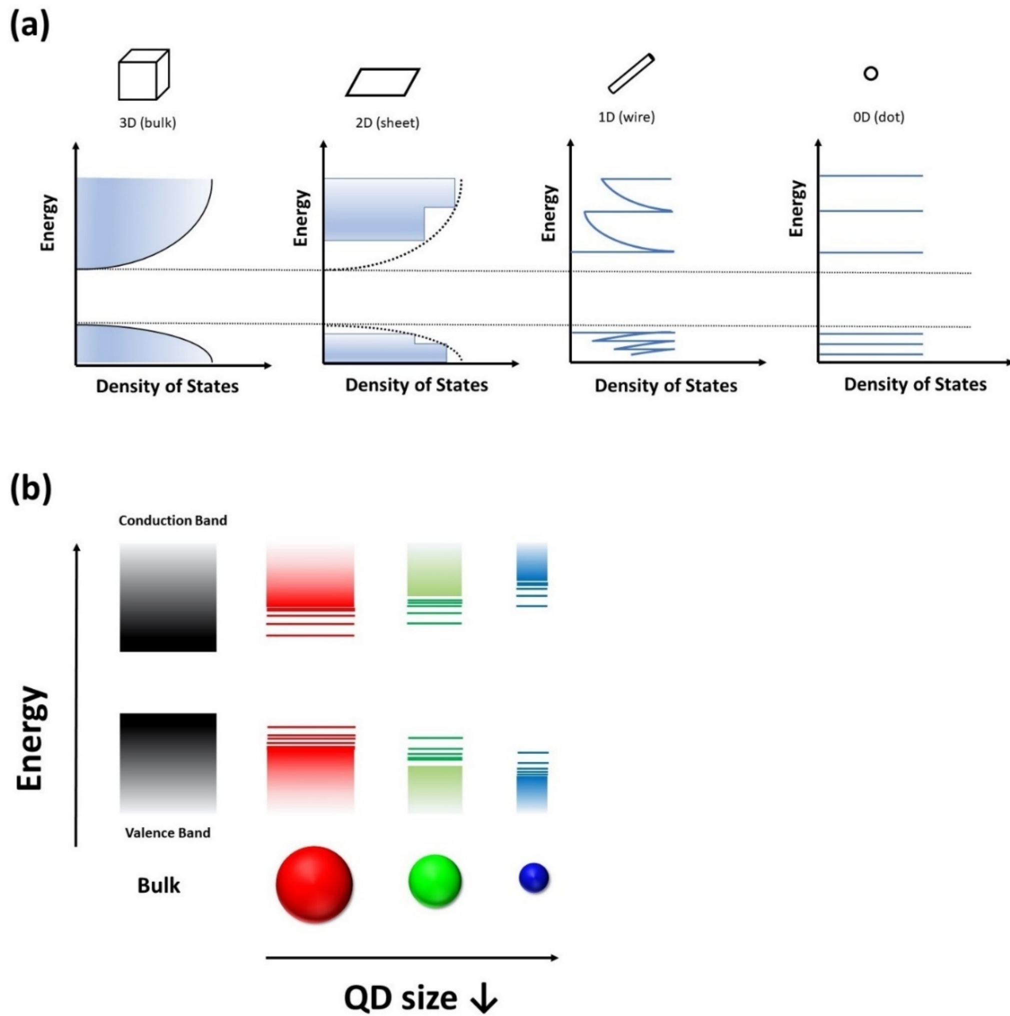

Figure 1.2 (a) Changes in density of states by reduction of material dimension. (b) Changes in energy band structure of QDs by reducing their size.

1.2.2 Charge Transport and Injection

The accurate transport and injection model must be taken into consideration to estimate and analyze carrier transport and injection during QLED operation[8-10]. The electrical conduction of the material is elucidated by the Drude model, which delineates the connection between current density (J) and electric field (E)[8]

$$J = (\frac{n \cdot q^2 \cdot \tau}{m}) \cdot E \quad (1.3)$$

where n is a charge concentration, q is an elementary charge, τ is a mean free time between collisions during charge transport, and m is a mass of electron. The conductivity σ is then[8]

$$\sigma = q \cdot n \cdot \mu \quad (1.4)$$

where μ is a carrier mobility. Utilizing equation (1.4) as a basis, the conductivity is dictated by the concentration of charge carriers and their mobility. In the context of typical QLED materials like organic semiconductors, nanoparticles (NPs), and QDs, intrinsic charge concentrations are usually negligible. Instead, the injection of charges from electrodes plays a predominant role in determining the charge concentration. Consequently, both the carrier mobility of the materials and the charge injection from electrodes become pivotal elements in characterizing charge carrier conduction during QLED operation. The charge carrier mobility of these materials is notably influenced by interatomic and intermolecular interactions. When atoms approach one another, their orbital wave functions begin to interact, culminating in the formation of molecular orbitals. A multitude of atomic or molecular orbital interactions, giving rise to a significant number of orbital splittings, results in the emergence of energy levels. In the case of inorganic semiconductors (e.g., Si and Ge), atomic distances are sufficiently small (< 3Å) to evoke potent interatomic interactions. This leads to the splitting of energy levels and the formation of conduction and valence bands where electrons and holes can move freely, as depicted in Figure 1.3 (a). Similarly, in organic materials characterized by extensive π-conjugation and close intermolecular distances, robust molecular interactions lead to the creation of a continuous energy band, akin to the situation in inorganic semiconductors. On the contrary, polycrystalline and amorphous materials with larger intermolecular distances (> 10 Å) exhibit discontinuous molecular energy levels due to weak intermolecular interaction, illustrated in Figure 1.3 (b). These non-continuous energy states function as trap sites for charge carriers, where carriers can reside for a relatively extended duration. Consequently, the mechanism governing carrier transport shifts to the hopping mechanism, as elucidated by the

Poole-Frenkel model.[9,10] This model involves carriers literally hopping and transitioning between discrete energy states amidst molecules. This process necessitates surmounting an energy barrier (ΔE) through a thermally activated trapping and de-trapping process. Compared to band transport mechanisms, the hopping transport exhibits relatively low carrier mobility (< 10^{-3} cm^2 V^{-1} s^{-1}). For materials with disorder, such as those incorporated into the QLED structure (e.g., organic semiconductors, QDs, and NPs), the transport mechanism is likely to align with the hopping mechanism.

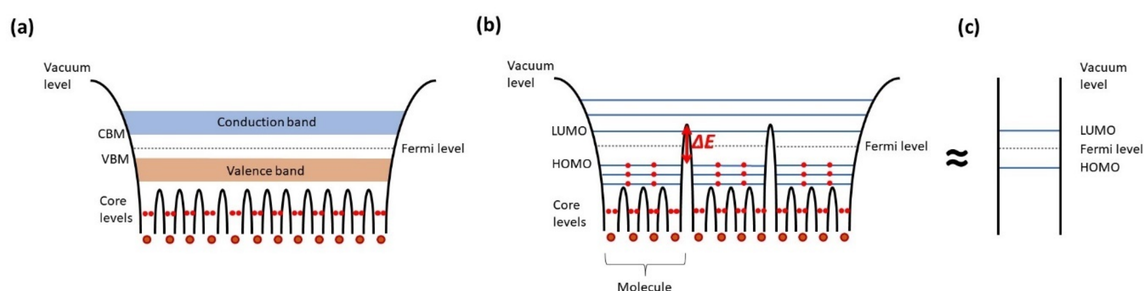

Figure 1.3 Electronic structure of solids (a) with small interatomic distance (< 3Å) enough to induce strong interatomic interactions and (b) with large intermolecular distances (> 10 Å). The structure shown in (b) is abbreviated as depicted in (c). The abbreviated structure is used to describe the energy levels of materials in QLEDs in this thesis.

The charge injection mechanism constitutes another important factor for assessing the QLED operation, as the concentration of charges within the QLED is dictated by the charges introduced from electrodes.[11] The Schottky-Mott rule governing the metal/semiconductor interface serves as the foundation for understanding the injection characteristics at the electrode/charge transport layer (CTL) interface.[11] Therefore, the interfacial barrier height for electron injection, Φ_e (and Φ_h for hole injection), hinges on the energy level disparity between the electron affinity A_e (or ionization potential, I_p, in the case of hole injection barriers) of the CTL and work function of the metal (WF), illustrated in Figure 1.4.[8]

$$\Phi_e = W\ F - A_e \tag{1.5}$$

and for the hole injection barrier[8]

$$\Phi_h = I_p - W\ F \tag{1.6}$$

Charge carriers are introduced through various mechanisms, encompassing field-assisted thermionic injection, Fowler-Nordheim tunneling, and thermoactivated hopping injection.

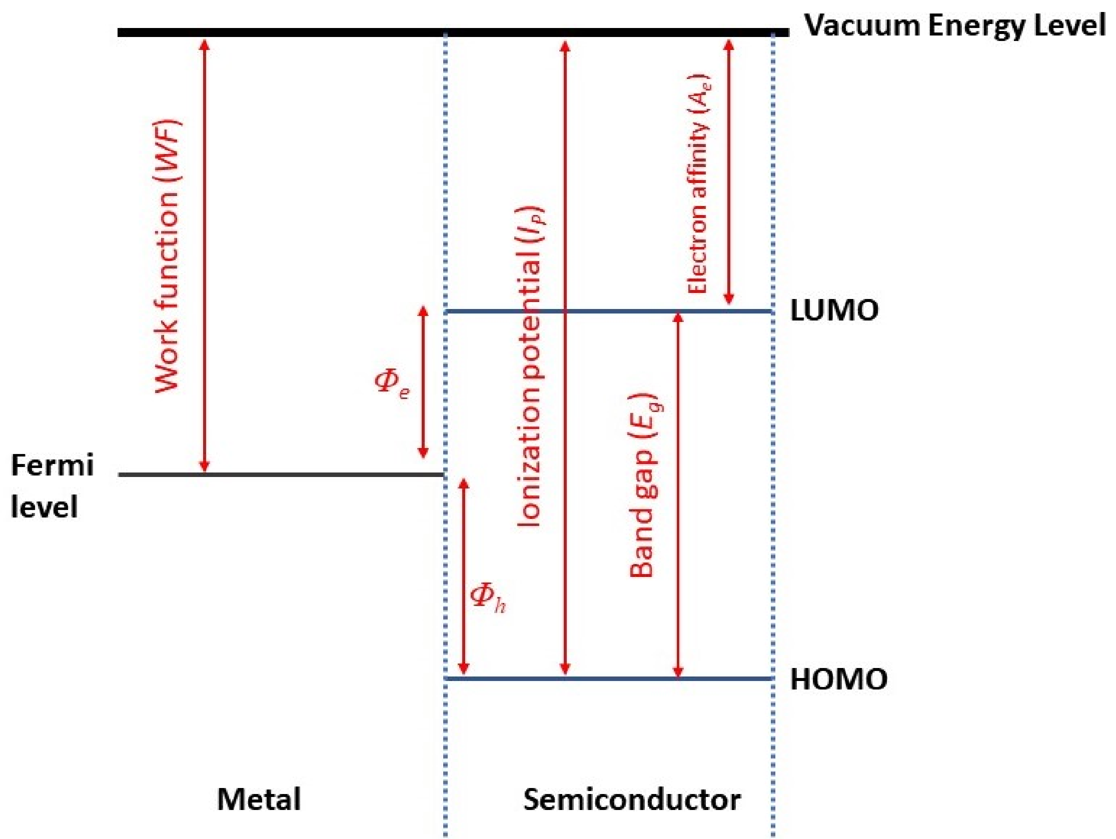

Figure 1.4 An example of energy level diagram of metal/semiconductor interface. The diagram includes work function, ionization potential, electron affinity, and band gap.

1.2.3 QLED Architecture and its Working Principle

The operational mechanism of QLEDs primarily follows these steps:

1. Electrons and holes are introduced from the cathode and anode, respectively, into the ETL and the HTL.
2. Electrons and holes then traverse through the ETL and HTL to reach the QD emission layer (EML).
3. Within the QD EML, Coulombic interaction between electrons and holes leads to the formation of excitons.
4. Subsequently, excitons undergo radiative recombination, emitting photons.

The architecture of a QLED is composed of material stacks with distinct functionalities: Anode/HTL/QD EML/ETL/cathode. The mode of charge carrier transport is contingent on the characteristics of both HTL and ETL. Fundamentally, the operational principle shares similarities with OLEDs. The majority of distinguishing traits of QLEDs originate from the unique characteristics of the QD EML, as the electroluminescent behavior is substantially shaped by the luminescence properties of the QDs. Furthermore, QLEDs benefit from a broader selection of charge transport materials compared to OLEDs. Unlike bulk semiconductors where electrons and holes behave as statistically independent entities, diffusing and injecting into the EML to form excitons, the process of exciton formation in QDs can be influenced by intermediate states of the QDs (either negatively or positively charged QDs). These states promote the injection of opposite carriers through their electrostatic forces.[12-15] Consequently, QLEDs exhibit a higher tolerance for charge imbalances within the EML. This attribute offers a diverse array of options for charge transport materials, such as combinations of organic and inorganic semiconductors for CTLs.

1.2.4 QLED architecture and its Evolution

Device structure evolution with respect to charge transport materials

The device structure has evolved and undergone modifications based on the selection of ETL and HTL material types for high-performance QLEDs, as illustrated schematically in Figure 1.5. The first QLED was demonstrated in 1994, comprising a polymer HTL (PPV, poly(p-phenylene vinylene)) and a QD EML flanked by two electrodes.[16] Although this simple device structure exhibited low device efficiency, it marked a significant milestone as the first EL device incorporating a QD EML, heralding the advent of QLEDs. The primary drawback of the initial generation device structure was limited electron injection due to the absence of ETLs. To address this, organic ETLs were introduced on the opposite side of QD EMLs, leading to the emergence of the HTL/QD EML/ETL structure, commonly known as 2nd-generation QLEDs.[17] While this enhanced the device performance to some degree compared to the 1st generation structure, the efficiency of organic CTLs still fell short, remaining under 1% in external quantum efficiency (EQE) and significantly below their theoretical limit. This low EQE was ascribed to inadequate injection at the heterojunction between organic materials and the QDs. While the introduction of organic ETLs addressed the electron injection issue, the charge imbalance problem within the QD EML persisted, resulting in substantial efficiency reduction. Subsequently, attempts were made to employ inorganic materials for both ETL and HTL, aiming to circumvent the challenges posed by organic CTLs.[18] However, the use of inorganic CTLs did not yield a sufficiently notable improvement in device efficiency. This was attributed to the high intrinsic carrier concentration of inorganic semiconductors, which triggered exciton quenching in the QD EML through inter-/intra-energy transfer, particularly at the QD EML/CTL interface. This interaction among a large number of carriers in inorganic semiconductors led to the loss of radiative recombination energy. Additionally, the limited selection of inorganic hole transport materials posed an additional challenge. The merits and limitations of both organic and inorganic transport materials culminated in the development of the current predominant QLED architecture, termed a hybrid QLED structure.[19] This 3rd

generation device architecture integrates an inorganic ETL and an organic HTL with a QD EML. Inorganic ETLs exhibit superior electron transport/injection properties along with chemical stability. On the other hand, organic HTLs demonstrate favorable hole transport capabilities and can be reliably deposited using state-of-the-art OLED technology. The combination of these advantages from both CTLs yields highly efficient QLEDs, achieving optimal EQE levels exceeding 20 % for red-,[20,21] green-,[22,23] and blue-QLEDs.[23-25]

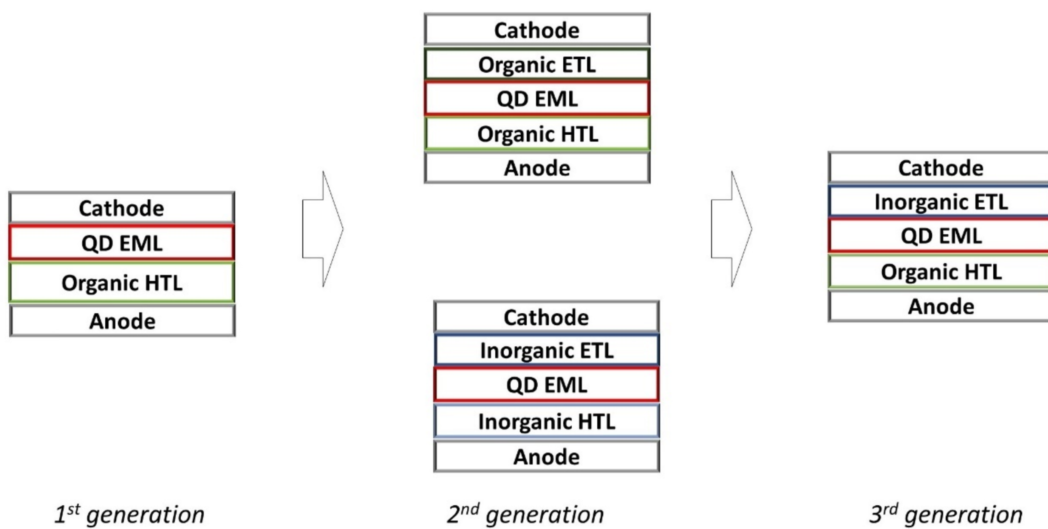

Figure 1.5 Schematic diagrams describing the evolution of QLED architecture.

Upright *vs.* Inverted device architecture

The deposition order also serves as a key criterion in determining the device architecture. Given that QLEDs are thin-film devices fabricated on supportive substrates, layer arrangement and deposition commence from the substrate side. Typically, indium tin oxide (ITO) is the initial coated layer, acting as an electrode. The standard LED structure follows the order: ITO/CTL_1/EML/CTL_2/Al (or Ag). CTL_1 represents the first-deposited carrier transport

layer (either HTL or ETL) directly placed on the ITO, while CTL_2 denotes the second carrier transport layer deposited on the EML, functioning as the counterpart to CTL_1 (either ETL or HTL). The conventional configuration, known as the upright architecture, entails an HTL deposited on ITO (i.e., CTL_1 is an HTL), as depicted schematically in Figure 1.6 (a). Conversely, the inverted architecture involves an ETL deposited on ITO (i.e., CTL_1 is an ETL), as illustrated in Figure 1.6 (b). The inverted architecture offers the benefit of ETLs connecting to n-type thin film transistors within the circuit, streamlining the fabrication sequence for active-matrix LED circuits.[26] Moreover, the inverted architecture affords flexibility in engineering ETLs while preventing any potential damage to the QD EML and HTL.

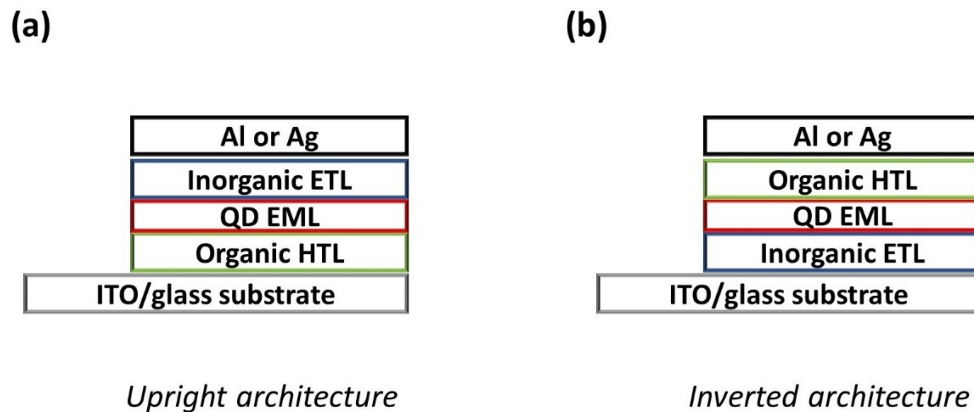

Figure 1.6 Schematic diagrams of (a) upright and (b) inverted QLED architecture.

1.2.5 Materials in QLED

Since the operation of LEDs hinges on the conversion of electrical energy into light, the meticulous choice of materials for QD EMLs and CTLs becomes paramount. The advancement of materials for QDs and charge transport/injection elements has yielded

significant strides in enhancing QLED performance, hand in hand with the evolution of QLED architecture. This section outlines the materials employed in the hybrid QLED architecture.

Core-shell QD materials

In addition to the limitations of the discussed device architecture above, the core-only QD structure is prone to losing carrier confinement, resulting in a significant reduction of device efficiency. In 1997, Schlamp et al. published their findings showcasing the use of CdSe/CdS core/shell QDs as an EML in the 1st generation device structure, effectively enhancing device efficiency compared to core-only QDs.[27] Core/shell structures can generally be categorized into two primary types based on the energy level offset between the core and shell materials, which dictates the nature of their heterojunction. The type-I structure features a straddling gap at the core-shell heterojunction, as illustrated in Figure 1.7 (a). Conversely, when the core and shell materials create a staggered gap at their heterojunction, the structure is classified as type-II, as shown in Figure 1.7 (b). Consequently, the type-I QD structure is more efficient in confining electrons and holes compared to type-II. For instance, CdSe/ZnS QDs possess a type-I structure and are primarily explored for LEDs that necessitate exciton formation. Conversely, the type-II structure might find more utility in other device applications such as solar cells and photodetectors, which require efficient exciton dissociation. Recognizing the significance of shell materials, the development of core-shell QD structures emerged. Among these, II-VI material-based QDs have garnered widespread adoption for EMLs, attributed to their high photoluminescence quantum yield (PLQY) and extensive developmental history. CdSe core paired with ZnS and CdS shell materials has been extensively investigated for EMLs in QLEDs.

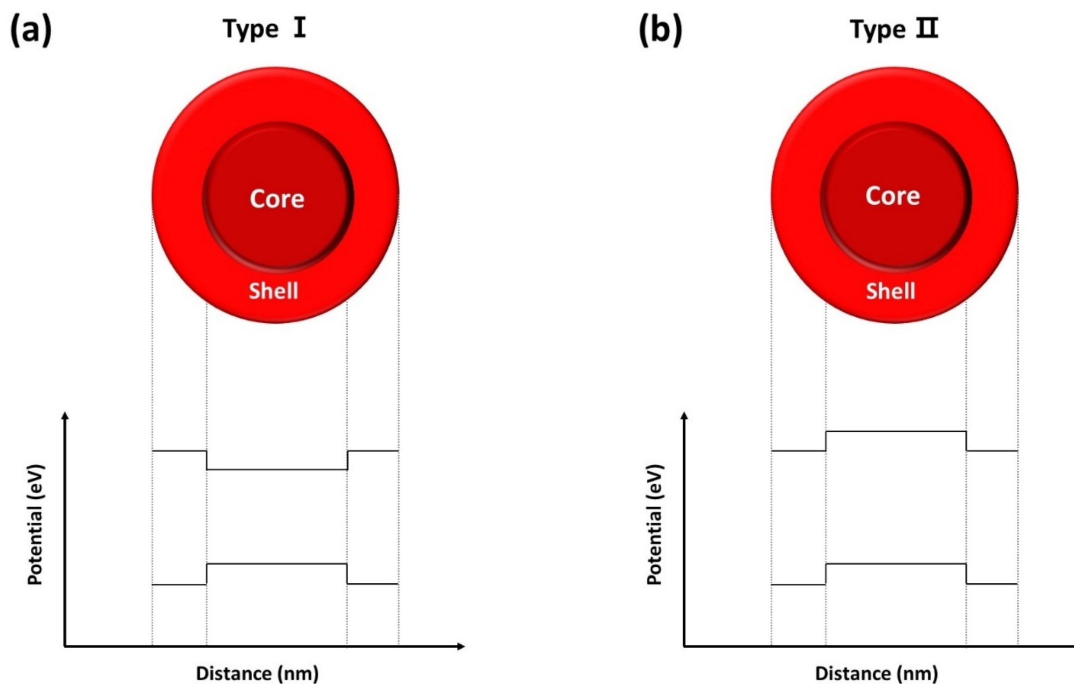

Figure 1.7 Basic energy structure of (a) type-I, and (b) type-II core-shell QD structure.

Organic hole transport materials

The selection of appropriate hole transport materials is a pivotal aspect of device design to ensure efficient hole transport and injection during QLED operation. In the realm of organic HTLs, materials such as 4,4′-Bis(N-carbazolyl)-1,1′-biphenyl (CBP)[28] and tris(4-carbazoyl-9-ylphenyl)amine (TCTA)[29] for small molecules, and poly(9,9-dioctylfluorene-alt-N-(4-sec-butylphenyl)-diphenylamine) (TFB)[30] and polyvinylcarbazole (PVK)[31] for polymers have found extensive application in QLEDs. The mobility of holes within these materials plays a pivotal role in achieving effective hole transport through the HTL. The highest occupied molecular orbital (HOMO) level is another critical consideration, ensuring efficient hole

injection at both the HTL/anode interface and the QD EML/HTL interface. Meanwhile, a shallow lowest unoccupied molecular orbital (LUMO) level can prove advantageous by increasing the energy barrier for electrons at the QD EML/HTL junction. Hence, an ideal hole transport material should exhibit high hole mobility in conjunction with deep HOMO and shallow LUMO levels.

ZnO electron transport materials

Ever since its advantageous impact on QLED efficiency was demonstrated,[32] ZnO and its derivatives have garnered almost universal preference as the material of choice. ZnO, a semiconductor material with a wide band gap (E_g) of 3.37 eV,[33-35] inherently exhibits n-type properties,[34,36,37] the precise origin of which is still a subject of debate. ZnO materials offer compelling advantages, encompassing their adaptability to solution-based processing and commendable electron transport characteristics. Furthermore, ZnO's wide E_g ensures minimal absorption of visible light, rendering it suitable for application in LEDs. The utilization of ZnO ETL in QLEDs has consistently yielded superior performance compared to other electron transport materials. This can be attributed to the well-aligned conduction band minima (CBM) between ZnO and CdSe, which facilitates efficient electron injection into the QD EML. ZnO's exceptional electron transport properties, compatibility with the QD EML, and transparency collectively establish it as an optimal choice for ETL in QLEDs.

Figure 1.8 illustrates the energy levels of selected materials that have found widespread usage in QLEDs.

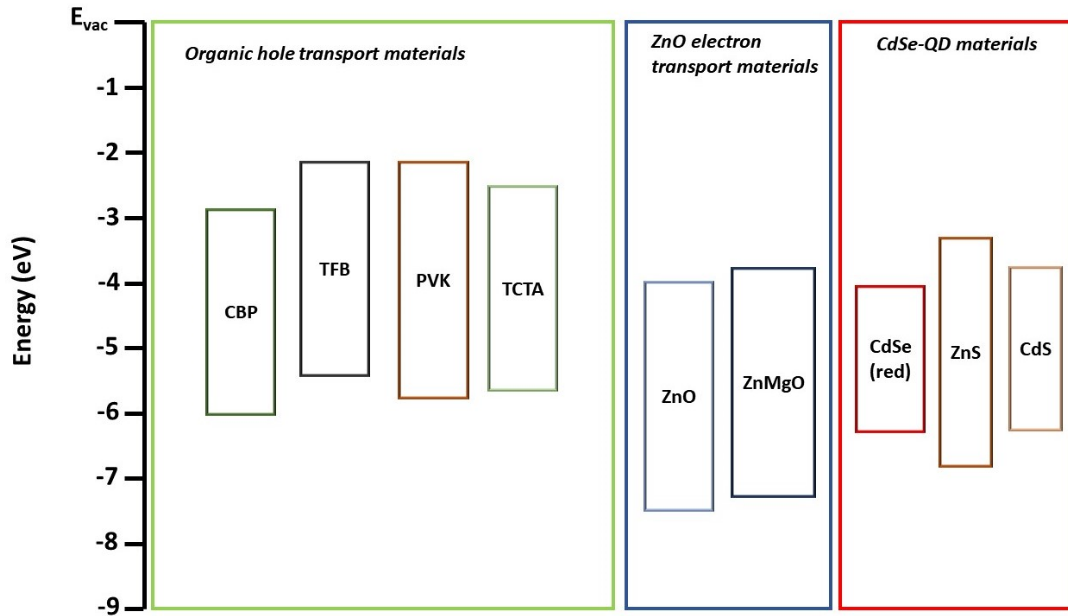

Figure 1.8 Energy levels of materials examples used in QLEDs. The energy levels of the materials are discussed in the references.[28-31,38,39]

1.3 QLED Performance Metrics

To gauge the EL performance of QLEDs, several metrics come into play. These encompass gauging the efficiency of exciton formation and radiative recombination that lead to photon emission outside the QLED, alongside evaluating the endurance and consistency of the photon emission process during device operation. In this context, two primary performance metrics take the spotlight for evaluating QLED performance: (1) EL efficiency and (2) EL stability. This section provides an overview of the performance assessment related to luminance, EL efficiency, and stability.

Luminance

Luminance pertains to the luminous intensity radiated by a light source within a specific direction, per unit area, and within a unit solid angle. This fundamental metric gauges the perceived brightness of a light source to human eyes, taking into account the eye's sensitivity to varying wavelengths of light. Luminance serves as a means to approximate the intensity of both EL and PL emitted by a light source. The unit of luminance is candela per unit area (cd m^{-2}). The candela (cd) quantifies the intensity of light radiation, which is also quantified in terms of luminous power (lumen, lm), a unit of power associated with light radiation.

EL efficiency

The EL efficiency can be quantified through external quantum efficiency ($\eta_{external}$, EQE), which measures the quantity of photon emissions from the QLED relative to the number of injected carriers. This includes internal quantum efficiency ($\eta_{internal}$, IQE), a parameter that characterizes the effectiveness of charge carrier injection and exciton generation. The IQE is described by factors encompassing exciton generation, charge balance ratio, and the PLQY of the emission material.

$$\eta_{internal} = \textit{exciton generation factor} \cdot \textit{charge balance factor} \cdot \textit{PLQY} \quad (1.7)$$

Out-coupling efficiency ($\eta_{out\text{-}coupling}$) refers to the proportion of photons extracted from within the device structure, typically ranging from 20 % to 30 %. This encompasses the interactions of photons within the device structure, including phenomena like cavity effects, reflection and refraction of light across the multi-stacked layers. Overall, EQE can be defined as a combination of factors including:

$$\eta_{external} = \eta_{internal} \cdot \eta_{out\text{-}coupling} \quad (1.8)$$

Current efficiency (CE) and power efficiency (PE) serve as additional metrics for assessing device efficiency. These metrics are derived from measurements of device luminance, current, and voltage. Current efficiency (CE) is characterized by the radiative recombination

within the current flow and is expressed in candelas per ampere (cd A^{-1}). On the other hand, power efficiency (PE) quantifies luminance efficiency relative to power consumption and is represented in lumens per watt (lm W^{-1}), calculated as the product of current and voltage.

EL stability

Next, device stability is a measurement of how effectively and consistently QLEDs uphold their EL efficiency throughout their operational lifespan. EL stability is determined through the EL lifetime, gauged by changes in luminance during actual device operation involving applied bias or current flow. Typically, the 50 % lifetime projection is utilized, indicating the duration for the relative luminance to decline to half of the initial luminance (L_0). This specific point in time is represented as LT50 and follows the established accelerated Coulombic degradation scaling rule,[40] a principle established through empirical research across the history of LED development.

$$\mathrm{LT50} \cdot L_0^{n} = \mathrm{constant} \tag{1.9}$$

where n is an accelerator factor determined by degradation mechanisms. The parameter n is introduced to adjust the projected LT50 value, which can vary within the range of 1.5 to 2.5, contingent on the degradation mechanism. This correlation is applicable to the LT50 estimation for QLEDs. By employing this correlation, the projected LT50 can be extrapolated across various L_0 and thereby facilitate direct comparisons of LT50s among diverse QLEDs featuring different efficiencies.

1.4 Challenges

Significant efforts have been devoted to enhancing QLED performance over the past three decades, achieving notable advancements. However, challenges persist in terms of their commercial viability. Current research advancements in QLED technology have yielded high device efficiencies, surpassing 20 % EQE in red-,[20,21] green-,[22,23] and blue-QLEDs.[23-25] Yet,

for successful commercialization, addressing the issue of QLED stability remains imperative. Despite notable progress and proposed solutions for achieving highly stable QLEDs using specific materials and conditions,[41-49] clear solutions remain elusive due to the intricate challenge of pinpointing the precise factors causing device degradation over extended operational periods and under varying external conditions. Consequently, achieving a comprehensive understanding of degradation mechanisms and the determinants influencing device lifespan is crucial. This thesis predominantly centers on introducing a significant enhancement in QLED stability through novel modification techniques applied to the ZnO ETL, as well as comprehending the mechanisms underlying QLED degradation and the restricted EL lifetime attributed to the ZnO ETL.

1.5 Thesis Overview

This thesis comprises eight chapters.

Chapter 1 serves as an introduction to QDs and their applications in LEDs. This chapter covers the operational mechanisms of QLEDs, their structural components, and how they have evolved concerning material selection and deposition order. Additionally, major performance metrics of QLEDs including luminance, EL efficiency, and stability are introduced. The chapter concludes by discussing the challenges associated with the stability of QLEDs.

Chapter 2 presents a comprehensive literature review on QLED stability issues, categorizing them according to the layers within QLEDs, along with the proposed potential solutions.

Chapter 3 outlines the research objectives and methodology employed in this work. The research aims, experimental methodologies, device architecture, fabrication process, and characterization techniques are all described in detail.

Chapter 4 delves into novel strategies for enhancing QLED stability through ZnO modifications. This section presents experimental outcomes showcasing significant improvements in EL stability through techniques such as the use of ZnO:PEI nanocomposites, carbon tetrafluoride plasma treatment on ZnO (FZnO), and the incorporation of I_2 and $FeCl_3$ dopants into ZnO (I_2:ZnO and $FeCl_3$:ZnO).

Chapter 5 explores the underlying mechanisms behind the improved EL stability achieved via ZnO:PEI and FZnO modifications. The chapter primarily focuses on experimental findings concerning the reduction of accumulated charges at the interface between the QD EML and HTL.

Chapter 6 continues the investigation into the mechanisms enhancing EL stability, specifically those resulting from the incorporation of I_2 and $FeCl_3$ into ZnO. Experimental results highlight the reduction of positively charged ZnO species and their implications.

Chapter 7 delves into the EL characteristics of green- and blue-QLEDs treated with halide-modified ZnO materials.

Chapter 8 concludes the thesis by summarizing its key points and outlining directions for future research.

In order to ensure clarity regarding authorship, the convention of using "we" rather than "I" will be employed throughout the remaining chapters. Furthermore, the contributions made will be acknowledged at the outset of each respective chapter.

Chapter 2 Comprehensive Literature Review on the Stability Issues of QLEDs and the Proposed Solutions

The advancement of QD EML and CTL has yielded remarkable progress in enhancing device efficiency. This progress is rooted in a deep understanding of the emission process within QD EMLs and the intricate interplay of charge transport and injection across QLEDs. However, while strides have been made in boosting device efficiency, the parallel development of device stability has faced some lag. Despite achieving impressive lifetimes in red- and green-QLEDs that occasionally rival those of OLEDs (LT50 at 100 cd m^{-2} of 3,000,000 hours[50]), these achievements often require intricate fabrication processes involving specially designed substrates,[51] and carefully controlled synthesis methods for QDs and organic materials.[23] Understanding the intricate mechanisms of device degradation remains a challenge due to its gradual occurrence over prolonged operational periods, influenced by diverse external conditions.[41,48,49] EL stability is influenced not only by factors related to emission, charge transport, and injection but also by changes in material properties and the degradation of individual materials through processes such as phase transitions, corrosion, decomposition, and redox reactions. These material changes can be triggered by various external factors, including oxygen, moisture, photoexcitation, and electrical excitation. In this chapter, a comprehensive review of selected issues concerning QLED degradation is presented, with a specific focus on QD EML, organic HTL, and ZnO ETL. Additionally, proposed solutions for addressing these stability challenges are discussed.

2.1 Photoluminescence Stability of QD Emission Layer

One critical issue that affects the stability of QLEDs is the PL stability of QDs. As a light-emitting device, maintaining the stable luminescence of QDs is paramount for the operational stability of QLEDs. While many publications have reported achieving nearly 100% PLQY of QDs, the luminescence stability of QDs is often hindered by unstable PL characteristics, most notably PL blinking.[52-55] Specifically, PL blinking refers to an unstable

luminescence characteristic exhibited by QDs. It manifests as intermittent fluctuations in PL intensity, where the emission intensity randomly alternates between higher intensity (bright state) and lower or zero intensity (dark state). This phenomenon is frequently observed in single-dot or isolated QD samples. One widely accepted explanation for this behavior is the formation of a trion within the QDs. A trion is an entity consisting of an excess charge in addition to an electron-hole pair, which can exist in negatively or positively charged states. Trions provide an alternative PL decay channel through the Auger recombination process. The formation of trions can arise from an uneven distribution of electron and hole wavefunctions within the QDs, as well as an imbalance in charge carriers within the QDs. This section delves into mechanistic explanations for the unstable PL properties of QDs from various perspectives.

2.1.1 Auger Recombination in QDs

Auger recombination is a process in which the recombination energy of an electron-hole pair is transferred to a third particle, and this energy is predominantly released through non-radiative recombination. In bulk materials, both energy and momentum conservation rules must be satisfied for Auger recombination to occur. However, in the case of QDs with an atomic-like structure, as described in sub-section 1.2.1, the translational symmetry is broken, and thus the momentum conservation rule is relaxed. This relaxation enables the efficient transfer of energy to the third particle. In the context of QDs, the presence of trions can lead to a higher probability of energy relaxation via Auger recombination. The Auger recombination process, when involving trions, contributes to the loss of photon energy and has been identified as a key factor in the occurrence of PL blinking in QDs.

In 1996, Brus et al. were the first to propose that ionization of CdSe QDs contributes to PL blinking through Auger recombination[52]. They conducted experiments to investigate the increase in the occurrence of 'dark states' in sparsely-packed CdSe QDs by raising the excitation intensity. To achieve this, they embedded the QDs in a polymer matrix (e.g., PMMA

and polyvinylbutyral) by blending a diluted QD solution. The results suggested that ionized QDs undergo non-radiative energy relaxation via Auger recombination, which leads to the phenomenon of PL blinking that depends on the excitation intensity. Subsequent studies further corroborated their findings and provided more evidence for PL blinking caused by Auger ionization. Since then, researchers have commonly employed a single-dot experimental spectroscopy setup and fluorescence lifetime-intensity correlation to investigate the characteristics of PL blinking. Galland et al. utilized fluorescence lifetime-intensity analysis along with an electrochemical approach to explore the relationship between PL intensity and PL lifetime.[54] By measuring the PL of both 'bright' and 'dark' states individually, they revealed the charging and discharging behavior resulting from Auger recombination in CdSe/CdS QDs. Yuan et al. successfully explained the charging and discharging process in CdSe/CdZnS QDs through the application of lifetime scaling and the analysis of PL fluctuation trajectories combined with lifetime-intensity distributions.[56] By using the PL fluctuation trajectory alongside the extracted PL lifetime values of τ_X (bright state) and τ_{X^*} (dark state) (where τ_{Xr} and τ_{X^*r} indicate the radiative lifetimes of each state), the radiative lifetime scaling factor of these fluorescence states can be determined[56]

$$\frac{\tau_{Xr}}{\tau_{X^*r}} = \frac{\tau_X}{\tau_{X^*}} \frac{I_{X^*}}{I_X} = 2 \tag{2.1}$$

The extracted factor of ‘two’ indicates that two electrons (or holes) recombine with one hole (or electron) in the PL mechanism, implying the involvement of trion recombination.[57] Their model effectively elucidates the mechanism behind QD PL blinking through the Auger process mediated by trions.

Given that the overlap of the electron-hole wavefunction across the energy structure of QDs significantly influences the interaction of charge carriers, the energy structure of core-shell QDs has been investigated to understand the loss of charge carriers in QDs. Resonant tunneling from core materials to surface states through shell materials has been proposed as a potential cause of the 'dark state' observed in PL blinking. The substantial surface-to-volume

ratio and incomplete passivation of surface states facilitate the overlap of wavefunctions within these states. This can result in charge carriers within the core materials being expelled and trapped by the surface states, ultimately leading to a reduction in PL intensity. The occurrence of the 'dark state' attributed to resonant tunneling can be predicted using the fluorescence lifetime scaling factor.[56]

$$\frac{\tau_{Xr}}{\tau_{X^*r}} = \frac{\tau_X}{\tau_{X^*}} \frac{I_{X^*}}{I_X} = 0.96 \tag{2.2}$$

Unlike the scaling factor observed in the relaxation of the trion (2.1), the factor is close to one, indicating a distinct relaxation channel. This factor elucidates an alternative potential relaxation pathway involving non-radiative recombination through the escape of charges into surface trap states. This can be attributed to inadequate charge carrier confinement arising from an incomplete core/shell structure and inadequate passivation of surface states.

2.1.2 Environmental Factors affecting PL stability of QDs

The unstable PL characteristics of QDs can be influenced by ambient conditions, such as the presence of O_2 and H_2O, due to their potential impact on the ionization of the QD material. Xiaogang Peng group has extensively studied the effects of environmental factors on the PL characteristics of CdSe-QDs. Their research has explored how O_2 and H_2O affect the stability of PL in CdSe/CdS QDs.[58] In their study on O_2 effects, they compared single-dots and ensembled QDs under both O_2-rich and inert (Ar-filled) conditions. The results showed that O_2 has a stabilizing effect on the PL intensity trajectory of QDs. Specifically, the ratio of bright states in the PL trajectory of QDs increased in the presence of O_2. This phenomenon can be explained by O_2's strong electron-accepting property, which effectively deionizes negatively charged QDs, including the relaxation of negative trions. The results indicated that O_2 does not have a detrimental impact on the PL intensity of QDs; instead, it stabilizes the PL by reducing photo-redox reactions within the QDs. Subsequently, the same group investigated the impact of H_2O molecules on the PL of the QDs.[59] Through systematic experiments controlling the conditions of H_2O and O_2, they supported the idea of a photochemical process occurring in the

QDs due to the presence of both O_2 and H_2O molecules. Interestingly, H_2O acted as an electron donor, contrary to the electron-accepting property of O_2, and drove a photo-reduction process in the QDs. Overall, O_2 and H_2O were found to have complementary effects on inducing photo-redox reactions in QDs. Specifically, H_2O induced ionization, resulting in dark states, whereas O_2 deionized the QDs, leading to bright states. While this work provides valuable insights into the possible mechanisms underlying the unstable PL blinking of QDs caused by environmental factors, their model is currently limited to single dots or QD films. Further investigation is necessary to understand the behavior of QD EML in QLED operation.

2.2 Charge Transport Materials

The stability of the EL process in QLEDs is heavily influenced by the properties of the charge transport materials. The efficient and stable generation of excitons within the QD EML relies on the stable injection of charges, which in turn contributes to stable luminescence. If the injection of electrons and holes is not balanced, it can lead to the formation of trions in the QD EML. Therefore, achieving balanced charge injection into the QD EML during device operation is contingent on optimizing the charge transport and injection characteristics of each CTL. Additionally, accumulation of charges at heterointerfaces between different layers can lead to non-uniform charge distribution and affect the device performance. Loss of charge carriers through recombination within the CTLs can further exacerbate these issues. In this section, the stability issues in QLEDs related to the HTL and ETL will be introduced.

2.2.1 Charge Imbalance in the QD EML by Uneven Injection Rate of Electron and Hole

Energy barriers at the interface between the CTL and the QD EML are inevitable due to the disparity in their energy levels. In the case of CdSe QDs, holes generally require more energy to overcome the energy barrier at the QD EML/HTL interface compared to electrons at the ETL/QD EML interface. This discrepancy arises primarily from the lower energy barrier at the ETL/QD EML interface. As depicted in Figure 1.9, the conduction band minimum (CBM) of ZnO exhibits a better energy level alignment with the CBM of CdSe, while the highest

occupied molecular orbital (HOMO) levels of most organic materials are shallower than the valence band maximum (VBM) of CdSe. This energy level mismatch leads to an uneven charge injection into the QD EML, resulting in diminished QLED lifetime and efficiency.[60] Additionally, the higher electron mobility of ZnO (2×10^{-3} $cm^2V^{-1}s^{-1}$) compared to that of most organic hole transport layers (typically < 1×10^{-4} $cm^2V^{-1}s^{-1}$) can result in imbalanced charge transport and injection into the QD EML.

2.2.2 Degradation of Organic Materials

Organic materials are inherently susceptible to degradation caused by factors such as UV excitation, electrical stress, radical species, moisture, and oxygen. Additionally, interactions with charges can initiate various degradation reactions in organic materials.[48,61,62] The degradation of organic HTLs can therefore emerge as a prominent contributor to device deterioration. An investigation into UV-induced exciton-induced degradation of organic HTLs has been reported.[42] This study examined changes in the PL intensity of QDs when in contact with different HTLs (CBP, NPB, spiro-CBP, mCP, and 2,6-DCzPPy) under UV excitation. The PL *vs.* time curves exhibited the gradual energy transfer of excitons from the HTL to the QDs over time, along with exciton quenching in the QDs due to exciton-induced degradation of the HTL. Particularly, the presence of an exciton quencher near the QD EML/HTL interface led to the loss of recombination energy of the excitons in the QDs. Spiro-CBP was found to be vulnerable to exciton-induced degradation, potentially explaining the shorter lifetime of QLEDs employing spiro-CBP compared to CBP. This outcome provides insight into a device degradation mechanism associated with exciton formation within the HTL due to leaked and accumulated charges. Another study delved into the consequences of electron leakage into the HTL.[63] This experiment observed two distinct stages of degradation patterns. In the initial hours of device operation, the QLED exhibited reduced EL efficiency due to negative charging of QDs caused by an excessive influx of electrons from the ETL. Concurrently, the organic HTL underwent damage during extended device operation due to electron leakage stemming from an excess of electrons in the QD EML. A cross-sectional transmission electron

microscope (TEM) image of a QLED after 90 hours of operation revealed alterations in the morphology of the HTL material CBP, which could result in the loss of its electrical properties. The diminishment of the HTL's electrical properties was observed to directly lead to EL loss in QLED operation. Arakawa et al. established a connection between the mobility of hole transport materials and QLED lifetime, suggesting that the degradation of hole transport and injection ability significantly contributes to EL loss in their QLEDs.[43] While the exact cause of the reduction in hole transport properties may be debated, these studies imply potential reactions occurring within the HTL during device operation that have a substantial impact on the stability of the device's electroluminescence.

The degradation of organic materials is not limited to the organic HTL; it also extends to the organic ligands attached to the QDs. Specifically, the organic ligands that are loosely bound to the surface of the QDs are susceptible to undergoing a decomposition process.[64-67] When these organic ligands decompose and lose their functional properties, the QDs become susceptible to various reactions that lead to irreversible changes in their material characteristics. Pu et al. conducted research into the instability of the EL in QLEDs featuring CdSe/CdS QDs, attributing the issue to the carboxylate ligands on the QDs' surface.[64] The authors identified the weakly bonded carboxylate ligands as the primary cause of the low EL stability. These carboxylate ligands can become detached during electrical stress, thereby exposing the QDs to subsequent electrochemical reactions.

2.2.3 Accumulation of Charges at Heterointerfaces

The intrinsically shallower HOMO level of organic hole transport materials (typically, 5 eV~6 eV below the vacuum level) compared to the VBM of the QD materials (6.2 eV~6.5 eV below the vacuum level for CdSe QDs) creates a substantial energy barrier. This barrier leads to the accumulation of holes at the interface between the QD EML and the organic HTL. The presence of accumulated holes at this interface significantly increases the probability of interactions with organic materials, including the organic HTL and the organic capping ligands surrounding the QDs. For instance, a material like CBP exhibits a redox potential close to its

HOMO energy level, suggesting that accumulated holes possess sufficient energy to facilitate redox reactions.[68] Furthermore, these accumulated charges can generate radical species through interactions, a phenomenon that has been observed before.[68] Radical species are highly reactive entities capable of self-decomposition or reacting with nearby organic molecules or atoms.

Song et al. investigated the effects of interfacial interactions on the degradation of QLEDs.[41] Their findings suggested that the differing degradation patterns observed in red and blue QLEDs could be linked to the accumulation of charges at distinct interfaces. To assess this, they employed an electro-absorption (EA) measurement to quantify the voltage drop across individual layers within the devices. Interestingly, their results highlighted a significant voltage drop across the ZnO ETL in the blue QLED, while both red and blue QLEDs exhibited the emergence of positively charged hole transport materials. These observations indicated that the degradation of QLEDs could be linked to the accumulation of charges at interfaces between the QD EML and HTL, as well as between the ZnO ETL and QD EML. Although their findings provided evidence of device degradation due to the accumulation of charges throughout QLEDs, further investigations are necessary to uncover the precise mechanisms operating at these heterointerfaces.

2.3 Intrinsic Defects in ZnO Electron Transport Materials

Several potential factors can contribute to the degradation associated with ZnO materials. Firstly, ZnO's high electron mobility and small energy barrier with QDs can result in an excessive influx of electrons into the QD EML. Additionally, the presence of stoichiometric and structural defects within ZnO creates various sub-bandgap states, complicating the precise estimation and optimization of charge injection at the interface.[33-35,69] In this section, potential mechanisms that govern the stability of QLEDs arising from ZnO and its derivatives are reviewed.

2.3.1 Defect-mediated Charge Trapping and Exciton Quenching

The presence of sub-bandgap states stemming from stoichiometric and structural defects in ZnO materials can significantly impact the QLED stability. The ZnO structure encompasses various forms of structural defects, e.g., oxygen/zinc vacancy, oxygen/zinc interstitial, and hydroxyl groups. These defects offer charge carriers favorable energy states and pathways for electronic transitions, as illustrated in Figure 2.1. Notably, the exciton can split into the electron and hole and these defect states can capture these charges. Particularly, Wannier-Mott type excitons in the QDs are especially susceptible to dissociation due to the electric fields, influenced by the high dielectric constant that reduces the Coulombic interaction between electrons and holes.[70] Multiple studies have observed a substantial decrease in the photoluminescence quantum yield (PLQY) of QDs upon interaction with a ZnO film.[45,71,72] Although the exact type of defect responsible for the PLQY reduction remains uncertain, oxygen vacancies (V_O) are believed to be a major contributor among the array of defect states.[36,45] These V_O can act as both electron and hole trap states. Fundamentally, oxygen vacancies create unpaired zinc ions with positively charged states (i.e., Zn^+ or Zn^{2+}), attracting electrons.[37,45,73] On the other hand, singly charged oxygen vacancies (i.e., V_O^+) can serve as trapping sites for holes.[74-76] Noticeably, the energy required to trap holes through oxygen vacancies aligns closely with the VBM of CdSe, suggesting accessible states for holes within the CdSe. In either scenario, the energy states associated with oxygen vacancies can lead to exciton quenching and subsequent charge trapping at the ZnO/QDs interface.

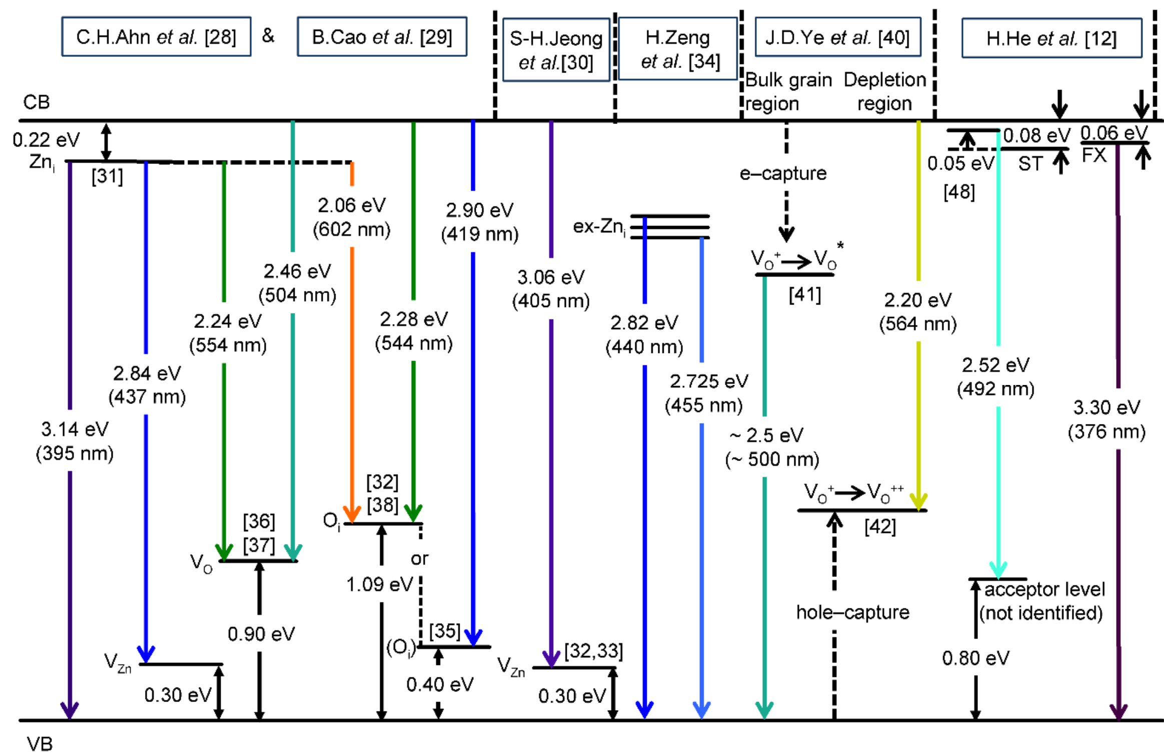

Figure 2.1 Energy level diagram showing some of the principal defect levels in ZnO. Reproduced with permission. Copyright 2012, Springer Nature[76].

2.3.2 Formation of Charged Species in ZnO

The ZnO can be significantly affected by charge accumulation and its interaction with charges. Various studies have reported the presence of charged species within ZnO and ZnMgO materials during the operation of QLEDs. More recently, a transient EL experiment was conducted to examine the capacitive charging behavior across QLEDs.[77] In the experiment, a DC offset voltage (V_{offset}) was applied before the driving voltage (V_D) to explore the impact of the voltage pulse profile on the EL process. The delay time of EL onset (t_d) *vs.* V_{offset} followed the relationship[77]

$$t_d = \frac{d^2}{\mu \cdot V_D} + \tau \cdot (\ln \frac{V_D - V_{offset}}{V_D - V_{inj}}) \tag{2.3}$$

where μ is the carrier mobility, d is the distance of carrier transverse, and V_{inj} is applied voltage for initiating electron injection. The first term generally represents the delay time between a square pulsed bias and the onset of EL, mainly due to the time it takes for carriers to reach the QD EML. The second term indicates the capacitive charging behavior of the QLED during the measurement. The author attributed the charging process during device operation to the penetration of Zn species into the QDs either during or after the fabrication. Another study observed a resistive switching behavior of ZnMgO.[47] Hysteresis in the J-V characteristic was observed in the ZnMgO-device, indicating an ionic process involving the migration of ions during QLED operation. This suggests electrochemical reactions within the ZnMgO caused by external bias, indicating an interaction with injected charge carriers. The author explained this resistive switching behavior as an electroforming process, which releases active oxygen species due to a redox reaction. The off-lattice oxygen can gradually migrate toward the anode under external bias, resulting in higher conductivity. The reverse bias deactivates the off-lattice oxygen ions, restoring the normal state with lower conductivity. A similar process can be anticipated in the case of ZnO due to the structural and compositional similarities. Positive charging of ZnO is also suspected to contribute to QLED degradation. Chen et al. observed the transfer of holes from the QDs to the ZnO, promoted by surface-bound ethanol species.[78] Their transient absorption (TA) measurements revealed long TA kinetics from the QDs/ZnO with surface-bound ethanol, suggesting slow absorption bleaching in the QDs due to hole depopulation. This could result from the extraction of holes by the ZnO with the surface-bound ethanol.

In summary, numerous reports have indicated the presence of charging processes associated with the ZnO ETL and their impact on QLED operation. Therefore, effectively managing the charging processes originating from the ZnO is crucial for achieving highly stable QLED performance.

2.4 Proposed Solutions

2.4.1 Core-shell engineering

Modifying the core-shell structure of QDs is a critical step in altering the energy level landscape across the QDs, thereby exerting control over charge carrier dynamics within the QDs. This energy landscape essentially dictates the electron and hole wavefunctions within the QDs. Typically, shell materials possess a larger bandgap compared to the core materials, ensuring efficient confinement of charge carriers within the core (especially in the case of type-I structures). In such core/shell structures, the overlap of electron and hole wavefunctions governs processes like exciton formation, dissociation, and recombination. Furthermore, the effective carrier volumes, considering wavefunction overlap, dictate the rate of Auger recombination, often characterized by a volume scaling rule. The manipulation of core-shell structures has emerged as a predominant strategy in the pursuit of stable QDs.

Lattice mismatch between core and shell materials is a crucial factor to take into account when undertaking successful core-shell engineering. An established guideline for achieving optimal luminescence efficiency dictates that the lattice mismatch should not exceed 15 % to prevent excessive strain effects.[79] For instance, CdSe material typically exhibit a small lattice mismatch with ZnS (10.6 %)[80], ZnSe (6.3 %)[81], and CdS (3.9 %)[82], making these shell materials commonly utilized in core-shell engineering for the CdSe.

The Klimov research group has been dedicated to studying the PL characteristics of CdSe/CdS QDs and meticulously engineering the shell materials to mitigate the Auger recombination.[83] Noteworthy contributions by this research group include the implementation of gradient shell structures within the QDs (e.g., CdSe/CdSeS/CdS[39,84-86], CdSe/CdZnS[87], and CdSe/CdZnSe/ZnSeS[15,88,89]). The introduction of such shell structures theoretically leads to the suppression of the Auger recombination, a phenomenon predicted by Cragg et al.[90] The potential shapes of a core-shell structure play a pivotal role in determining the Auger process rate, as described by Fermi's golden rule[91]

$$k_A = \frac{1}{\tau_A} = \frac{2\pi}{\hbar}\int |M_{if}|^2\, \delta(E_{initial} - E_{final})dE \qquad (2.4)$$

$$M_{if} = \int \psi_{final}\, V \psi_{initial} \qquad (2.5)$$

where k_A and τ_A indicate the Auger process rate and lifetime, respectively, and M_{if} indicates the transition matrix. The M_{if} is expressed through an integral involving the initial state wavefunction $\psi_{initial}$, final state wavefunction ψ_{final}, and the potential V, as depicted in equation (2.5). By solving this equation through Fourier transformation, the final state wavefunction takes on different forms based on various potential confinements. In cases of abrupt potential confinement, the solution of the final state wavefunction is proportional to $(k_f \cdot a)^{-2}$, where k_f represents the wavenumber of the final state and a denotes the width of the potential box. On the other hand, for a parabolic potential shape, the wavefunction of the final state is proportional to $exp\,(-k_f{}^2 \cdot a^2/2)$. Consequently, a gradient potential profile with a parabolic shape across the core-shell structure yields an exponentially smaller M_{if} compared to an abrupt potential profile. The overall rate of Auger recombination is determined by $|M_{if}|^2$, indicating that a core with a gradient shell structure exhibits a lower rate of Auger recombination than a conventional core/shell structure. This theoretical prediction proposes the utilization of a gradient shell structure as an approach to achieve stable PL characteristics of QDs.

Another approach involves the implementation of a thick shell structure to address the loss of PL stability caused by resonant tunneling of charge carriers through the shell.[53] This approach was suggested to mitigate the loss of PL stability via the resonant tunneling of charge carriers through the shell. Mahler et al. proposed an adjusted synthesis procedure for CdSe/CdS QD structures. In their approach, they first synthesized a CdSe core and subsequently grew multiple layers of CdS sequentially. After multiple iterations of shell growth, a thick CdS shell was developed, covering the CdSe core. The increase in shell thickness effectively reduced PL blinking by decreasing the probability of resonant tunneling. The significance of shell

thickness was also observed in other QDs, such as InP/ZnSe/ZnS QDs. According to a *Samsung*'s publication, the thickness of the ZnSe shell in InP/ZnSe/ZnS QDs was shown to strongly impact the EL lifetime of QLEDs.[92] Their study unveiled that a thick shell inhibits energy transfers between QDs as well as Auger recombination. The selection of an appropriate shell material is also crucial for achieving the optimal energy structure of core-shell quantum dots. Some reports have indicated that a smaller bandgap (E_g) of ZnSe shell can offer better alignment with CdSe than ZnS with a larger E_g, potentially facilitating carrier injection.[93]

2.4.2 Ligands engineering for QDs

Optimizing the physicochemical properties of the surfaces of QDs is crucial due to their substantial surface-to-volume ratio. Ligands are artificially introduced onto the QD surfaces to create steric hindrance, which serves to stabilize the colloidal state of the QDs by suppressing intermolecular reactions and passivating dangling bonds. Each ligand consists of an anchoring group and a functional tail, as schematically depicted in Figure 2.2. The functional tail, along with a hydrophilic segment, enhances the dispersibility of QDs in a colloidal state, rendering the QD surface hydrophilic for stable dispersion in nonaqueous media. Ligands also reduces electronic coupling in densely packed QDs. The presence of ligands reduces the loss of recombination energy via Förster energy transfer among the QDs. Therefore, ligands play a crucial role in both ensuring a stable emission process in QDs and the formation of a stable structure.

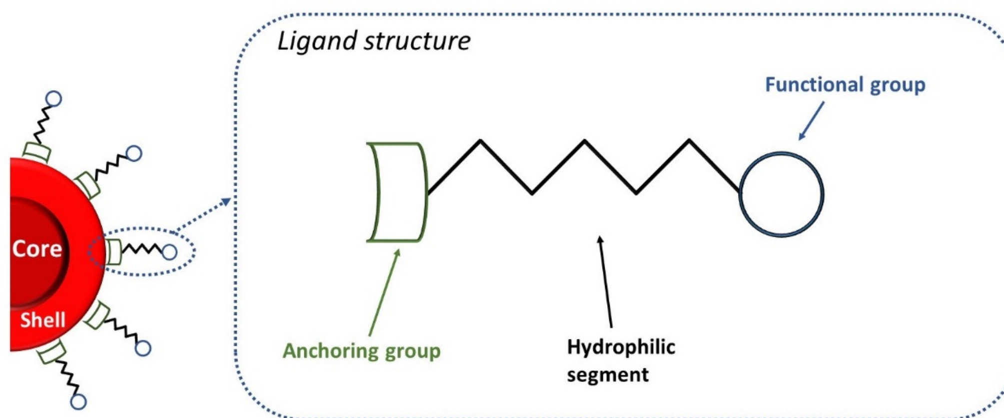

Figure 2.2 Schematic illustration of the core-shell QDs with ligands. The ligand structure is also represented.

Numerous ligand structures have been proposed to ensure the stable luminescence of QDs. For achieving stability in QLEDs, it is essential that the ligands are electrochemically stable. Pu et al. demonstrated that the appropriate ligand choice could enhance the QLED lifetime.[64] As previously discussed in subsection 2.2.2, CdSe/CdS QDs with carboxylate ligands are vulnerable to ligand termination under electrical stress. By substituting carboxylate ligands with fatty amine ligands, Pu and colleagues increased the bonding strength between ligands and the CdS surface, mitigating termination of the bond due to electrical stress. Consequently, utilizing QDs with fatty amine ligands extended the EL lifetime of the QLED. Other studies have emphasized the significance of ligand resistance to Joule heating. QLEDs can be susceptible to Joule heating during operation, given the presence of non-radiative recombination processes that may dissipate energy as thermal energy. This thermal energy can potentially decompose organic materials within the QLED. To address this issue, 1-dodecanethiol (DDT) ligands were employed for their resilience against Joule heating.[94] Implementation of DDT ligands in the QD EML improved the operational stability of the

QLED. Additionally, alkylthiol materials, like 1-octanethiol, have been suggested to enhance PL stability.[95] Alkylthiol-induced surface reconstruction led to a reduction in residual surface traps.[96] Inorganic ligands such as halides and metal complexes have also been considered for QDs.[24,97,98] These inorganic ligands typically exhibit high conductivity, unlike organic ligands.[99] For example, the utilization of chloride ligands with CdSe/ZnS QDs facilitated charge carrier injection, minimizing hole accumulation and suppressing the Auger recombination.[98] However, introducing inorganic ligands to QDs in QLEDs poses challenges due to their strong electronic coupling with the QDs,[100,101] which can significantly impact radiative recombination within the QDs.

2.4.3 HTL engineering

The challenges posed by relatively lower carrier mobility of organic hole transport materials compared to the electron transport materials, along with their intrinsic instability, are significant hurdles to overcome. As a result, the strategies for engineering the HTL primarily focus on two key approaches: (1) achieving a balanced charge injection rate into the QD EML and (2) enhancing the material stability and robustness.

The first approach involves the careful selection of appropriate materials based on their energy levels and hole mobility. In order to achieve efficient hole transport and injection into the QD EML, certain materials like CBP and TFB are commonly employed in inverted and upright QLED structures, respectively. These materials are chosen due to their favorable hole transport and injection characteristics. However, to address the issue of QLED lifetime, additional modifications are often necessary. Small molecule organic HTL materials, e.g., CBP and TCTA, are widely utilized in inverted QLED structures due to their excellent hole transport and injection properties, attributed to their deep HOMO levels.[45,46,51,102] Nonetheless, the operational stability can sometimes be constrained by CBP's relatively low glass transition temperature (T_g) of 62 °C and susceptibility to material degradation caused by excessive charges. To solve this issue, the co-deposition of CBP and 2,2'-bis(4-(carbazol-9-yl)phenyl)-biphenyl (BCBP) to form a mixed HTL was proposed.[103] The BCBP possesses a relatively

shallower LUMO level and a higher T_g of 173 °C in comparison to CBP. The mixed HTL takes advantage of both materials, facilitating efficient hole injection from CBP while benefiting from the electron blocking capability and resistance to joule heating provided by BCBP. This approach demonstrated a substantial extension in QLED lifetime, with a LT70 of over 2,000,000 hours at 100 cd m^{-2}. Another innovative approach involved the implementation of cascaded HTLs to mitigate the accumulation of holes near the interface between QDs and the HTL. The large hole injection barrier between QDs and CBP can lead to the build-up of holes at this interface. This accumulation of holes not only affects the electrical characteristics of CBP but also has potential repercussions on QD stability through various processes. To address this challenge, a cascaded HTL configuration was proposed, featuring layers of CBP, TCTA, and NPB. This design creates heterojunctions within the HTL, effectively distributing the accumulated holes across the entire HTL structure.[102] By introducing such a cascaded HTL into the QLED device architecture, the QLED demonstrated a remarkable 25-fold increase in LT50 at 100 cd m^{-2} compared to the control device, which employed a QLED with CBP as the HTL material. Researchers have explored the implementation of step-wise HTLs composed of various material combinations, e.g., poly-TPD/PVK,[104] TCTA/NPB,[105,106] and CBP/mCP.[107,108] These structures capitalize on the synergistic effects arising from the optimal combination of mobility and HOMO level of each constituent material, leading to enhanced hole injection and transport processes. For instance, the use of poly-TPD in combination with PVK offers a strategic approach to leverage the higher mobility of poly-TPD (10^{-4} $cm^2V^{-1}s^{-1}$) compared to PVK (10^{-6} $cm^2V^{-1}s^{-1}$), along with the deeper HOMO level of PVK (5.8 eV) as compared to poly-TPD (5.4 eV). Likewise, the pairing of TCTA and NPB in the step-wise HTL structure serves to overcome energy barriers between QD EMLs and HTLs, courtesy of TCTA's deep HOMO level (5.8 eV), while NPB contributes to a high hole current density.

The polymeric TFB stands out as a favored choice for the HTL in the upright QLED configuration due to its high hole mobility.[23,78,109] However, its suitability can be affected by factors such as the substantial hole injection barrier resulting from its HOMO level and limited

chemical robustness. Researchers have put forth various strategies to enhance the stability of QLEDs utilizing TFB, and some notable approaches are proposed. One effective strategy involves chemical treatments applied to the HTL or HTL/HIL (hole injection layer) interface. For instance, the treatment of TFB with 2,3,5,6-tetrafluoro-7,7,7,7,-tetracyanoquinodimethane (F_4TCNQ) has been proposed.[110] This treatment enhances hole conductivity by increasing hole concentration and diminishing the hole injection barrier, thus addressing charge imbalance within the QD EMLs. Ionic liquid treatments at the PEDOT:PSS/TFB interface have also been explored for enhancing hole transport and injection.[111] By introducing AgTFSI and LiTFSI modifications, the charge balance within the QD EML is improved through enhanced hole injection, aided by the role of these ions in increasing hole concentration. In light of potential limitations associated with the polymeric nature of TFB, alternative materials have been investigated. The polymeric structure of TFB may contribute to electron leakage due to its energetic disorder.[23] Poly((9,9-dioctylfluorenyl-2,7-diyl)-alt-(9-(2-ethylhexyl)-carbazole-3,6-diyl)) (PF8Cz) has been found to successfully extend the lifetime of green and blue QLEDs compared to TFB-based counterparts by suppressing electron leakage.[23] Another promising alternative is 9,9-Bis(4-((4-ethenylphenyl)methoxy)phenyl)-N2,N7-di-1-naphthalenyl-N2,N7-diphenyl-9H-fluorene-2,7-diamine (VB-FNPD), which boasts greater chemical robustness compared to TFB, potentially offering improved stability for QLED applications.[109]

Numerous studies have focused on addressing the limitations of organic HTLs in QLEDs to achieve longer device lifetimes. Approaches include selecting appropriate materials, modifying HTLs for stability, and utilizing cascaded or step-wise structures. Chemical treatments and alternative materials have also been explored to enhance QLED performance. These strategies collectively aim to improve QLED stability and ensure their viability for practical applications.

2.4.4 ETL engineering

Compared to organic HTL, less attention has been given to the stability issues stemming from electron transport materials like ZnO, owing to the perception of ZnO's high

thermodynamic stability.[33,112,113] Nevertheless, there have been instances of QLED stability enhancement through ZnO modifications. General strategies for ZnO modifications include: (1) Tailoring the electron transport and injection properties of ZnO to achieve improved charge balance within the QD EML, similar to HTL engineering. (2) Mitigating exciton quenching caused by trap states within ZnO.

An effective approach involves incorporating insulative buffer layers between the ZnO ETL and QD EML to diminish electron injection efficiency. The first instance of success was the use of a poly(methyl methacrylate) (PMMA) layer as a buffer at the ZnO/QDs interface, which greatly improved device efficiency as demonstrated by Dai et al.[21] Since then, various materials such as polyvinylcarbazole (PVK),[114] Al_2O_3,[115,116] and polyethylenimine (PEI),[107,117,118] have been proposed as buffer layers to enhance QLED performance. These buffer layers serve to decrease electron injection into the QD EML and to passivate interfacial trap states at the ZnO/QDs interface.

Doping ZnO is another effective strategy for tuning the electrical properties of ZnO.[119] Various materials, such as Y,[120] Li,[121] and Mg,[122] have been explored as dopants for ZnO. Y doping in ZnO reduces electron mobility, enhancing charge balance within the QD EML. Similarly, introducing Li into ZnO can alter electron mobility, leading to extended QLED lifetime. Mg-doped ZnO is widely used as an electron transport material in QLEDs. ZnMgO offers better charge injection rate balance with organic HTLs due to lower electron concentration. Mg doping widens the E_g of the ZnO[123-125] and reduces defect states,[126,127] thereby improving radiative recombination within QD EML, boosting device efficiency and stability. Various modifications to ZnMgO, such as using materials, e.g., Rb_2CO_3,[128] spiro-OMeTAD[129] and TBS-PBO,[130] have been proposed to further enhance QLED lifetime.. Strategies like incorporating Li into ZnMgO[131] and alloying ZnO with ZnMgO[132] have also been suggested. These ZnO-related strategies primarily focus on reducing electron transport and injection properties of ZnO materials to attain improved charge balance within the QD EML.

Ligand engineering for ZnO NP has also been suggested as a strategy.[78] The presence of surface-bound ethanol in ZnO NPs can act as a hole scavenger, readily capturing holes. To enhance QLED lifetime, LiAc ligands were introduced onto the surface of ZnO NPs. This approach effectively decreased the surface-bound ethanol species, preventing the build-up of positive charges within the ZnO, thus contributing to improved device stability.

Other metal oxides, e.g., SnO_2,[133,134] ZrO_2,[135] and TiO_2,[136] have also been suggested as potential alternatives to ZnO for QLED applications. SnO_2 has demonstrated comparable QLED lifetime and efficiency to that achieved with ZnO ETL. However, surpassing the successes of ZnO materials requires further research and development, encompassing advancements in synthesis techniques, property enhancements, and device structure modifications, all while considering their electron transport properties.

2.5 Summary

Many research studies have presented strategies to achieve highly stable QLEDs. Core-shell QD structures and their ligand engineering have proven successful in improving the PL stability of QDs, effectively reducing PL blinking and enhancing the luminescence property of QDs. Engineering organic HTLs is another avenue to enhance QLED stability. Due to their susceptibility to degradation from various factors like interaction with charges and radicals, and electrical stress, significant efforts have been dedicated to developing organic hole transport materials, improving their properties, and using dopants to enhance their electrical characteristics.

The role of ZnO ETLs in QLED stability has often been overshadowed by the emphasis on QD structures and organic HTLs. However, some studies have shown promising results by modifying the ZnO ETL, including the introduction of buffer layers, surface treatments, and doping, leading to increased QLED lifetimes. A common thread in many investigations is the association of charge imbalance within the QD EML with limited QLED

stability. As a result, numerous ZnO modification strategies focus on improving charge balance within the QD EML. Nevertheless, finding a definitive solution to address limited EL stability remains a challenge.

Chapter 3 Research Objectives and Methodology

3.1 Research Approaches and Aims

The overarching objective of this work is two-fold: (1) exploring new approaches for modifying the ZnO ETL to improve device stability and (2) understanding the role of chemical treatments of ZnO in influencing device stability. Toward this goal, this PhD work does the following:

(a) Explores new approaches for modulating charge transport across the ZnO and passivating the defects in it with the purpose of improving device stability. The following approaches will be pursued: (i) adding polymer additives to the ZnO to change charge distribution across the QLED, and (ii) using chemical treatment to alter the stoichiometry and defect distribution via plasma and wet processes. These treatments address oxygen vacancies and/or charge trap states in the ZnO.

(b) Determines how the ZnO treatments impact device stability, ultimately elucidating how ZnO limits device stability. It studies the impacts of different additives in the ZnO ETL on device stability. Various investigation techniques are used to understand the role of dopants, e.g., estimating charge distribution, accumulation, and annihilation of charge carriers within QLED, probing recombination center, measuring exciton lifetime, measuring chemical and electronic states of materials across QLED.

3.2 General Methodology in the Experiments

3.2.1 Device Architecture and its Fabrication Process

This work uses the inverted hybrid QLED structure for systematically investigating the impact of ZnO modifications. The fabrication procedure, therefore, is designed to solely modify ETL while avoiding any impact on the QD EML and HTLs. Indium tin oxide (ITO) is pre-patterned on a glass substrate (Kintec) for providing 4 mm^2 of active device region. The

schematic image of the ITO substrate is depicted in Figure 3.1 (a). The ITO substrate is thoroughly cleaned by Micro 90 cleaning solution (Cole-Parmer), acetone, and isopropanol by using a cleanroom level swab (TX758B, AlphaSeries). The possible organic contaminants are then further removed by a plasma treatment. The substrate is treated by using oxygen plasma with 20 sccm of O_2 gas injection, and generated by 50 W for 300 seconds (Phantom RIE, Trion technology). ZnO ETL is deposited on the ITO substrate, followed by the modification process. QD EML and HTL are sequentially deposited following the ZnO ETL deposition. The overall fabrication sequence is in order : (i) ETL deposition/modification → (ii) EML deposition → (iii) HTL/HIL deposition → (iv) electrode deposition → (v) device characterizations. The ETL modification is done in either the step (i) or a solution preparation step before ETL deposition. This provides a great latitude in various ETL modifications without the constrains of possible damaging the QD EMLs and HTLs. The effect of the ETL modification can be systematically investigated by comparing the QLEDs with ZnO *vs.* modified ZnO. The inverted QLED architecture used in this work is schematically shown in Figure 3.1 (b).

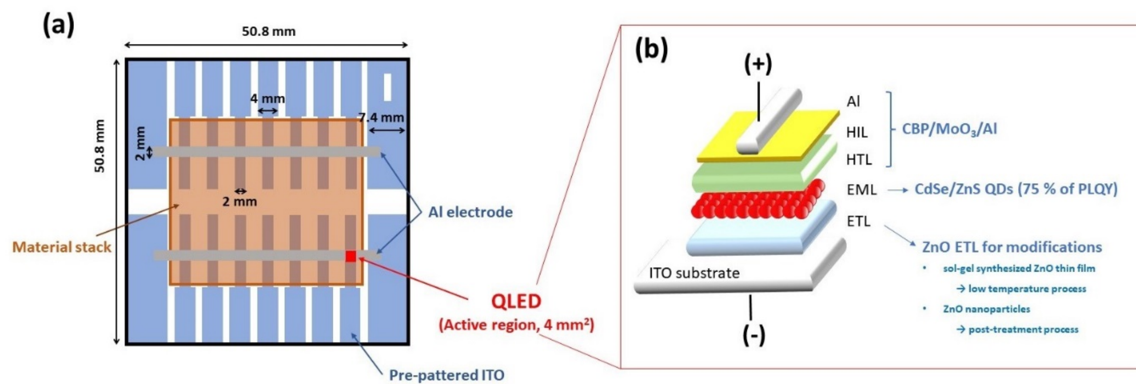

Figure 3.1 (a) Layout of the device substrate used in this work. (b) A schematic image of the inverted QLED.

CdSe/ZnS core/shell QDs for Emission Material

CdSe/ZnS core/shell QDs are selected for providing a consistent quantum yield and luminescence to exclusively investigate the effect of ETLs on device performance. Commercialized QD product from Mesolight Inc. (630 nm emission wavelength and 75 % PLQY) is chosen for providing an EML. This QD structure includes CdSe/ZnS core/shell and 1-octanethiol for a ligand material. The long chain structure of the 1-octanethiol provides efficient steric hindrance, providing a stable colloidal state and a smooth film on the substrate.

ZnO for Electron Transport Material

Mainly two different types of ZnO materials are used to provide ETL.

1) **Sol-gel synthesized ZnO thin film**

Sol-gel synthesized ZnO is used as an ETL. Sol-gel method is widely used chemical synthesis of metal oxide thin films. The synthesis includes the intermediate step of a colloidal solution (sol) and semi-solid (gel) states, and its chemical reactions based on the transformation of molecular precursors into metal oxide nanoparticles via hydrolysis and condensation processes. For ZnO synthesis, zinc acetate ($Zn(CH_3COO)_2 \cdot 2H_2O$) is a precursor material. The chemical process is described by[33]

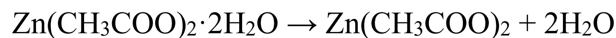

$$Zn(CH_3COO)_2 \cdot 2H_2O \rightarrow Zn(CH_3COO)_2 + 2H_2O$$

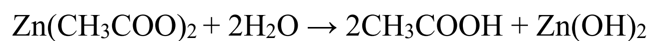

$$Zn(CH_3COO)_2 + 2H_2O \rightarrow 2CH_3COOH + Zn(OH)_2$$

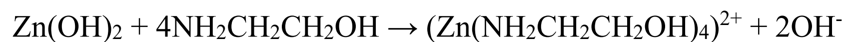

$$Zn(OH)_2 + 4NH_2CH_2CH_2OH \rightarrow (Zn(NH_2CH_2CH_2OH)_4)^{2+} + 2OH^-$$

$$Zn(OH)_2 + 2OH^- \rightarrow (Zn(OH)_4)^{2-}$$

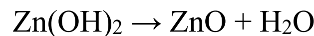

$$Zn(OH)_2 \rightarrow ZnO + H_2O$$

Zinc acetate ($Zn(CH_3COO)_2 \cdot 2H_2O$) undergoes hydrolysis to form zinc acetate dihydrates ($Zn(CH_3COO)_2$), and be stabilized in a sol-state by ethanolamine ($4NH_2CH_2CH_2OH$) in ethanol solution. Solution phase $Zn(OH)_2$ is thermally decomposed at low temperature (150 °C) into ZnO. In the final process, H_2O is vaporized by heating. The hydrolysis is strongly sensitive to humidity. For example, low humidity slows down the hydrolysis rate. This provides an

insufficient hydrolysis reaction, causing large trap density and oxygen deficiency. On the other hand, high humidity condition increases the hydrolysis rate, which does not provide enough time for packing nanoparticles. This causes a high surface roughness and an uncontrollable thickness. The humidity control during sol-gel process is, therefore, critical for the ZnO and QLED performance in the experiments. The effect of the humidity level during the fabrication process on the QLED performance is shown in Figure 3.2. Each red dot indicates current efficiencies at 20 mA cm^{-2} current flow of QLEDs fabricated in the different humidity. The film depositions of the QD EML and the HTL are performed inside the glove box where the moisture and oxygen levels are kept consistent and low. The humidity value in this plot indicates the lab humidity during sol-gel synthesis for ZnO. Therefore, a major factor of the scattered performances is the sol-gel synthesis process in the different humidity. Accordingly, it is required to control the humidity under 30 % during the sol-gel synthesis. Since the sol-gel process does not require high temperature process, it is used for the modification via polymeric materials that is not compatible with the high temperature processing.

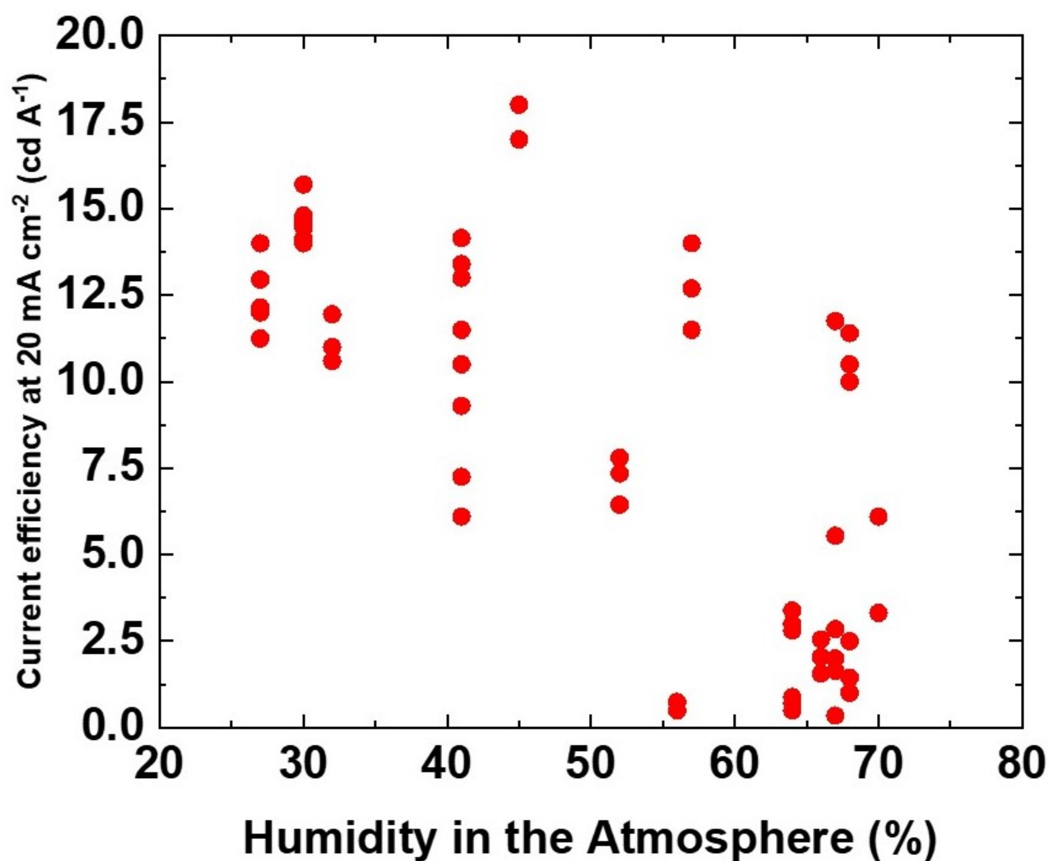

Figure 3.2 The current efficiency of QLED at 20 mA cm^{-2}. Each device is fabricated in different humidity conditions.

2) ZnO Nanoparticles Dispersed Solution

Commercialized ZnO NP product (SkySpring Nanomaterials, Inc.) is another option for providing ZnO ETL in the experiments. The product provides 8 ~ 12 nm particle size of ZnO dispersed in an ethanol solvent. The ZnO NP solution can proceed to solution-coating

without complex synthesis process that may be vulnerable to atmospheric conditions. The solution-coating of ZnO NP is done in the glove box where the O_2 and H_2O levels are kept low (< 0.1 ppm). This ZnO NP requires a post-annealing process above 200 °C. Based on the optimization sequence, it was figured out that the post-annealing process largely impact on the current efficiency and driving voltage as can be shown in the Figure 3.3. This is well agreement results with the previous reports suggesting thermal annealing effect on electrical property of the ZnO NP[137]. The ZnO NP is used for plasma treatment and wet treatment with halides that has endurability to the thermal decomposition.

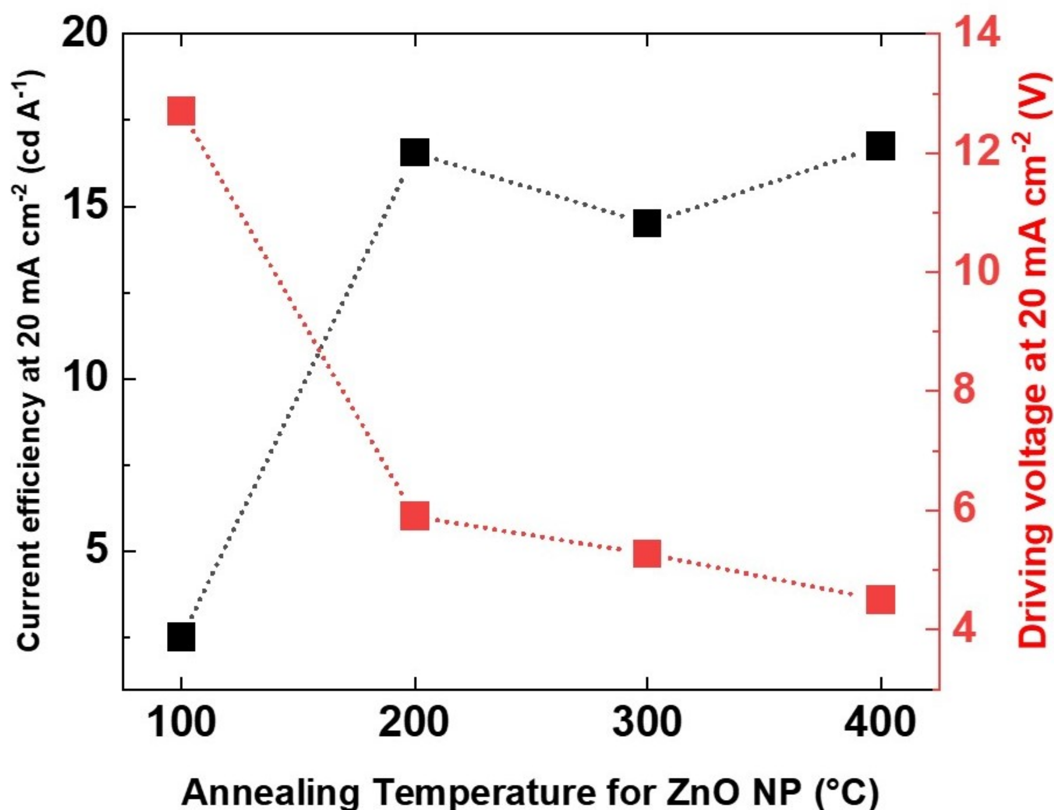

Figure 3.3 Current density and driving voltage dependence on post-annealing temperature of ZnO NP solution coating.

CBP/MoO_3 for HTL/HIL

For hole transport and injection, a CBP/MoO_3/Al structure is used in the inverted QLED. Carbazole-based materials, e.g., CBP and TCTA, have good hole transporting properties and a deep HOMO level[138], which makes them a popular choice for QLEDs. The deep HOMO energy level of CBP allows a relatively low energy barrier with the QDs compared to other HTLs. MoO_3 is directly deposited onto CBP to enhance hole injection into CBP. MoO_3 can induce a strong electric dipole, improving hole injection from Al into CBP.

The CBP/MoO_3/Al structure provides consistent hole injection into the QD EML throughout repeated fabrications, thereby providing consistent device performance.

Solution Deposition Processes for ETL and QD EML

Sol-gel ZnO solution is prepared by mixing 0.197 mg of zinc acetate and 54 μL of ethanolamine in 6 mL of ethanol by using magnetic stirring bar on a 50 °C hotplate for 40 minutes. Sol-gel synthesized ZnO is then deposited by solution-coating process in a clean room at room temperature. The sol-gel ZnO solution is spin-coated at 1,000 rpm and followed by baking on a 120 °C hotplate for 30 minutes. On the other hand, solution-coating for the ZnO NP is performed in a N_2-filled glove box. The concentration of ZnO NP solution is diluted to 30 mg mL^{-1} in an ethanol solvent. The ZnO NP solution is then spin-coated by 3,000 rpm, followed by 30 min annealing at 400 °C. The modifications are performed during ZnO solution preparation or after ZnO ETL deposition, avoiding any impact on the following EML and HTL. CdSe/ZnS QDs (12.5 mg mL^{-1}) dispersed in octane (Sigma-Aldrich) are spin-coated on the ZnO ETL at 3,000 rpm followed by post-baking on a 50 °C hotplate for 30 minutes. Spin-coating and subsequent baking steps for the QD EML are also performed in a N_2-filled glove box.

Thermal Evaporation for HTL/HIL/Al anode

Angstrom EvoVac Deposition System is used to deposit HTL, HIL, and Al anode. The system includes a nitrogen-filled glove box, a thermal deposition chamber, and a cryogenic pump with automation system combining with a software to control vacuum, deposition rate, materials, and thickness sensors. The chamber is opened by the nitrogen injection. A picture of the chamber inside is shown in Figure 3.4 (a) and (b). A substrate with devices is loaded inside the chamber with proper direction matched with a shadow mask that is installed just below a sample holder. The deposition rate and thickness are measured by a calibrated QCM sensor. The materials are installed inside the chamber using either aluminum oxide crucible, tantalum box boat with perforated holes top, or graphite-coated boat. Each material boat is

covered by shutters. The shutter is automatically opened once the deposition process initiates by the software in the computer. In the experiments, 50 nm of CBP (the source provided by Angstrom Engineering), 5 nm of MoO_3 (Angstrom Engineering) and 100 nm of Al (Angstrom Engineering) are sequentially deposited for HTL, HIL, and an anode electrode, respectively, under 10^{-6} mTorr vacuum condition controlled by the cryogenic pump.

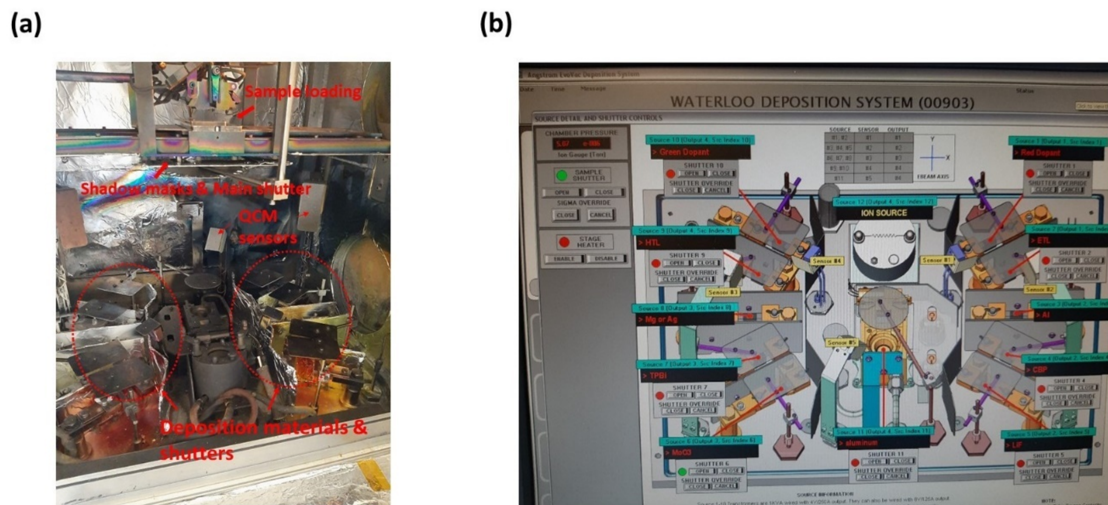

Figure 3.4 Pictures of (a) deposition chamber inside, (b) software screen that controls source/sample shutters.

3.2.2 Experimental Characterization

In this section, characterization tools used in this project and the purposes are introduced with a brief explanation of the techniques.

Nitrogen-filled test box

During the measurements, a sample is loaded in a home-built test box with N_2 gas flowing inside. Pictures of the test box are shown in Figure 3.5. The test box is made to keep a sample inert during the measurement in order to minimize the effects from atmosphere or any undesirable factors. The test box consists of 14 pins that make electrical contact with each

device when a switch is turned on, as well as a gas inlet for filling with N_2. A position of the pins is located to fit with the pre-patterned ITO on the glass substrate. The test box is then connected with a power source and a semiconductor analyzer by using a BNC cable for electrical connection.

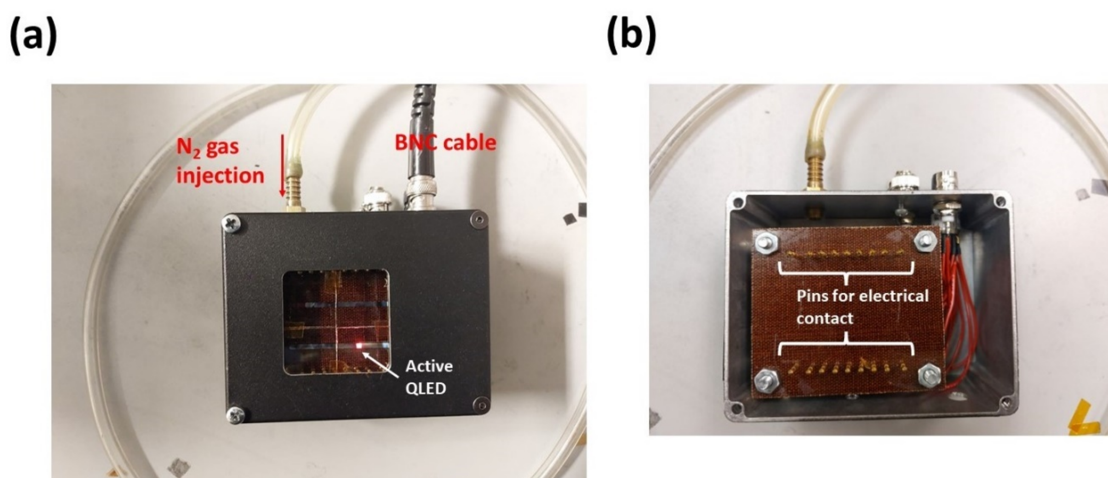

Figure 3.5 (a) A picture of N_2-filled test box used in this work and (b) inside of the box where the device substrate is placed.

Current density-voltage-luminance (J-V-L) measurement

The relationship between J, V, and L is a representative characteristic of EL of QLEDs. The device sample loaded in the test box is connected to an Agilent 4155C semiconductor parameter analyzer (Figure 3.6 (a)). A silicon photodiode (Figure 3.6 (b)) is connected to the analyzer to measure EL intensity. The software (ICS Interactive Characterization Software, Metrics Technology, Inc.) controls measurement parameters, voltage ranges, and sweeping modes. The silicon photodiode detects photocurrent from the device during the voltage sweep. The luminance value is first manually measured by using Minolta CS-100s under 20 mA cm^{-2} current flow. The measured luminance is then used to convert the photocurrent value obtained

by the photodiode into the luminance value. The J-V-L characteristics are used to investigate charge transport across the device, and extract current efficiencies and EQEs of QLEDs.

(a)

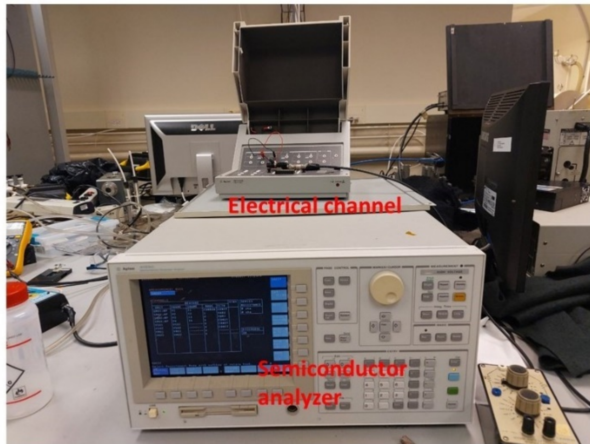

(b)

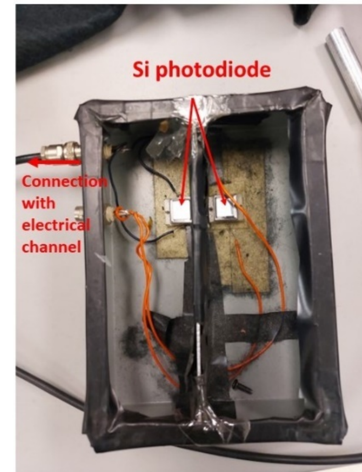

Figure 3.6 A picture of (a) Agilent 4155C semiconductor parameter analyzer and Agilent 15462A electrical channel and (b) silicon photodiodes connected to the electrical channel.

Emission spectra measurement

The photon energy is a result of radiative recombination of excited electrons by either photoexcitation (PL) or electrical pump (EL). The PL and EL spectra are measured to investigate the luminescence characteristics of materials and QLEDs. The emission spectra contain all the emissive photons of a sample. It can be used to evaluate color purity, recombination center, and luminescence quenching. In the experiments, the EL spectra of devices installed in the test box are measured under current flow using an Ocean Optics QE65000 spectrometer. The PL spectra are measured by the same spectrometer with a Newport 67005 200W HgXe arc lamp and monochromator as an excitation source. The samples are installed on a sample stage while kept in the N_2-filled test box. The lamp and the sample stage

are aligned on an optical table for guiding the excitation light to the sample surface. The experimental setup is shown in Figure 3.7.

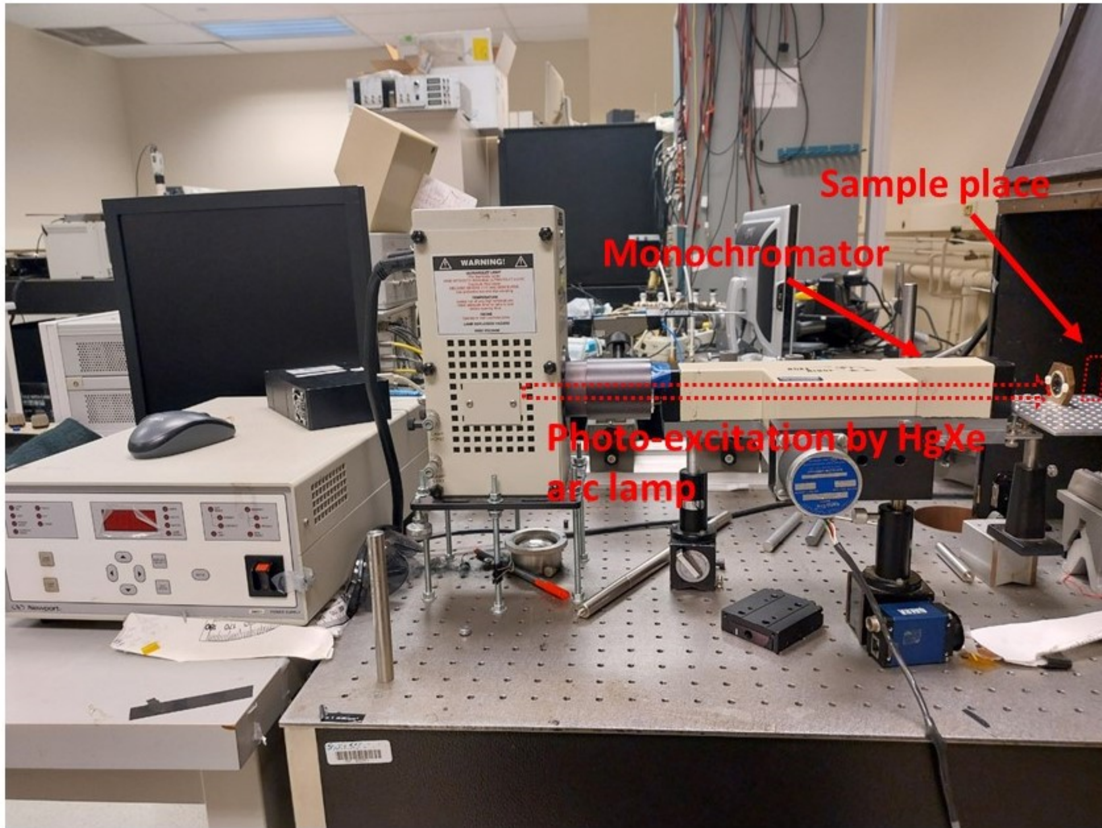

Figure 3.7 A picture of an experimental setup on optics table for EL/PL measurements.

Device lifetime measurement

The device luminance *vs.* time characteristics measured in this work are recorded using a M6000 PLUS OLED lifetime test system. The equipment consists of 8 test boxes as shown in Figure 3.8 (a). The test box has pins for electrical contacts designed for the substrate dimension described in Figure 3.1 (a). The measurement modes include constant current

flowing, constant voltage applying, pulsed current/voltage, etc. The software automatically record time, relative luminance, current density, and driving voltage.

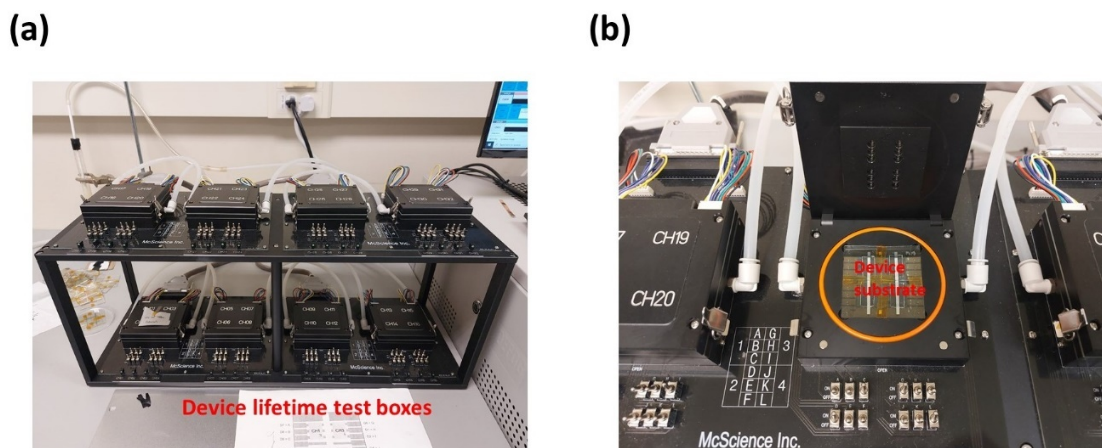

Figure 3.8 A Picture of M6000PLUS OLED lifetime tester: (a) device lifetime test boxes, and (b) the test box inside.

Time-resolved photoluminescence measurement (TRPL)

TRPL can be used to investigate transient PL characteristic of the materials within the nanosecond range. It detects PL decay in the material. The PL decay provides information on the transition of electronic states, including both radiative and non-radiative recombination, luminescence quenching, and exciton lifetime. In the experimental setup, pulsed laser source (375 nm wavelength) is used to produce electronic transition in a sample, followed by deactivation of the excited states. The decay of PL is measured by time correlated single photon counting (TCSPC). It measures the time difference between the excitation of the sample and the released photon energy. This cycle is repeated multiple times, providing the PL intensity decay profile. The number of photons (intensity) exponentially decreases by the deactivation of the molecules. The raw data is required to be analyzed numerically by extracting parameters.

In general case, the intensity (*I(t)*) decay has a form of single- or multi-exponential decay, expressed by

$$I(t) = \sum_{i=1}^{n} A_i e^{-t/\tau_i} \tag{3.1}$$

with A_i indicates weighing constants and τ_i indicates the characteristic lifetimes. The τ_i may be the most important because it expresses the recombination rate and can be used to determine the factor for the specific recombination.

Capacitance-voltage (C-V) measurement

Based on a classical electrostatic correlation of capacitance and voltage with charges

$$Q = C \cdot V \tag{3.2}$$

The capacitance measurement is used to investigate the charge accumulation and annihilation across the QLED. The QLED structure consists of CTLs and QD EML placed between two electrodes, which can be considered as a typical parallel capacitor. In QLED operation, electron and hole are transported through the CTLs and eventually injected into the QD EML. During the process, energy barriers at the CTL/QD EML interfaces induce charge accumulation, which reduces effective thickness of the capacitor, increasing the capacitance value. Charge carrier recombination in the QD EML or other layers reduces the number of charges, thereby sudden decreasing in the capacitance value.

Delayed Electroluminescence (delayed EL) Measurement

Delayed EL measurement is used to estimate charge distribution by capturing parasitic EL after termination of an electrical excitation[139]. It can be used to investigate the location of charge-trapping and slow EL components due to energy transfer and exciton diffusion. The delayed EL signal is due to (1) late recombination from charges that are de-trapped from termination of bias, and (2) slow emission stimulated by an energy transfer by triplet-triplet annihilation (TTA) process in phosphorescence materials. The measurement requires a

specialized setup, schematically shown in Figure 3.9. The setup mainly consists of bias pulse generator (Stanford Research Systems, DG535 digital pulse generator), optical fiber, and an optical chopper (ThorLabs MC1000A). The optical fiber is capturing both prompt EL signals and delayed EL signals. A digital phosphor oscilloscope (Tectronix, TDS5054) records the measured EL signals. During the measurement, the QLED is driven by a 500 µs forward bias square pulse of magnitude equivalent to the driving voltage required to achieve a current density of 20 mA cm^{-2} and allow the prompt EL to reach steady state. Modulating the forward bias voltage to obtain the same current density ensures that the number of charges injected during the forward bias pulse is similar in all devices. The chopper is open to allow the optical fiber to capture the delayed EL signals. Reverse bias pulse can be applied during the delayed EL capturing in order to further understand the charge distribution.

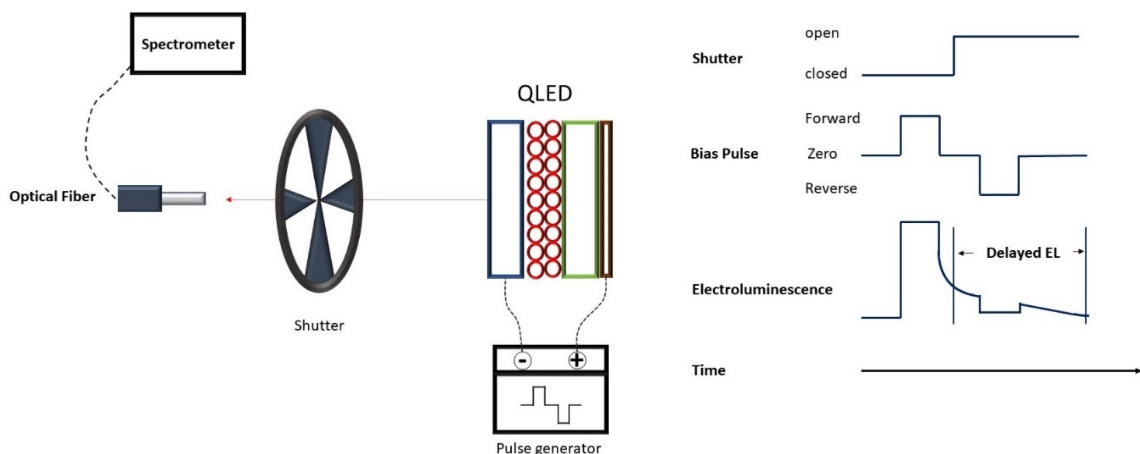

Figure 3.9 A schematic image of delayed EL experimental setup.

Time-of-Flight Secondary Ion Mass Spectrometry (TOF-SIMS)

TOF-SIMS is a technique to measure the composition of a species. It uses pulsed ion beam to destroy from the outermost surface of a layer and detect the secondary ions detached

from the surface. It, therefore, investigates the distribution of chemical composition across the entire film depth.

X-ray Photoelectron Spectroscopy (XPS)

XPS is to detect a chemical composition and chemical states on the surface by using photoelectric effect. The energy of X-ray produces core-level electron emission in chemical bonds in the material and the electron binding energy is measured by kinetic energy of ejected electron. The XPS is performed to characterize the valence state of the material and estimate chemical composition by characterization of binding energy of each chemical species.

Atomic Force Microscopy (AFM)

AFM is a scanning probe microscopy that can directly measure a surface topography. It is commonly used to characterize the surface roughness of deposited films, which is a critical factor affecting device performance. A rough film surface can create partially short channels for electrons, which can lead to non-uniform emission and increased electrical stress on the short channel region. This can result in the formation of dark spots and device failure due to shorting and Joule heating. Therefore, AFM is a useful tool for evaluating surface characteristics and estimating the film structure required for stable QLEDs. There are mainly two different modes for AFM measurements: contact mode and non-contact mode. The contact mode involves the direct contact of the probe with the surface, which can result in surface damage during the measurement. On the other hand, non-contact mode uses a probe that oscillates close to the surface, and the interaction between the tip and the sample is measured. This mode is widely used to measure soft materials, such as organic materials, and thin films because of minimal surface damage during the measurement. In this work, the non-contact mode AFM is used to investigate surface characteristics.

Chapter 4 Approaches to the ZnO Modification for QLED Stability Improvement

This work has been published in DS Chung et al., Nanoscale Advances, 3 (20), 5900-5907, 2021, DS Chung et al., Nano-Micro Letters, 14 (1), 212, 2022, and DS Chung et al., Advanced Optical Materials, 2300686, 2023. It has been reproduced in part with permission from the publisher.

In this Chapter, two approaches for ZnO modification are discussed: (i) adding polymer additives to the ZnO and (ii) using halogen treatment on ZnO via plasma and wet processes. In Section 4.1, the ZnO:PEI nanocomposite is introduced as a new form of ETL. The EL characteristics of the QLED with the ZnO:PEI are then discussed and compared with those of both the conventional ZnO and ZnO/PEI double layer. In the Section 4.2, the halogen treatment on ZnO is introduced and their effects on the EL characteristics of the QLED. The sub-section 4.2.1 discusses the modification of ZnO via the CF_4 plasma treatment whereas the sub-section 4.2.2 focuses on the chemical doping of I_2 and $FeCl_3$ into ZnO.

4.1 ZnO:PEI Nanocomposite Thin Films

4.1.1 Blending sol-gel ZnO and PEI for New Form of ETL

Polymers containing aliphatic amine groups, such as polyethylenimine (PEI) and its ethoxylated derivative (PEIE), are often used for the purpose of enhancing QLED efficiency[107,117,118]. While the influence of PEI interfacial layers on QLED efficiency has been well studied, their impact on stability has received much less attention, with only one recent study suggesting that they had a limited effect[72]. They also need to be used in the form of ultrathin (< 10nm), pin-hole free layers which is challenging for solution coating. Instead, mixing the PEI into the ZnO in the form of a ZnO:PEI blended ETL instead of a separate layer has therefore been recently proposed[140]. In the only report applying a ZnO:PEI(E) ETL to QLEDs, Shi et al. showed that using a ZnO:PEIE blended ETL can improve the efficiency of

inverted blue QLEDs but its effect on stability was not addressed[141]. In this section, the effect of using ZnO:PEI blended ETL compared to a neat ZnO and a bilayer ZnO/PEI ETL structure on QLED performance is investigated.

4.1.2 Results and Discussion

Device fabrication

ZnO solution is prepared by the sol-gel synthesis as described in the sub-section 3.2.1. PEI solution is prepared by stirring branched-PEI (Sigma-Aldrich) in ethanol or 1-propanol (Sigma-Aldrich) at 700 rpm overnight in N_2 filled glove box. 1 mL of PEI solutions in ethanol with different concentrations are then mixed with 1 mL of ZnO solution at 700 rpm for 1 hour to make solutions of the different ZnO:PEI ratios. ZnO solutions are spin coated at 1000 rpm on the cleaned ITO substrates followed by 150°C baking on a hotplate for 30 minutes. ZnO:PEI blended solution is deposited by solution coating at 2,000 rpm followed by 120°C baking on a hotplate for 30 minutes. For ZnO/PEI bilayer ETL, 0.5 mg/mL of PEI dissolved in 1-propanol is spin coated at 5000 rpm followed by 120°C baking on a hotplate for 20 minutes on top of a ZnO film. 4 mg/mL CdSe/ZnS QDs dispersed in octane is deposited on ETL at 500 rpm and baked on a 50°C hotplate for 30 minutes. CBP, MoO_3, and Al are then deposited by thermal evaporator (Angstrom Engineering) under 5×10^{-6} Torr for HTL, hole injection layer (HIL) and anode. Film thicknesses are measured using a Dektak-150 profilometer.

First, the effect of using a ZnO:PEI blended ETL *vs.* a ZnO/PEI bilayer ETL *vs.* a ZnO-only ETL on the EL characteristics of the QLEDs is compared. For this purpose, four groups of QLEDs of the general structure are fabricated and tested : ITO/ETL (~32nm) /QD (30 nm)/CBP (50 nm)/MoO_3 (5 nm)/Al, with the ETL made of ZnO:PEI with 0.1% or 0.3% PEI by weight, (denoted as ZnO:ETL with different concentration 0.1 wt% and 0.3 wt% as ZnO:$PEI_{0.1}$ and ZnO:$PEI_{0.3}$, respectively.) ZnO/PEI or only ZnO, the last one to serve as control. The thickness of the ETL in all devices was ~32 (±3nm), which included the additional thickness of the neat PEI layer (~8 nm) in case of the bilayer ETL. Figure 4.1 (a) depicts the general QLED structure, whereas Figures 4.1 (b-d) present the JVL, EQE and EL spectra of

the devices, respectively. As can be seen from the J-V characteristics, the devices with the ZnO/PEI and ZnO:PEI ETLs all have a higher threshold voltage (V_{th}) and a lower current density at any given voltage in comparison to the control device. One can also see that increasing the PEI concentration from 0.1 wt% to 0.3 wt% in the ZnO:PEI ETL reduces the current at any given voltage. The higher V_{th} and lower current density suggest that the PEI makes electron injection and transport more difficult, an effect that can be attributed to its low conductivity. An examination of the EQE *vs.* current density characteristics in Figure 4.1 (c) shows that using the PEI brings about a significant increase in EQE, increasing the maximum value from 7.7% (in case of the ZnO control device) to 11.2%, 11.0% and 12.1% for the ZnO/PEI, ZnO:$PEI_{0.1}$, and ZnO:$PEI_{0.3}$ devices, respectively. With the J-V characteristics in perspective, the EQE enhancement can be attributed, at least in part, to the role of the PEI in reducing the charge imbalance in the QD EML produced by the asymmetric carrier injection barriers. The passivation of ZnO surface defects by the PEI may also be contributing to this efficiency enhancement. While this passivation effect has only been studied in devices with ZnO/PEI in the past, we may expect a similar effect in case of the ZnO:PEI blends. The EL spectra (Figure 4.1 (d)) show a single emission band with peak at wavelength 632 nm, indicating that the majority of radiative recombination happens in the QD EML in all devices.

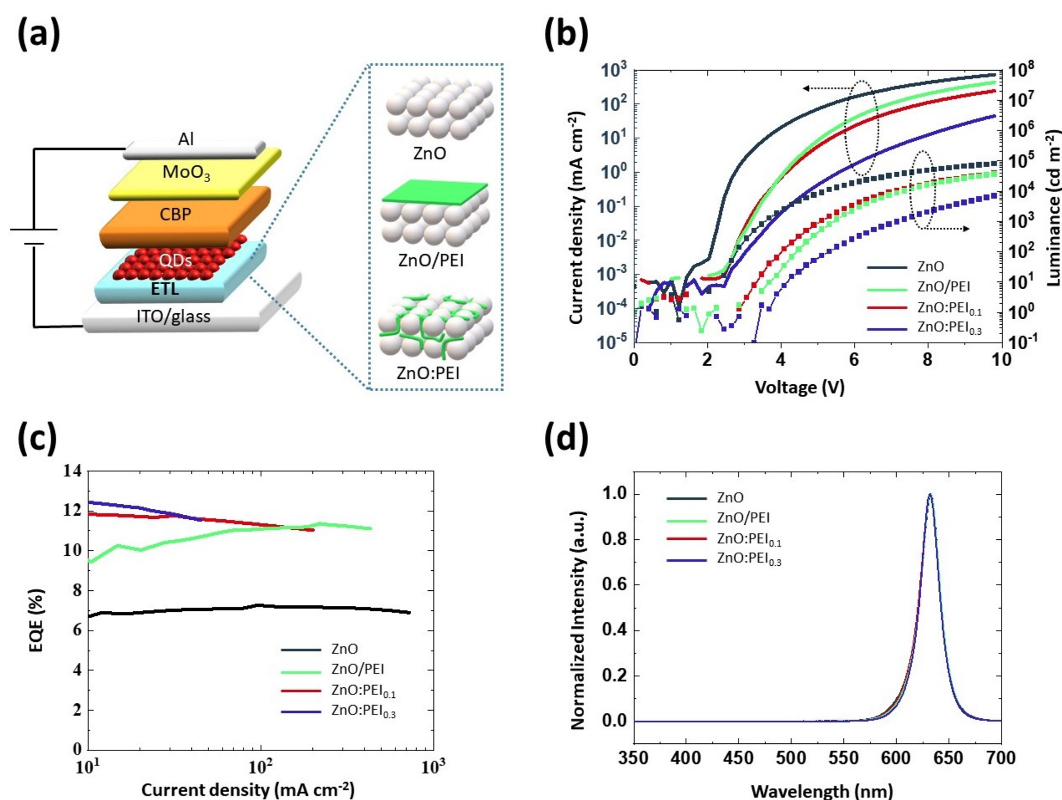

Figure 4.1 (a) Schematic diagram showing the general structure of the QLEDs and the different ETLs investigated in this work. (b) J-V-L characteristics, (c) EQE *vs.* current density, and (d) EL spectra of the QLEDs.

Next, the EL stability of the devices under constant current driving at 20 mA cm^{-2} is tested. Figure 4.2 (a) and (b) show the normalized luminance (relative to the initial luminance, L_0) and changes in the driving voltage (driving voltage at time, t, minus the initial driving voltage) *vs.* time plots of the devices, respectively. The LT50 of the ZnO ETL and ZnO/PEI devices is 46 hours and 62 hours, respectively (from an L_0 of 2,500 and 3,030 cd m^{-2}, respectively). In contrast, the LT50 of the ZnO:PEI devices is markedly longer, amounting to 140 hours in case of the ZnO:$PEI_{0.1}$ device and 292 hours in case of the ZnO:$PEI_{0.3}$ device

(from an L_0 of 3,000 and 3,250 cd m^{-2}, respectively). Using the lifetime scaling rule ($L_0^n LT50 = constant$) and the widely used value of 1.8 for the scaling coefficient, these values correspond to LT50 values of 15,100 hours, 28,773 hours, 65,630 hours and 153,735 hours, respectively for an L_0 of 100 cd m^{-2}. Introducing the PEI into the ZnO layer, instead of having it in a separate layer, leads to a significant enhancement in the EL stability of QLEDs, leading to ~10 times longer LT50 at L_0 of 100 cd m^{-2}. Table S4.1 summarizes the LT50 values of the devices and their EQEs. There is a distinct difference between the trends of the control device and the PEI containing devices in the driving voltage trends of Figure 4.2 (b), with the latter all experiencing an initial decrease in the driving voltage initially before beginning to rise over time. In general, an increase in driving voltage during electrical driving can be attributed to the formation of space charges within the device layers that create internal electric fields of opposite direction to the field produced by the external bias which require an increase of the external bias to offset their effect and maintain the same current flow. As the difficulty of injecting holes into the QD EML arising from the large energy difference between the HOMO of the HTL and the valence band of the QD is a bottleneck for current flow in QLEDs in general, one can expect the increase in voltage to be associated with hole accumulation and the build-up of hole space charges in the HTL near the QDs/HTL interface. The fact that the presence of the PEI alters the trend of the driving voltage initially therefore suggests that it may be slowing down the formation of these hole space charges. One also notes the different curvature (i.e., trajectory) of the driving voltage trends of the PEI devices where the increase in voltage seems to accelerate in the longer term. Surprisingly, this effect seems to be most significant in case of the ZnO:$PEI_{0.3}$ which exhibits the fastest increase in driving voltage despite it having the highest EL stability. That this increase in driving voltage does not seem to negatively affect device efficiency (as inferred from the stable EL) suggests that it may be arising from space charges that are formed far away from the QD EML.

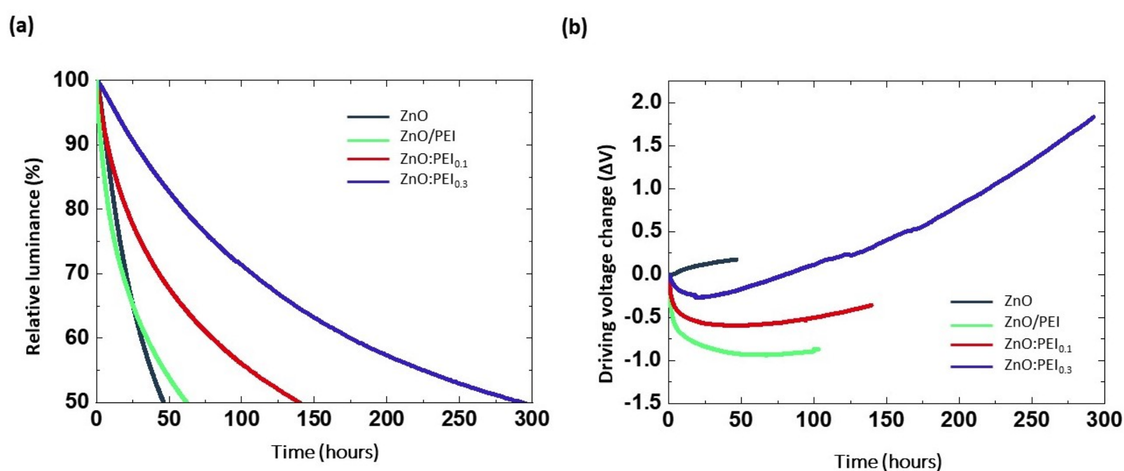

Figure 4.2 (a) Relative luminance and (b) changes in driving voltage *vs.* time trends of the QLEDs with the different ETLs under 20 mA cm^{-2} constant current driving conditions.

4.2 Halogen-incorporating into ZnO Nanoparticles

In this work we investigate the influence of halogen treatment on the ZnO NP ETLs on QLED performance. First, fluorine is incorporated into ZnO NPs. While the use of F for passivating ZnO oxygen vacancies has been pursued in thin film transistors[142,143] and photovoltaic devices[144,145], it has not yet been investigated for QLEDs. Here we demonstrate the first F-incorporation into ZnO for ETL of QLED and find that incorporating F into the ZnO ETLs of QLEDs significantly improves their electroluminescence stability. Via the use of carbon tetrafluoride (CF_4) plasma treated ZnO (FZnO) NP ETLs, we successfully fabricated highly stable QLEDs. Second, we investigate the effect of adding other halide dopants, i.e., I_2 and $FeCl_3$, to ZnO ETL on QLED stability. By incorporating I_2 and $FeCl_3$ as halide dopants into ZnO ETL, the LT50 of red QLEDs increases compared to neat ZnO ETL.

4.2.1 CF_4 Plasma Treatment on ZnO Nanoparticles

Doping by F has been found to modify ZnO properties in the past[146,147]. The ionic radius of F is comparable to that of oxygen, making it possible to neutralize oxygen vacancies without causing significant lattice distortions[142,148,149]. ZnO NP films are subjected to a F plasma using a parallel plate reactor with a CF_4 source gas. In a conventional parallel plate reactor, the sample to be treated is typically placed on a stage on one of the two electrodes. The high potential gradients near the electrodes however lead to the acceleration of charged plasma species and their collision with the sample surface at high kinetic energies resulting in bond cleavage and damage to the sample[150]. Therefore, to avoid this effect, the samples are placed in the middle of the plasma chamber where the potential gradients are smaller and ion bombardment effects are minimal, as schematically depicted in Figure 4.3 (a). Chemical modification of the ZnO NPs by the CF_4 plasma treatment is verified by X-ray photoelectron spectroscopy (XPS). Figure 4.3 (b) depicts the XPS spectra of F 1s core level electrons for FZnO and non-exposed ZnO films. To remove any surface contamination, Ar sputtering for 30 seconds is conducted on the film surface before the XPS measurement. A distinguishable F 1s spectrum emerges in the plasma treated film (i.e., FZnO) that is not observed in the untreated ZnO film. The emergent F 1s spectral peak can be deconvoluted into two bands with maxima at 685.9 eV and 687.6 eV[149]. The 685.9 eV band can be ascribed to Zn-F bonding whereas the 687.6 eV band may be attributed to elemental fluorine or to F-C species[151] (with C present in the surface ligands of the ZnO NPs, for example). Fluorine, zinc and oxygen ion depth profiles in ZnO and FZnO films are further investigated through time-of-flight secondary ion mass spectroscopy (TOF-SIMS) in Figure 4.3 (c). The peak intensities of the detectable species in Figure 4.3 (c) are normalized to the intensity of the indium oxide ions. Clearly, negative fluorine ion species are detected throughout the entire FZnO film thickness but not in the ZnO film. This observation confirms that the plasma treatment leads to F incorporation across the entire bulk and is not limited to the film surface. Figure 4.3 (d) and (e) show XPS band spectra of O 1s core level electrons in ZnO and FZnO films, respectively, again collected after a 30s

Ar sputtering to remove any surface contaminants. The highest (O_i) and lowest (O_{iii}) energy bands correspond to hydroxyl groups and ionized oxygen ions, respectively, whereas the middle one (O_{ii}) can be attributed to electronic states associated with oxygen vacancies in the lattice[148]. Quite notably, the relative intensity of the O_{ii} band decreases in case of FZnO film. This suggests that the fluorine atoms passivate the oxygen vacancies in the ZnO lattice, possibly by bonding with unbonded Zn^{2+} states. Steady state PL spectra under 330 nm UV excitation for the ZnO and FZnO films were also collected and are shown in Figure 4.3 (f). There are two distinguishable bands at 2.3 eV and 3.1 eV, which can be ascribed to emission from Shockley-Read-Hall (SRH) recombination at sub-band gap states[69,152], and originating from oxygen vacancies and other defects such as zinc interstitials which lead to different states in ZnO films, respectively[153-155]. The PL intensity of both bands becomes lower in FZnO, an effect similar to that observed in Mg-doped ZnO[156], suggesting that the presence of the fluorine passivates the sub-band gap states and reduces radiative electron-hole recombination.

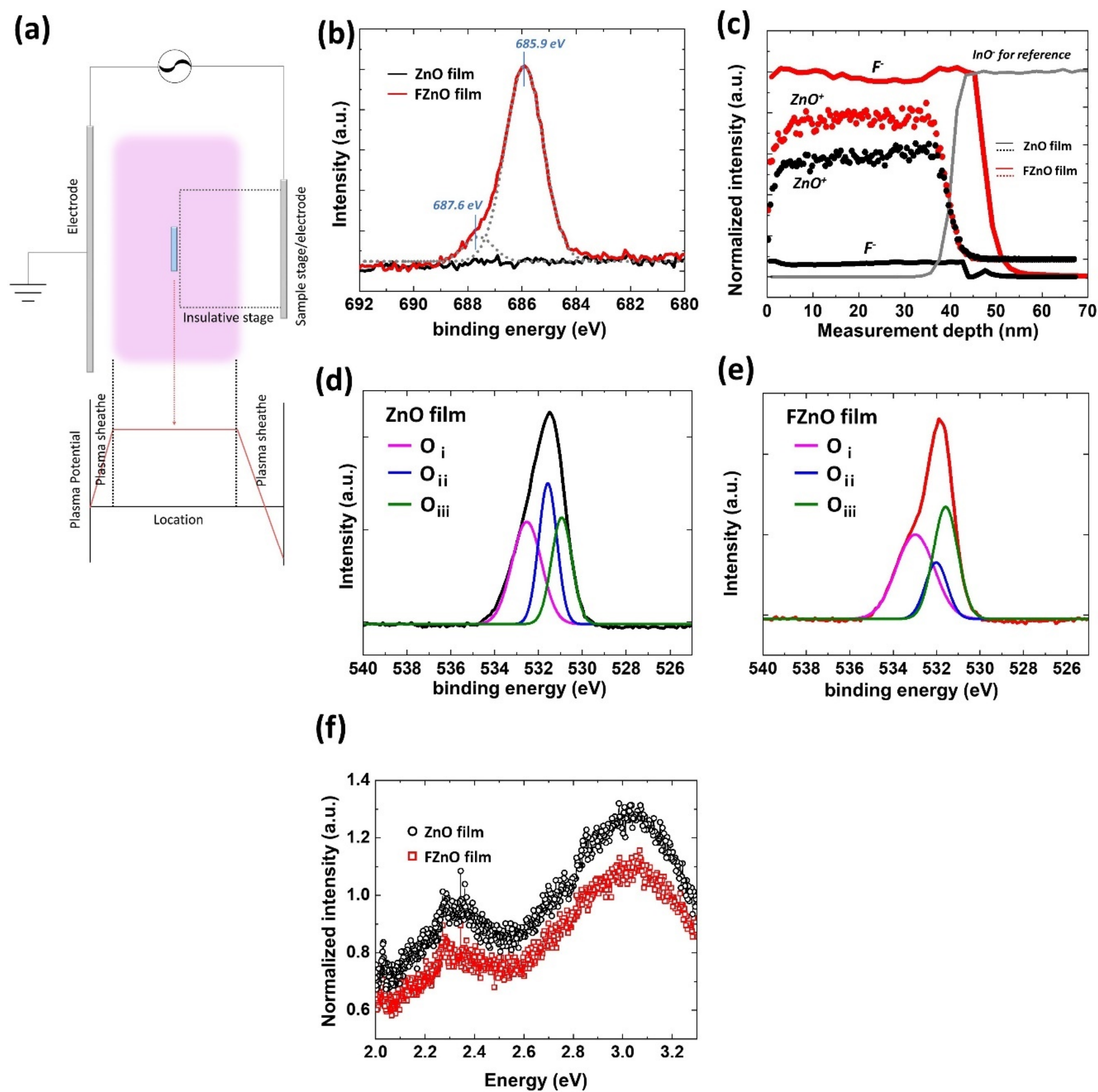

Figure 4.3 (a) Schematic diagram of the plasma treatment setup. (b) XPS spectra of F 1s core level electrons in ZnO and FZnO films and (c) F^- and ZnO^+. All intensity values of TOF-SIMS are normalized by intensity of InO^- signal. O 1s core level electrons in (d) ZnO film and (e) FZnO film. (f) Steady-state PL spectra under 330 nm UV excitation collected from the ZnO and FZnO films.

Seeing that the F incorporation may be passivating the sub band-gap states in the FZnO NP film, one can expect the use of FZnO as ETL in QLEDs may improve device performance. FZnO NP films are therefore incorporated as ETLs in inverted red QLEDs to investigate their effect on the electroluminescent (EL) characteristics. The structure of the QLEDs is schematically shown in Figure 4.4 (a), and consists of, in order: ITO/ETL (40 nm)/QD EML (30 nm)/ CBP (50 nm)/MoO_3 5 nm/Al. Two groups of QLEDs of this general structure but with different ETLs are fabricated: ZnO (control device, ZnO-QLED) and FZnO (CF_4 plasma treated, FZnO-QLED). The EL characteristics of the QLEDs are shown in Figure 4.4 (b-d). The shown characteristics represent typical values from among a set of 9 devices from each group fabricated on different days. The J-V-L characteristics in Figure 4.4 (b) show that the FZnO-QLEDs have similar threshold voltage (V_{th}) and turn-on voltage (V_{on}) to the ZnO-QLEDs. The current density at any given voltage is however lower indicating that electron transport is affected by the treatment. Another notable point is the reduction in current density below V_{th} in case of the FZnO-QLEDs. The sub-threshold current reduction can be explained in terms of the current flow mechanism in the low electric field regime, which for a junction-based diode structure, will be dominated by carrier recombination and described by[8,157]

$$J_{rec} = \frac{q \cdot n_i \cdot t_{scr}}{\tau_r} \tag{4.1}$$

where J_{rec} represents the recombination current density, and q, n_i, t_{scr}, and τ_r represent the elementary charge, intrinsic carrier density in the material, the width of space charge region in the junction, and recombination lifetime, respectively. Since the recombination process involves both band-to-band recombination ($\tau_{band\ to\ band}$) and SRH recombination (τ_{SRH}), τ_r will be given by[8,157]

$$\frac{1}{\tau_r} = \frac{1}{\tau_{band\ to\ band}} + \frac{1}{\tau_{SRH}} \tag{4.2}$$

where τ_{SRH} is given by[8,157]

$$\tau_{SRH} = \frac{1}{\alpha_{SRH} \cdot N_t} \tag{4.3}$$

with α_{SRH} and N_t representing the SRH recombination coefficient and trap density of states, respectively. The N_t of the QLEDs are further discussed and calculated in Appendix A. Since, based on the PL results, SRH recombination must be less in case of the FZnO-QLED, the lower current density at voltages below V_{th} can be ascribed to the lower trap density, in line with Würfel[157] et al. and Anderson et al[8]. The small difference between V_{th} and V_{on} indicates that carriers are efficiently injected for exciton formation and radiative recombination in the QD EML. EL spectra of the ZnO- and FZnO-QLEDs are shown in Figure 4.4 (c). Both devices exhibit strong QD emission at 630 nm without any discernable parasitic emission from the other layers. The EQE *vs.* current density characteristics of the QLEDs are shown in Figure 4.4 (d). The FZnO-QLED shows a maximum EQE of 15.3 %, a 15 % enhancement relative to the ZnO-QLED control device. Given that the PLQY of the QDs used in this work is 75%, and based on a 20 % out-coupling efficiency, the EQE of FZnO-QLEDs approaches the theoretical limit for a device with these QDs pointing to optimal charge balance and minimal exciton quenching conditions. With the decrease of sub-bandgap states in ZnO by the fluorine treatment, the efficiency improvement may be attributed at least in part to the passivation effect on ZnO trap states which can act as quenching centers.

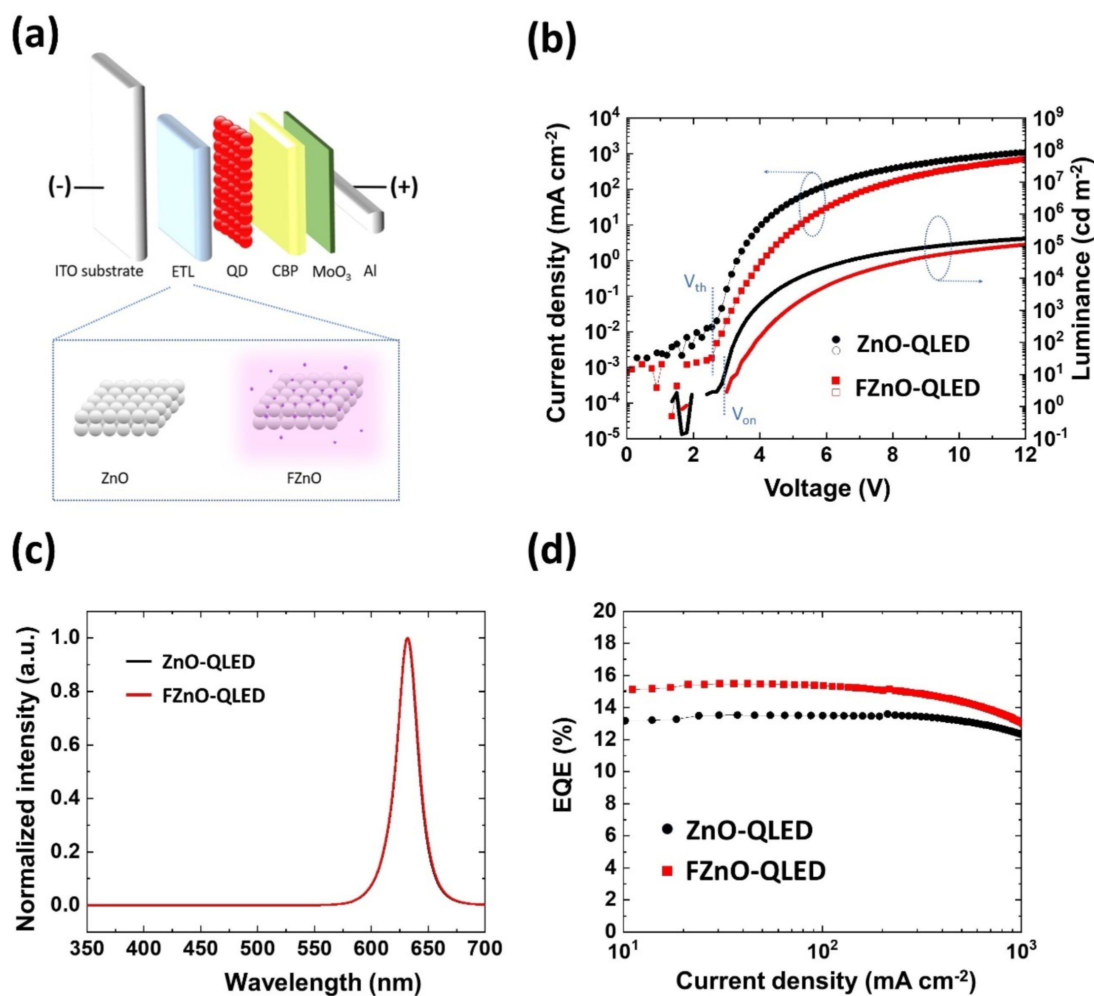

Figure 4.4 (a) Schematic diagram depicting the QLED structure. (b) J-V-L characteristics, (c) EL spectra, and (d) EQE *vs.* current density of QLEDs with ZnO *vs.* FZnO ETLs.

In addition to the improvement in EQE, the FZnO-QLED has been found to exhibit a significantly higher EL stability over the ZnO-QLED control. Luminance and driving voltage evolution versus time under constant current at 20 mA cm^{-2} are presented in Figure 4.5 (a) and (b), respectively. The initial luminance (L_0) is 3,320 cd m^{-2} and 3,910 cd m^{-2} for the ZnO- and FZnO-QLEDs, respectively. The LT50s of ZnO-QLED and FZnO-QLED are found to be 65

hours and 516 hours, respectively. In addition, both QLEDs show negligible difference in driving voltage evolution in Figure 4.5 (b). Different from some of the other reports for highly stable QLEDs via ETL modification where an exponential-like increase in driving voltage is sometimes observed[46], the FZnO-QLED shows a more linear trend which is more advantageous for long-term device operation. For a more accurate comparison between the lifetime of the devices, the LT50 equivalent values for L_0 of 100 cd m^{-2} is calculated using the lifetime scaling equation (1.20) ($L_0^n LT50 = constant$, where *n* is an accelerator coefficient). The value of *n* is calculated to be 1.9 and 2.3 for QLED with ZnO and FZnO, respectively, based on stability tests on different devices at various L_0 values as depicted in Figure 4.5 (c). The different lifetime scaling coefficient values suggest that there may be an underlying difference in the degradation mechanisms of ZnO- and FZnO-QLEDs. The projected LT50 for L_0 = 100 cd m^{-2} of the FZnO-QLED corresponds to 2,370,000 hours, a QLED lifetime improvement of 47 times over the 50,000 hours for the ZnO-QLED. To the best of our knowledge, this represents the longest LT50 for QLEDs utilizing conventional core/shell QDs obtained by ETL modification, suggesting that further stability enhancements may be possible if customized core/shell QDs or HTL materials are used with this ETL[23,51]. Table S4.2 summarizes data from previous reports of QLEDs with improved stability achieved via ETL modifications.

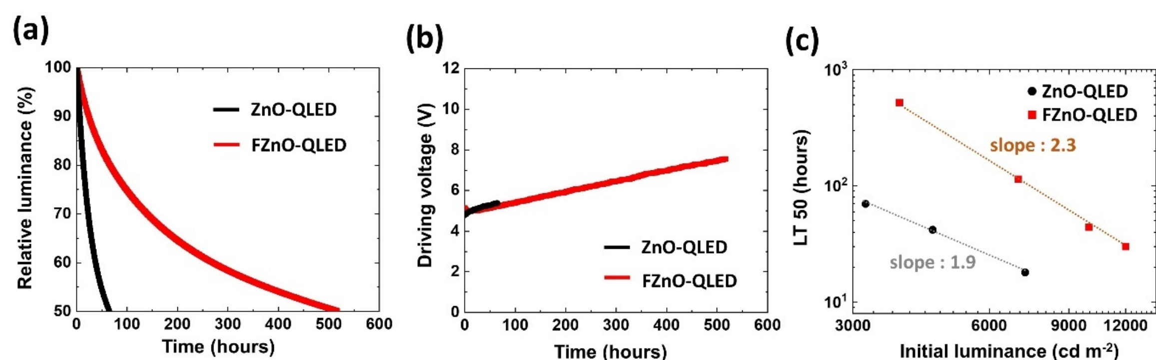

Figure 4.5 (a) Luminance decay *vs.* time and (b) driving voltage *vs.* time of ZnO- and FZnO-QLEDs operated at a constant current density of 20 mA cm^{-2}. (c) Measured LT50 values for different devices with operated at different L_0 values. The slopes correspond to the accelerator coefficients.

4.2.2 Introducing I_2 and $FeCl_3$ dopants into ZnO Nanoparticles

Here we investigate the effect of adding I_2 and $FeCl_3$ dopants to ZnO ETL on QLED stability[158]. Halides have been exploited as additives in various nanomaterials for modifying their electronic properties[159]. For example, the electrochemical potential of Au and TiO_2 nanoparticles can be effectively modified by metal-chloride additives[160,161]. Similarly, adding iodine to ZnO nanoparticles can form charge transfer complex species[162]. Therefore, one can expect incorporating halides into the ZnO ETL of QLEDs may influence device performance. To investigate this possibility, three groups of QLEDs utilizing ZnO as ETL, with or without halide dopants, of the following general structure are fabricated and tested: ITO/ETL (40 nm)/QDs (20 nm)/ CBP (50 nm)/MoO_3 (5 nm)/Al. In the first group, undoped ZnO is used whereas in the other two groups, the ZnO is doped with I_2 or $FeCl_3$. For the doped ZnO ETLs, 0.3 mg of I_2 or $FeCl_3$ are added into 1 mL of ZnO and the solutions are used for making the ETLs by spin coating. The ETLs are referred to by ZnO, I_2:ZnO, and $FeCl_3$:ZnO, respectively and the corresponding devices by ZnO-QLED, I_2:ZnO-QLED, and $FeCl_3$:ZnO-QLED, respectively. The general structure of the QLEDs is schematically depicted in Figure 4.6 (a) whereas their EL characteristics are presented in Figure 4.6 (b-d). The shown data represents

typical characteristics collected from a set of 14 devices from each group fabricated on different days. As can be seen from Figure 4.6 (b), the J-V-L characteristics show very similar threshold (V_{th}) and turn on (V_{on}) voltages for all QLEDs. This suggests that charge injection barriers are hardly changed by the use of dopants. In contrast, the currents at high voltages show some differences suggesting that the dopants may be affecting charge transport properties across the ETL, especially for I_2:ZnO-QLEDs where the current density at any given voltage is non-negligibly lower in comparison to their ZnO counterparts. From Figure 4.6 (c) one can see that the dopants had some but limited effect on current efficiency, with all devices exhibiting very similar current efficiency at 20 mA cm^{-2}, the current used for the lifetime measurements and later experiments in this work. From the EL spectra in Figure 4.6 (d), one can see that all devices have a strong emission at 630 nm without any discernable parasitic emission from the other layers. Given that the same QD EML and HTL are used, the similar current efficiency at 20 mA cm^{-2} implies comparable exciton formation and radiative recombination efficiencies in the three groups of QLEDs, at least at this current.

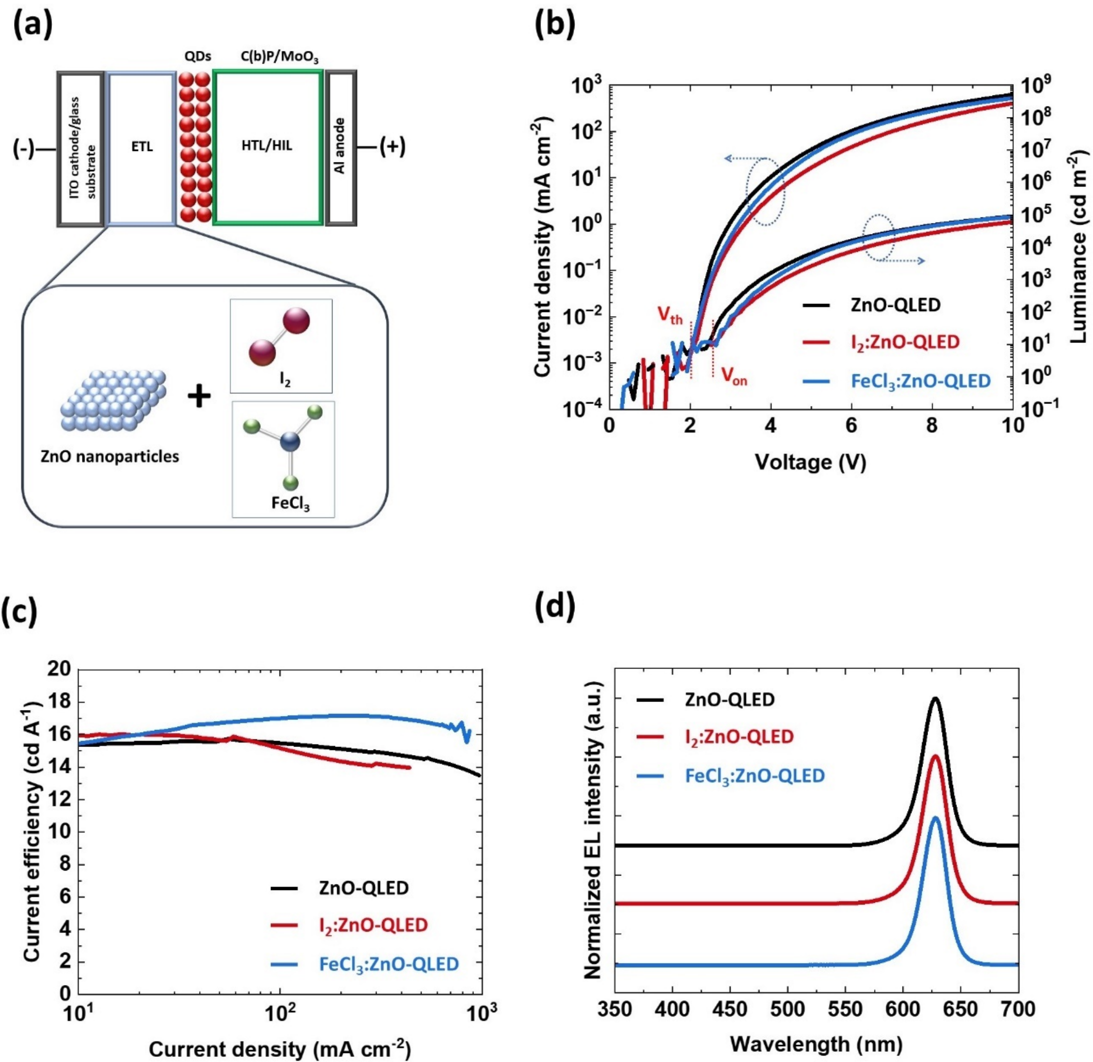

Figure 4.6 (a) Schematic diagram of the structure of the QLEDs used in this work. (b) J-V-L characteristics, (c) current efficiency *vs.* current density, and (d) EL spectra of QLEDs with ZnO, I_2:ZnO, and $FeCl_3$:ZnO ETLs.

Next, we test the EL stability of the devices under 20 mA cm^{-2} constant current driving. We measure LT50, the time for EL to reach 50 % of the L_0 intensity and commonly referred

to as device EL lifetime, to compare the EL stability among the QLEDs. Figure 4.7 (a) shows the EL lifetime and the current efficiency of 14 devices from each group. As can be seen, while the devices generally exhibit only minor differences in their current efficiency, incorporating I_2 and $FeCl_3$ into ZnO results in a significant increase in their EL lifetimes. The $FeCl_3$:ZnO-QLEDs have the longest EL lifetimes (average value 206.1 hours), followed by the I_2:ZnO-QLEDS (average value 124.3 hours). In contrast, the ZnO-QLEDs have the shortest EL lifetime (average value 56.9 hours). It should be noted that all devices have comparable initial EL values, consistent with their comparable initial current efficiencies at this current density. One notable additional observation is that the QLEDs with the doped ETLs, especially the $FeCl_3$:ZnO ETLs, exhibit a larger variation in their LT50 values (a relatively larger standard deviation). This might be due to the high chemical reactivity of halides which makes them more easily affected by external factors. The increase in EL lifetime upon using the dopants however clearly well exceeds these variations. We also found no strong correlation between the current efficiencies and the EL lifetimes of devices within each group, as can be shown in Figure S4.1, which indicates that the variations in the lifetimes of devices within each group are not primarily driven by differences in radiative e-h recombination efficiencies in them. Representative EL *vs.* time traces of the QLEDs are shown in Figure 4.7 (b). The L_0 at 20 mA cm^{-2} values are 3,200 cd m^{-2}, 3,260 cd m^{-2}, and 3,310 cd m^{-2} for the ZnO-, I_2:ZnO-, and $FeCl_3$:ZnO-QLEDs, respectively. The measured LT50 values are 71 hours, 124 hours, and 237 hours for the QLEDs with the ZnO, I_2:ZnO, and $FeCl_3$:ZnO ETLs, respectively. Driving voltage *vs.* time traces during the electrical aging time are shown in Figure 4.7 (c). The driving voltage of all QLEDs generally decreases pointing to an increase in charge conduction across the devices. The ZnO-QLED shows the largest decrease in driving voltage over time, which also happens rapidly within the first two hours. The driving voltages of the I_2:ZnO-QLED and $FeCl_3$:ZnO-QLED also decrease but to lesser extents and at slower rates, especially for the latter. These observations suggest that the electrical aging-induced changes in device conductivity are significantly affected by the presence of the I_2 and $FeCl_3$. We further investigate the differences in the EL loss rates among the QLEDs by calculating the first

derivative of the EL *vs.* time data in Figure 4.7 (b). Figure 4.7 (d) shows the resulting EL change rate *vs.* time. As seen from the Figure, the rate of EL loss is much faster in the initial 30 hours in case of the ZnO-QLED relative to that in the other two devices. Interestingly, all QLEDs exhibit similar rates after 50 hours. This observation suggests that the loss in EL occurs via different processes in the short (i.e., the initial 30~50 hours) and long (> 50 hours) terms. Given the slower EL loss rate in the I_2:ZnO- and $FeCl_3$:ZnO-QLEDs in the first 30 hours, investigating the changes within the initial 30 hours and any differences in them among the devices can provide insights into the causes of the faster device degradation in case of the ZnO-QLEDs.

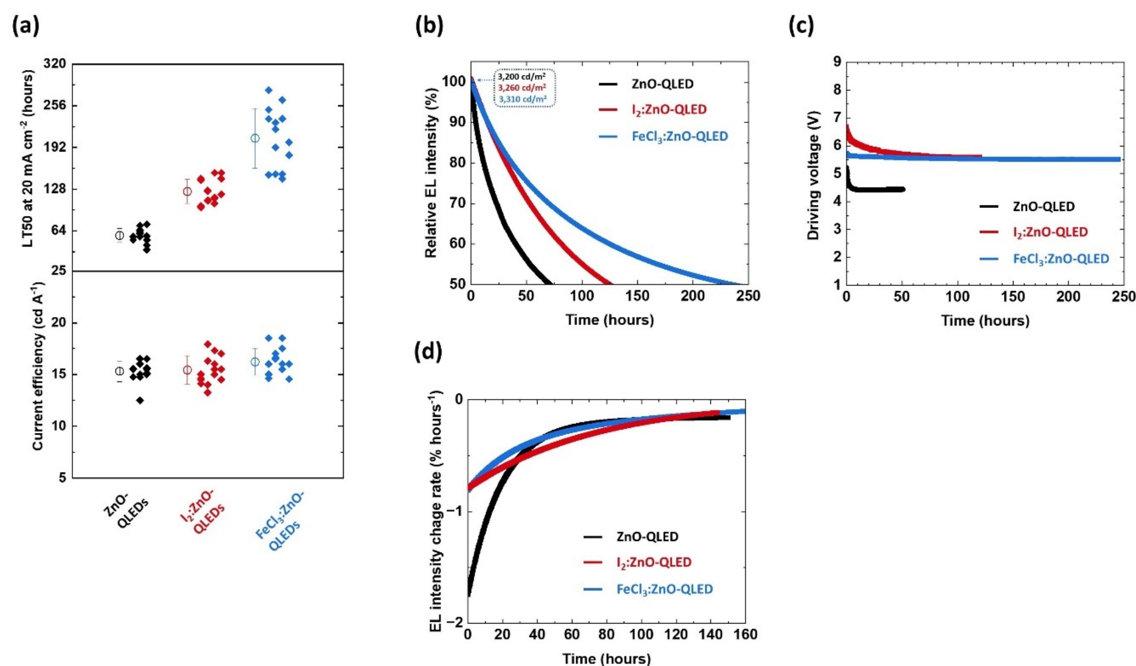

Figure 4.7 (a) The initial current efficiency and LT50 at 20 mA cm^{-2} of all 14 QLEDs in each of the three groups. The round symbols and error bars give the average and standard deviation values of the same data for each group. (b) EL *vs.* time, (c) driving voltage *vs.* time, and (d) EL change rate *vs.* time of representative QLEDs from each group (i.e., with ZnO, I_2:ZnO, and $FeCl_3$:ZnO) under 20 mA cm^{-2} constant current driving.

4.3 Chapter Summary

The research discussed in this chapter proposes new approaches for ZnO modification for improving QLED performance, generally focused on the EL stability. Blending PEI and ZnO to form a ZnO:PEI nanocomposite ETL improves device efficiency by more than 50 % compared to QLED with only ZnO ETL. The ZnO:PEI ETL has a significant advantage in terms of improving device stability. A device with a ZnO:PEI ETL containing 0.3 wt% PEI exhibits an LT50 of 153,735 hours (for L_0 of 100 cd m^{-2}), almost 10× longer than a ZnO ETL control device. Chemically treating the ZnO NP ETLs of QLEDs by F plasmas, using carbon tetrafluoride (CF_4) as a source gas, leads to significant improvements in EL lifetime, demonstrating an LT50 at 100 cd m^{-2} of 2,370,000 hours QLED, 47× longer than untreated ZnO. Introducing other halogen species, i.e., I_2 and $FeCl_3$, into ZnO ETL also brings about the increase in LT50 of QLEDs. I_2:ZnO and $FeCl_3$:ZnO increase the LT50s for L_0 of 3,000 cd m^{-2} by 2.2× and 3.6×, respectively, demonstrating 124.3 hours and 206.1 hours instead of only 56.9 hours in devices with undoped ZnO.

In QLEDs, charge concentrations and their build-up in the layers bulk and at interlayer interfaces directly influence excitonic phenomena and the efficiency of the radiative processes. As discussed in the Chapter 2 and Section 2.4, most of the approaches for modifying and optimizing electrical properties of the ZnO and the ZnO/QDs interface have attempted to improve the charge balance within the QD EML by reducing the charge transport property of the ZnO and injection efficiency at the ZnO/QDs interface. As also discussed, solution-processed ZnO ETLs have structural and stochiometric defects that can act as exciton quenching sites at the ZnO/QDs interface and thereby affect EL of the QLED. The lack of a complete and accurate understanding of these interfacial phenomena, however, often leads to contradictory findings when attempting to resolve performance issues in QLEDs. In Figure 4.8, the statistical results depicting the relationship between LT50 and the charge balance factor of the QLEDs are presented. These QLEDs are fabricated using different dopant treatments of ZnO. The dopants are introduced into ZnO solution. As seen, the experimental results indicate

that improved charge balance can enhance the EL stability in a low charge balance state. However, when a full QLED reaches a high enough efficiency and therefore a high charge balance state via the ZnO modifications, the correlation between the charge balance state and the EL stability may no longer hold. This suggests that other factors may become dominant in determining EL stability. Therefore, it is important to gain a better understanding of the role of ZnO in limiting device stability and of the mechanisms behand the stability improvement.

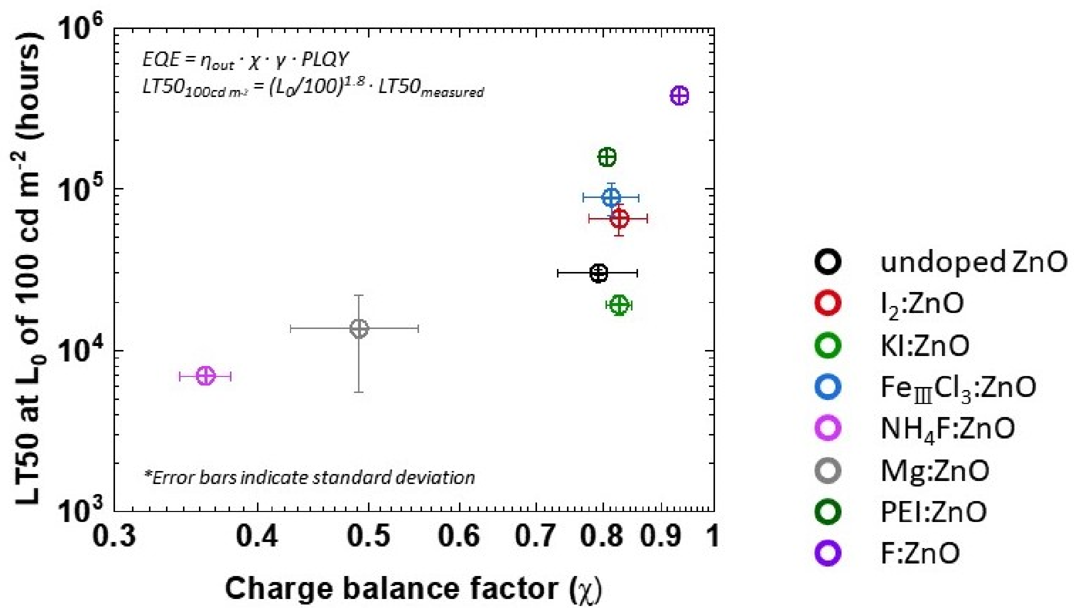

Figure 4.8 The LT50s of QLEDs with various ETLs vs. charge balance factors extracted from EQEs of the QLEDs.

Chapter 5 The Influence of ZnO Modifications on Positive Charge Accumulation at the QD EML/HTL Interface

This work has been published in DS Chung et al., Nanoscale Advances, 3 (20), 5900-5907, 2021, and DS Chung et al., Nano-Micro Letters, 14 (1), 212, 2022, and DS Chung et al., Organic and Hybrid Light Emitting Materials and Devices XXVI, 12208, 23-28, 2022. It has been reproduced in part with permission from the publisher.

In the previous Chapter 4 and the Section 4.1 and 4.2, the significant device stability improvements by the ZnO modifications are discussed. First, the ZnO:PEI ETL has a significant advantage in terms of improving device stability, as discussed in the Section 4.1. A device with a ZnO:PEI ETL containing 0.3 wt% PEI shows the LT50 of 153,735 hours (for L_0 of 100 cd m^{-2}), almost 10× longer than a ZnO ETL control device. Second, the Section 4.2 discusses the significant device stability improvement by CF_4 plasma treatment on ZnO. Chemically treating the ZnO NP ETLs of QLEDs by F plasmas, using carbon tetrafluoride (CF_4) as a source gas, results in significant improvements in the EL lifetime, demonstrating an LT50 at 100 cd m^{-2} of 2,370,000 hours QLED. This represents the 47× increase in lifetime compared to untreated ZnO. In this Chapter, the impact of these ZnO modifications on device stability improvement is discussed. In the Section 5.1, the changes in charge distribution across QLED by using ZnO:PEI and its impact on the hole accumulation at the QDs/HTL interface are discussed. In order to investigate the charge distribution, delayed EL measurements, the analysis of J-V characteristics in the electron-only devices, and the measurements of EL spectra of QLEDs with the marking layer are utilized. The Section 5.2 focuses on the influence of F-incorporation on the trap state of ZnO and its consequential impact on the electron concentration within the QD EML. For this investigation, TRPL *vs.* bias measurements and C-V-L measurements as well as the EL spectra of QLED with the marking layer are employed.

5.1 Changes in Charge Distribution across QLED by ZnO:PEI

5.1.1 Deeper Penetration of Electrons into HTL by ZnO:PEI

Delayed EL Measurements for QLEDs with ZnO, ZnO/PEI, and ZnO:PEI

Seeing in the Chapter 4 and the Section 4.1 that the ZnO:PEI ETLs lead to a greater EL stability, comparative delayed EL measurements on QLEDs with ZnO:PEI$_{0.3}$, ZnO/PEI and ZnO ETLs are carried out to try to glean additional insights into the influence of the various ETLs on altering charge distribution within the devices. The delayed EL measurements are performed using an experimental setup as described in the Chapter 3 and the sub-section 3.2.2 and for which a schematic is further provided in Figure 5.1[46,163]. In the delayed EL technique, the QLEDs are driven with a 500 µs forward bias square pulse of magnitude equivalent to the driving voltage required to achieve a current density of 20 mA cm^{-2} and allow prompt EL to reach steady state. Modulating the forward bias voltage to obtain the same current density ensures that the number of charges injected during the forward bias pulse is similar in all devices. It also allows for the study of delayed EL behavior for devices under the same electrical driving conditions that the EL stability tests were conducted under. An optical chopper system is activated to record the EL 50 µs following the end of the forward bias pulse. This delay is sufficiently long for all allowable luminescent exciton relaxation processes to occur and is much larger than a typical QLED electrical time constant, rendering electrical transient effects negligible. Therefore, any measured EL signal will arise from radiative decay of excitons that are formed after the termination of the forward bias pulse.

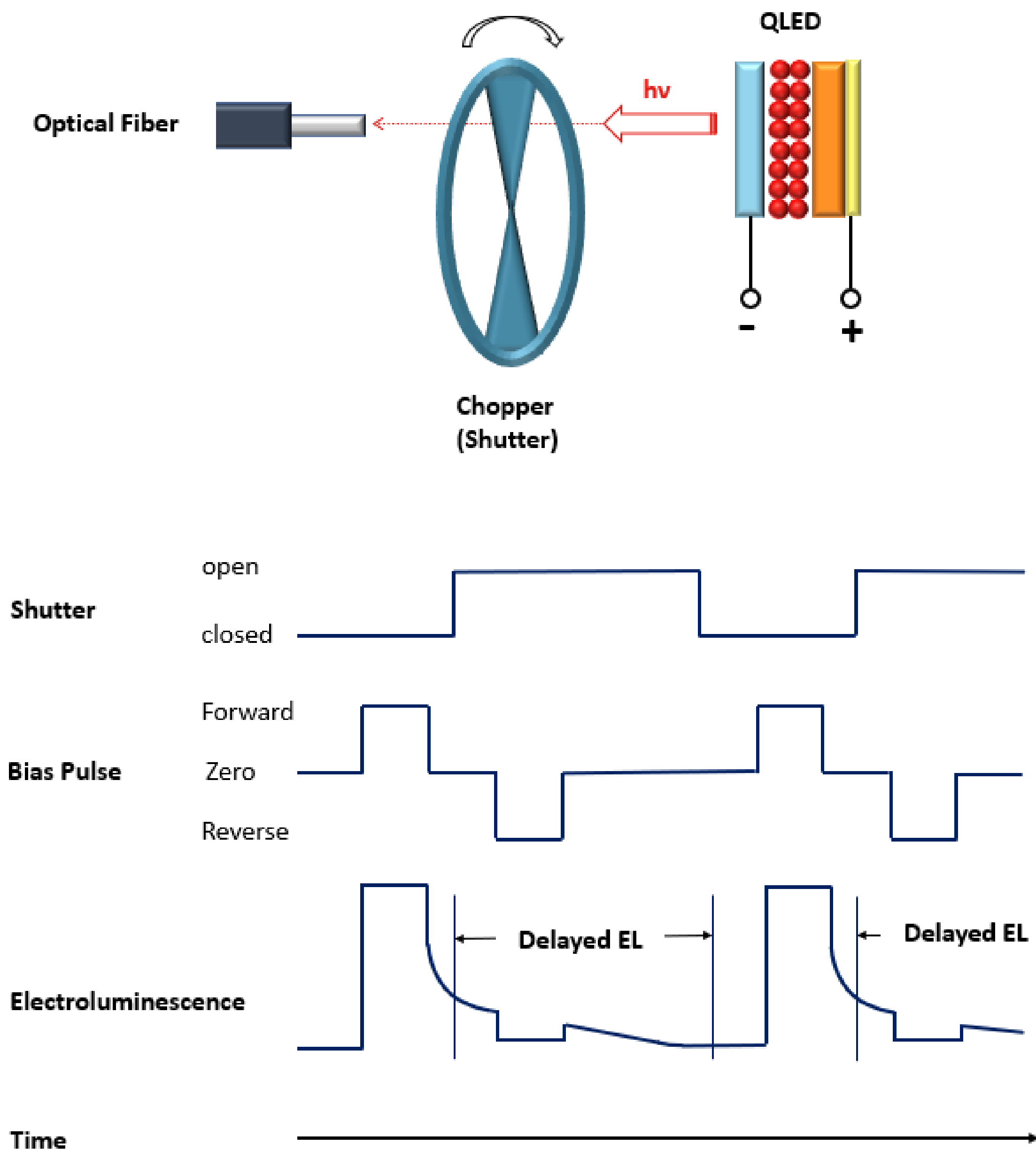

Figure 5.1 Schematic images of delayed EL measurement setup. Timings of shutter open/close, bias pulse, and EL are illustrated.

Figure 5.2 depicts the delayed EL intensity signal versus time collected from the QLEDs. In this figure, time = 0 on the x-axis corresponds to 50 μs after the end of the forward bias, the time when the optical chopper is completely open. The data is normalized to the intensity at time = 0 to facilitate comparison. The delayed EL signal has the same decay rate in all devices, suggesting that the mechanistic process behind the delayed EL is the same in all of them. In general, the formation of excitons after the termination of the forward bias pulse in QLEDs can arise from two processes[72,102,164]: (i) recombination of residual (trapped/accumulated) charges in the various device layers including the HTL that become mobile and capable of recombination, producing luminescence after the forward bias pulse has ended and/or (ii) triplet excitons created within the HTL that diffuse slowly and eventually reach and excite the QDs by energy transfer either directly from those triplet states (by a Dexter process) or by a Förster process from singlet intermediates produced by triplet-triplet annihilation (TTA). To identify the main process behind the delayed EL, we investigate the effect of applying a reverse bias pulse, 200 μs long, applied 650 μs after the opening of the optical chopper on the delayed EL characteristics. It is known that in devices where process (i) is the dominant mechanism behind the delayed EL, the application of a reverse bias will lead to a permanent reduction in the delayed EL intensity and is sometimes accompanied by the appearance of EL spikes at the beginning and end of the reverse bias pulse due to the redistribution of charges which provides opportunities for electron-hole recombination. On the other hand, in devices where process (ii) is more dominant, the reverse bias will result in only a temporary decrease in the delayed EL signal due to electric-field induced dissociation of excitons which recovers completely after the reverse bias ends. Figure 5.2 (b-d) show the effect of applying a reverse bias pulse of two different magnitudes (5 V and 7.5 V) on the delayed EL signal from the same set of devices. The data is normalized to the delayed EL intensity at t = 0 in order to facilitate the comparison. As can be seen, in addition to the temporary decrease in EL intensity during the pulse, the reverse bias leads to a permanent reduction in the intensity (observed over the 0.4-0.6 ms range on the figures) as well as a sharp delayed EL spike at the end of the pulse (observed at 0.4 ms on the figures), indicating that the delayed EL arises

primarily from the recombination of residual charges (i.e. process (i)). In this regard, the reverse bias sweeps out residual electrons and holes in the device layers towards the cathode and anode respectively, away from the QD EML. Therefore, when the reverse bias ends, some of these charges move back towards each other, driven by diffusion and Coulombic forces, producing new electron-hole recombination events and hence the EL spike at the end of the reverse bias. The subsequent permanent reduction in the delayed EL intensity, on the other hand, is due to the permanent removal of residual charges by the reverse bias. As seen, this permanent reduction is larger in case of the ZnO and ZnO/PEI devices relative to their ZnO:$PEI_{0.3}$ counterpart (and is larger, although only marginally, in the ZnO device relative to the ZnO/PEI device). The larger reduction suggests that residual charges in these devices are generally more mobile and thus can be swept out more easily by the reverse bias. By contrast, the smaller reduction in case of the ZnO:$PEI_{0.3}$ device points to the presence of a significant number of less mobile (i.e., strongly trapped) charges. One can also see that increasing the magnitude of the reverse bias (from 5 V to 7.5 V) does not appreciably affect the magnitude of this reduction in case of the ZnO/PEI or the ZnO devices, again pointing to the more mobile nature of the residual charges in them which makes it possible for even the lower reverse bias to sweep them out as effectively. This is in contrast to what is observed in case of the ZnO:$PEI_{0.3}$ device where the higher reverse voltage leads to a larger reduction in the delayed EL, reflecting the role that the reverse bias plays in de-trapping the immobile (i.e., strongly trapped) charges that are present in this case. Although it is not possible to determine the polarity or location of these trapped charges from the delayed EL characteristics, they may indeed be electrons into the CBP HTL, correlating these results with those from the FIrpic marking layer devices discussed later in this Chapter. This is also in view of the fact that electrons have a much lower mobility compared to holes in CBP (electron and hole mobility are 3×10^{-4} $cm^2 \cdot V^{-1} \cdot s^{-1}$ and 2×10^{-3} $cm^2 \cdot V^{-1} \cdot s^{-1}$, respectively.[165]) and hence need higher reverse voltages to be de-trapped from their sites in the HTL bulk. This would suggest that some of the electrons that penetrate into the HTL in case of the ZnO:PEI devices remain deeply trapped in the HTL. This may perhaps explain the different trajectories of the driving voltage versus

time trends in Figure 4.2 (b) where the ETLs that lead to a deeper penetration of electrons into the HTL (i.e., the ZnO:$PEI_{0.3}$ and ZnO:$PEI_{0.1}$) eventually lead to a faster voltage rise relative to ZnO/PEI ETL that leads to only limited electron penetration. Because in case of the ZnO:PEI devices the location of this electron space charge is deep inside the HTL away from the QD interface, it does not appreciably quench the luminescence of the QDs and therefore does not affect the EQE. By contrast, the more mobile charges in the ZnO and ZnO/PEI devices might therefore be holes in the CBP HTL. Regardless of the specific polarity of the charges or their location, the delayed EL results clearly show that the ZnO:$PEI_{0.3}$ ETL significantly alters charge distribution in the device (much more than the ZnO/PEI ETL) changing the nature of residual charges that remain unrecombined from ones that are more mobile to ones that are more strongly trapped. It is also notable to point out that the ZnO/PEI device shows an additional delayed EL spike at the beginning of the reverse bias pulse. That only this device shows this spike suggests that residual charges in the PEI layer may be involved in its appearance. (For example, holes that reach the PEI layer and get trapped into it during the forward bias pulse that then get de-trapped and pulled back towards the QD layer upon applying the reverse bias pulse where they recombine with residual electrons.)

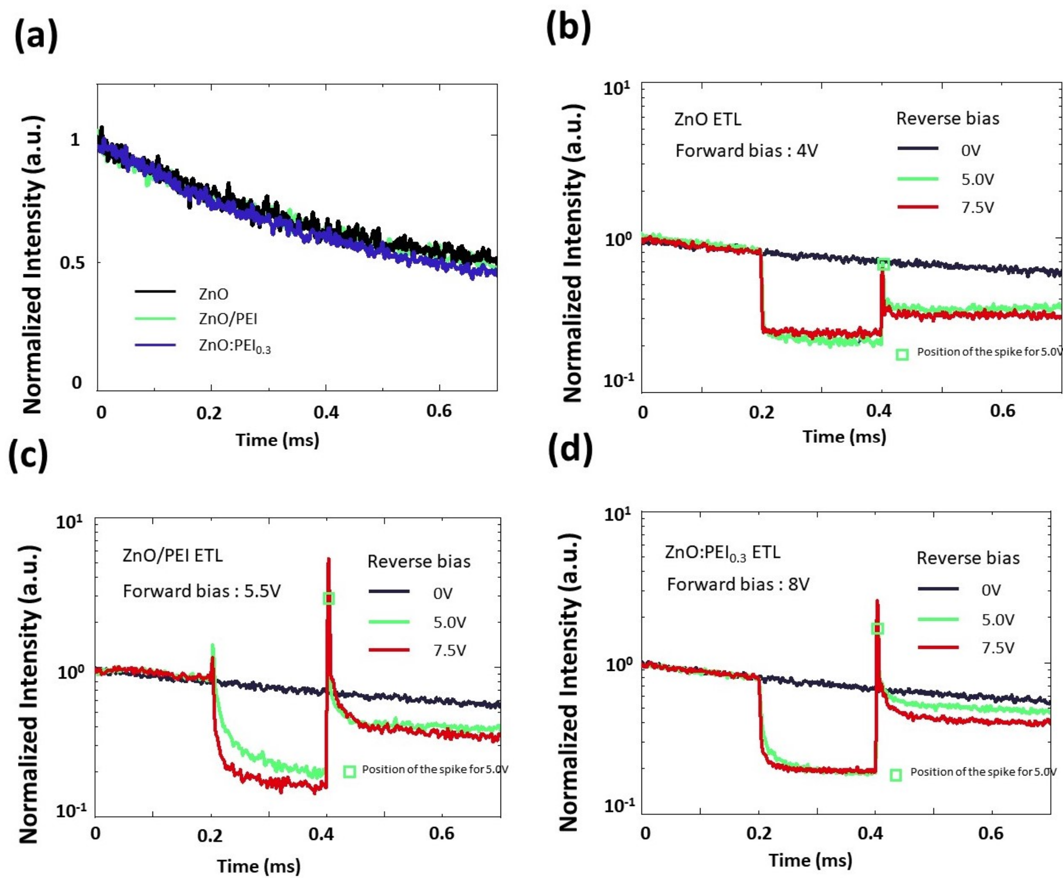

Figure 5.2 (a) Delayed EL of QLEDs with different ETLs. Reverse bias with 200 μs pulse on-time was applied at 0.2 ms. Delayed EL with increasing reverse bias of QLEDs with (b) ZnO, (c) ZnO/PEI, and (d) ZnO:$PEI_{0.3}$.

Electron-only Devices with ZnO, ZnO/PEI, and ZnO:PEI

To verify that the use of PEI indeed reduces the supply of electrons, and thereby the conclusion that the deeper penetration of electrons into the HTL in case of the ZnO:PEI devices must be the result of a higher electric field within the QLED structure we test the ETLs in unipolar electron-only devices (EODs). The structure of the EOD was similar to the QLEDs

except that the MoO_3 layer was replaced by a 10 nm LiF layer. The general device structure of these EODs therefore is: ITO/ETLs/QD/CBP (30 nm)/ LiF (10 nm)/Al (100 nm) and is illustrated in Figure 5.3 (a). Under forward bias, i.e., when ITO is at a more negative potential relative to the Al contact, the injection of holes from the Al contact is blocked by the LiF layer. The flow of current therefore proceeds only by electrons, which get injected in the device at the ITO contact and collected at the Al contact. Figure 5.3 (b) shows the J-V characteristics of these EODs, each comprising one of the four ETL configurations. As can be seen the current at any given voltage decreases in the order (from highest to lowest): ZnO → ZnO/PEI → ZnO:$PEI_{0.1}$ → ZnO:$PEI_{0.3}$, indicating that electron supply by the ETLs becomes harder in the same direction which is in line with what was inferred from the changes in the J-V characteristics of the QLEDs in Figure 4.1 (b). The deeper penetration of electrons into the HTL in case of the ZnO:PEI ETLs must therefore be the result of a higher internal electric field in these devices, induced by the more difficult supply of electrons. The almost parallel J-V traces and their linearity over the voltage range suggest that electrons can be injected into the CBP HTL from the QD layer and travel across it relatively easily.

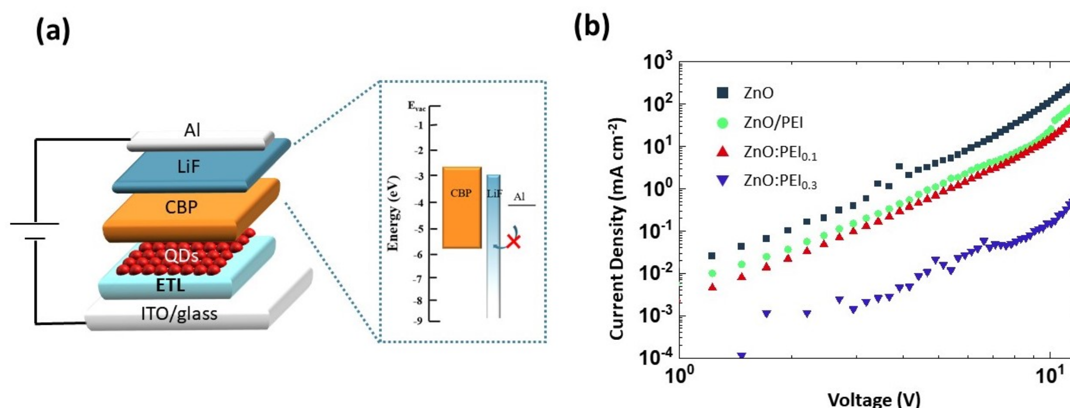

Figure 5.3 (a) Schematic diagram showing the general structure of the EODs. (b) J-V characteristics of EODs with the different ETLs.

5.1.2 Electron-hole Recombination at the QD EML/HTL Interface

Finding that the ZnO:PEI ETL devices and that the use of PEI in the ETLs significantly affects both the J-V characteristics (Figure 5.3 (b)) and the increase in driving voltage over time (Figure 4.2 (b)) as well as charge distribution investigated by delayed EL measurements (discussed in Figure 5.2), we investigate if the ETLs affect the electron-hole recombination zone or otherwise alter the distribution of electrons and holes in the HTL. The devices that contain a thin luminescent marking layer in the HTL is fabricated, which will emit light if excitons are created nearby. The 10 nm marking layer consisted of 10 % bis(2-(4,6-difluorophenyl)pyridinato-C2,N) (picolinato) iridium (III) (FIrpic) by volume doped into the CBP HTL. FIrpic is selected because of its comparable energy band structure to CBP which minimizes altering charge distribution from that in the original devices. In addition, its high quantum yield and luminescence in the 450-550 nm range, far from the QD emission band (at 632 nm), make it relatively easy to distinguish its EL. The marking layer was placed 10 nm away from the QD/HTL interface in order to avoid quenching FIrpic via energy transfer to the QD layer.[166] The general device structure of these devices therefore is: ITO/ETLs/QD EML/CBP (10 nm)/CBP:FIrpic (10 nm)/CBP (30 nm)/MoO_3 (5 nm)/Al (100 nm). Figure 5.4 (a) shows the general device structure whereas figure 5.4 (b) shows the EL spectra measured from QLEDs incorporating the different ETLs while driven at 20 mA cm^{-2} current density. The spectrum of a ZnO device without a marking layer is also included for comparison. All the spectra are normalized to the QD emission band peak intensity to facilitate comparison. The ZnO:PEI devices show significant emission from the FIrpic marking layer indicating that a significant number of electrons can penetrate into the HTL and reach the marking layer where they recombine with holes to produce EL. In stark contrast, the spectrum of the ZnO/PEI device shows only very weak (but discernable) emission from FIrpic, indicating that the penetration of electrons into the HTL is much less in this case. The ZnO device shows no detectable FIrpic emission, evident from the comparable background noise to that of the control device without the marking layer over the 450-550nm range. For any given current density, a higher electron

current requires that the hole current must be proportionally lower at the same device cross sectional plane indicating that hole currents must be somewhat lower in the HTL near the QD interface in case of the ZnO:ETL devices. A deeper penetration of electrons into the HTL also points to a lower concentration of accumulated holes in the HTL at the QD/HTL interface, otherwise the electrons would have been annihilated (i.e., neutralized) by recombination with these holes. The fact that this effect is strongest in case of the ZnO:PEI devices and that these devices also exhibit a significantly higher EL stability suggests that there is a correlation between the two phenomena. In this regard the higher stability is possibly associated with a lower concentration of holes in the HTL at the QD/HTL interface whose presence in high concentrations would otherwise reduce the luminescence of the QD EML by Auger quenching or by degrading the HTL in the vicinity of the HTL/QD by excitons.[102] While the deeper penetration of electrons into the HTL in case of the ZnO:PEI devices may seem inconsistent at first glance with the shifts in the J-V characteristics which suggest that these ETLs make electron injection and transport more difficult, it is possible that restricting the electron supply leads to higher internal electric fields within the device that facilitate hole injection from the HTL into the QD layer and/or the penetration of electrons into the HTL, either of which would reduce hole accumulation in the HTL at the QD/HTL interface. For example, reducing the number of electrons in the QD layer would be expected to lead to a higher electric field across it which may help energy band bending at the QD/HTL interface and facilitate hole injection. The increased hole injection may, in turn, reduce the hole space charges at the QD/HTL interface leading to a higher electric field across the HTL that can help electrons to penetrate into it. Indeed, increasing the driving voltage has been found to alter the relative height of the FIrpic band and not always in the same direction (for example the height of the FIrpic band first increases on increasing the driving voltage but then the trend reverses at higher voltages, as shown in Figures 5.4) pointing to changes in electric field distribution within the device and the strong dependence of the extent of electron penetration into the HTL on them. In this regard, the higher stability of the ZnO:$PEI_{0.3}$ device in comparison to its ZnO:$PEI_{0.1}$ counterpart even though the results in Figure 5.4 (b) point to a deeper penetration of electrons in case of the

latter device may be due to differences in the internal electric field distribution in the two cases that facilitate hole injection from the HTL to the QD in the earlier and thus lead to a lower hole space charge in the vicinity of the QD/HTL in it. The higher EQE of the ZnO:$PEI_{0.3}$ device relative to its ZnO:$PEI_{0.1}$ counterpart at 20 mA cm^{-2} (reflected in their L_0 values of 3,250 cd m^{-2} versus only 3,000 cd m^{-2} at this current) supports this notion as it points to better charge balance in case of the ZnO:$PEI_{0.3}$ device indicating that hole injection from the HTL to the QD may indeed be greater in this device.

Figure 5.4 (c) shows that QLEDs with ZnO exhibit negligible emission from FIrpic in entire voltage range, suggesting excessive electrons cannot reach CBP:FIrpic marking region. In figure 5.4 (d), FIrpic emission in a QLED with ZnO/PEI slightly increases at 10V, suggesting that excessive electrons reach CBP:FIrpic marking layer. It could be expected that higher applying voltage will increase FIrpic emission in QLED with ZnO/PEI. FIrpic emission greatly increases along with voltage range from 6V to 10V in QLEDs with ZnO:PEI 0.1 wt% and 0.3 wt% as can be shown in figure 5.4 (e) and (f). On the other hand, in higher voltage range in Figure S5.1 (a) and (b), FIrpic emission ratio decreases as voltage increases. This may be because either electrons and holes move further toward the opposite direction, i.e., electrons and holes drift toward anode and QD, respectively, or excitons in CBP:FIrpic layer are dissociated by strong electric field. This result indicates electric field forces excessive electrons to overcome the QD/HTL interface.

(a)

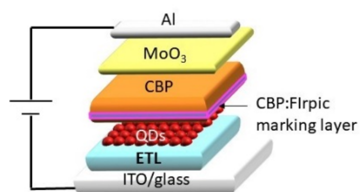

(b)

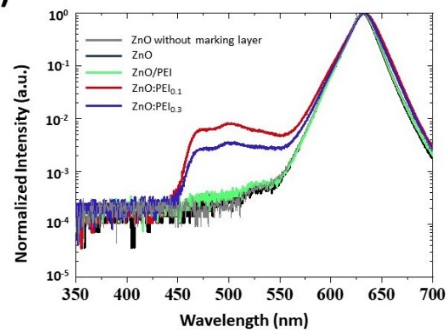

(c)

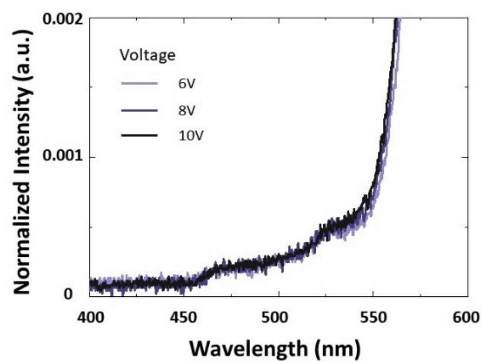

(d)

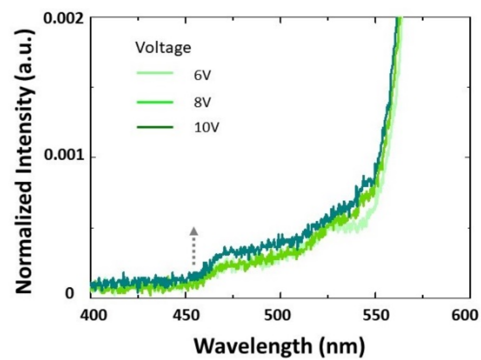

(e)

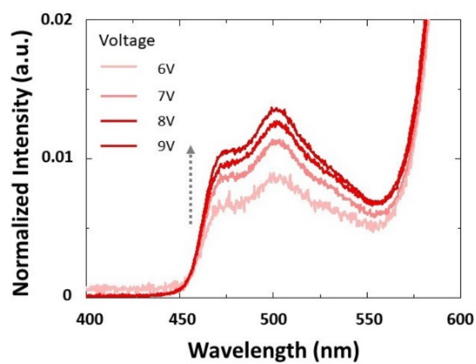

(f)

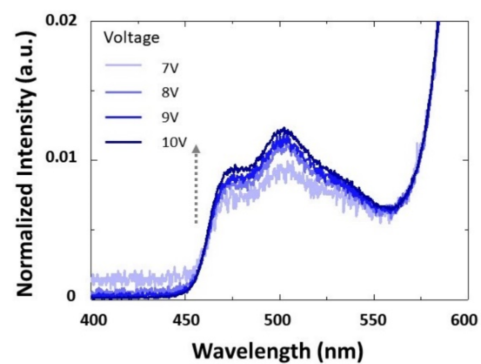

Figure 5.4 (a) Schematic diagram showing the general structure of the QLEDs with the CBP:FIrpic luminescent marking layer. (b) EL spectra from these with the various ETLs under 20 mA cm^{-2}. A spectrum from a ZnO ETL control device without the marking layer is also included for comparison. EL spectra from the QLEDs with the marking layer with (c) ZnO, (d) ZnO/PEI, (e) ZnO:$PEI_{0.1}$, and (f) ZnO:$PEI_{0.3}$ at various forward bias voltages.

5.2 Changes in Electron Concentration within QD EML by FZnO

5.2.1 Reducing Trap Density in ZnO by F-incorporation and its Impact on Electron Concentration within QD EML

While the F incorporation in ZnO via the CF_4 plasma treatment clearly leads to a significant enhancement in device stability as discussed in the Chapter 4 and the Section 4.2, it is unlikely that the enhancement is due to an increase in the chemical stability of the ETL. This is because ZnO is already thermodynamically stable[33,112,113,167]. The effect might be associated with changes in exciton relaxation dynamics in the QD EMLs due to the passivation of ZnO surface defects or in charge distribution across the QD EMLs[46,102]. It is known that a change in charge distribution in the QD EMLs could affect device stability. The electron transport characteristics of the FZnO *vs.* ZnO ETLs are therefore studied and compared in EODs. Additionally, TRPL measurements are used to study and compare the influence of electron currents on QD exciton lifetime. Figure 5.5 (a) depicts a schematic diagram of the experimental setup. In order to avoid the injection of holes from the Al electrode when under bias, and, at the same time, minimize – as much as possible – perturbations that may arise from differences in device structure between the EODs and the actual QLEDs, the same layer stack composition is used in the EODs as was used in the QLEDs except that the MoO_3 layer was replaced by a 3 nm thick LiF layer in order to block hole injection into CBP. The inset in Figure 5.5 (a) illustrates the energy levels of the QDs/CBP/LiF/Al portion of the EOD, showing the large hole injection barrier behind the hole-blocking nature of the contact. It also should be noted that the devices do not emit any detectable EL over the voltage range of the

measurements proving that hole injection is indeed insignificant. Figure 5.5 (b) depicts and compares the J-V characteristics of ZnO-EOD and FZnO-EOD. The characteristics suggest an ohmic contact at the ETLs/QD EML interface which may explain why the threshold voltage of the QLEDs (in Figure 4.4 (b)) was not significantly changed. As can also be seen, the current at any given voltage is lower in case of the FZnO-EOD suggesting that the presence of fluorine reduces electron conduction across the ETL, which can be ascribed to the passivation of oxygen vacancies[36] and is consistent with the changes in the J-V characteristics of the QLEDs observed in Figure 4.4 (b). The characteristics also have somewhat different shapes pointing to different charge transport behaviors. In case of the ZnO-EOD, the characteristics show a well-defined inflection point at around 2 V. The FZnO-EOD characteristics, in contrast, show what could be a much less defined inflection point at below 0.5 V, although, given the lower current levels in this case (below 1 μA cm^{-2}) instrument limitations can make the measurements accuracy less certain. The clear change in slope at the inflection point – at least in case of the ZnO-EOD – points to a change in the dominant carrier transport mechanism between the low and high voltages[168-170]. At voltages below 2 V, the ZnO-EOD characteristics exhibit a slope of 1.3 suggesting trap-limited space charge limited current. In contrast, at voltages above 2 V, the characteristics of both devices exhibit a slope of 3.1 suggesting conduction becomes dominated by trap-filled carrier transport. In general, the transition voltage, V_{TF}, at which the transition from trap-limited to trap-filled carrier transport occurs will depend on[168-170]

$$V_{TF} = \frac{q \cdot N_t \cdot t}{2\varepsilon_0 \varepsilon_r} \tag{5.1}$$

where t and ε_r represent the layer thickness and dielectric constant, respectively, and N_t represents the trap density, which in our ETLs scales with the density of oxygen vacancies. The higher V_{TF} in the ZnO-EOD relative to the FZnO-EOD implies that a larger number of trap states (i.e., oxygen vacancies) exists in ZnO than in FZnO, and is consistent with the defect-passivation effect of the fluorine observed in Figure 4.3 (d-f) The derived N_t values of

the EODs are 1.39 × 10^{18} cm^{-3} for the ZnO-EOD and 1.61 × 10^{17} cm^{-3} for the FZnO-EOD, indicating a reduction in trap states by F-incorporation.

With knowledge that the oxygen vacancies in ZnO are filled via fluorine incorporation, the effect of electron injection on QD lifetime was subsequently evaluated and compared in the EODs. In order to accomplish this, TRPL measurements on the QD layers in the EODs were conducted at the QD peak emission wavelength of 630 nm via excitation with a 380.2 nm laser pulse while a bias was simultaneously applied to the device as illustrated in Figure 4a. In general, the decay in PL intensity over time PL(t) subsequent to the excitation can be deconvoluted into multiple exponential decay components each having a lifetime τ_n that is characteristic of the underlying exciton deactivation process according to the curve fitting equation:

$$PL(t) = \sum_{n=1}^{3} A_n \exp\,(t/\tau_n) \tag{5.2}$$

where A_n is a weighting coefficient. Table S5.1 gives the extracted values for the τ and A parameters assuming a tri-exponential decay rate. In QDs, the fastest exciton deactivation process is typically dominated by non-radiative recombination at the layer interfaces[171] as well as by negative trion decay[12,13,172,173]. The τ_1 values are therefore the most relevant for this analysis. In the absence of an external bias, the TRPL measurements show a lower exciton decay rate (in Figure 5.5 (c)) and a larger τ_1 value (in Figure 5.5 (d)) in case of the FZnO, evidence of a reduction in the non-radiative deactivation of excitons by defects at the ETL/QD in the treated samples, consistent with the above results. Given its influence by negative trion decay, one can expect τ_1 to also be strongly affected by electron injection. TRPL measurements, therefore, are also done on the EODs under forward bias (i.e., with the ITO held at a more negative potential relative to the Al contact) to investigate the effect of current flow on exciton decay rate. The approach taken here is different from that sometimes followed in other reports where TRPL measurements are carried out under reverse bias or with blocking contacts for the

purpose of investigating the effect of electric fields - without any current flow - on exciton lifetime[174,175]. As can be seen in Figure 5.5 (d), applying the forward bias leads to changes in QD exciton lifetimes and τ_1 values. Notably these changes are quite different in the two devices, with the increase in voltage leading to a progressive increase in τ_1 in case of the ZnO-EOD but an opposite trend initially in case of the FZnO-EOD before the trend reverses and τ_1 also starts to increase with bias although to a lesser extent than in the control device. An increase in τ_1 with bias is opposite to what one would expect from the familiar phenomenon of electric field-induced exciton dissociation and shows that the observed changes in τ_1 are indeed current-induced rather than field-induced. It should be also noted that applying a reverse bias was found to have a negligible effect on τ_1 (as can be shown in Figure S5.2), further proving that the changes observed under the forward bias are driven by the current flow rather than by the fields. Considering that carrier transport is trap-limited in these ETLs, filling the traps in ZnO with electrons may contribute to the increase of τ_1 in the ZnO-EOD. In other words, the continuous supply of electrons from the cathode neutralizes the oxygen vacancies in ZnO leading to a reduction in exciton dissociation at the ZnO/QD interface. In contrast, since a large fraction of the trap states is already passivated by the fluorine, the flow of current leads to a more modest increase of τ_1 in the FZnO-EOD and only at higher voltages (> 3 V) when current levels become significant. The initial decrease, rather than increase, in τ_1 observed at the low voltages in this case might stem from the presence of the faster decaying channel from negative trions whose concentrations in the QD layer of the FZnO-EOD can be expected to be higher due to the higher electron concentrations from the lower onset of reaching trap-filled transport in case of FZnO. As these trions become easily dissociated at high electric fields, their influence on τ_1 subsides at the higher voltages (i.e., at > 3 V or 300 kV cm^{-1})[176]. The presence of a large number of injected electrons at the higher voltages increases their electric-field screening effects which may reduce the field-induced trion dissociation, hence the late onset of this effect. Regardless of the specific mechanism, the different bias-dependence of exciton lifetime in the two EODs indicates that replacing ZnO with FZnO as the ETL changes electron distribution in the device stack possibly leading to higher electron concentrations in the QD

layer near the QDs/HTL interface. The higher electron concentration within the QD EML when using FZnO may be behind the significantly higher stability and efficiency of these QLEDs. The differences in exciton quenching and carrier distribution between the FZnO-EOD and the ZnO-EOD are schematically illustrated in Figure 5.5 (e and f).

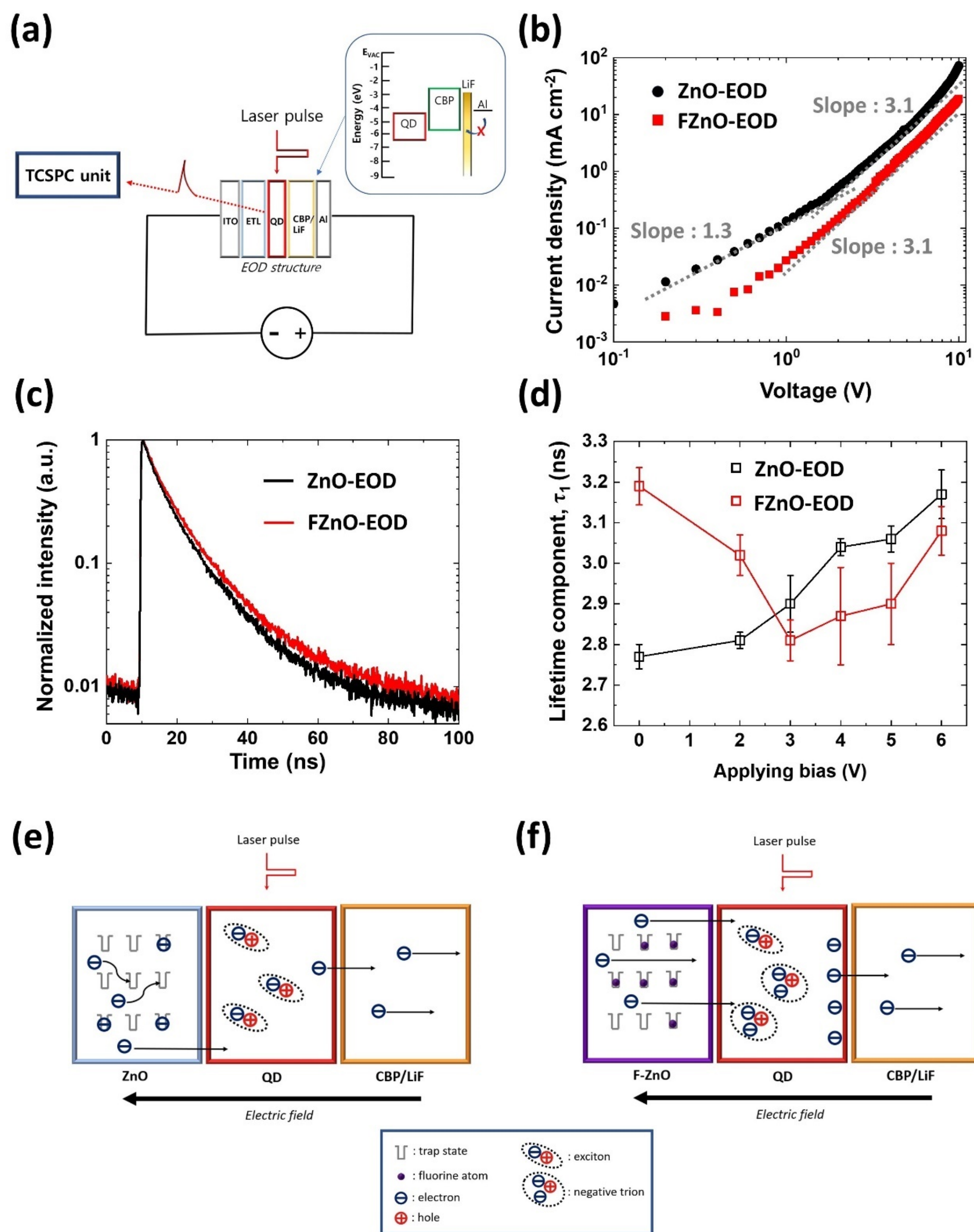
(a)
TCSPC unit
Laser pulse
ITO
ETL
QD
CBP/ LiF
Al
EOD structure
Energy (eV)
QD
CBP
LiF
Al
(b)
ZnO-EOD
FZnO-EOD
Slope : 3.1
Slope : 1.3
Slope : 3.1
Current density (mA cm-2)
Voltage (V)
(c)
ZnO-EOD
FZnO-EOD
Normalized intensity (a.u.)
Time (ns)
(d)
ZnO-EOD
FZnO-EOD
Lifetime component, τ1 (ns)
Applying bias (V)
(e)
Laser pulse
ZnO
QD
CBP/LiF
Electric field
(f)
Laser pulse
F-ZnO
QD
CBP/LiF
Electric field
: trap state
: fluorine atom
: electron
: hole
: exciton
: negative trion

Figure 5.5 (a) Schematic diagram of the EOD structure and the TRPL measurements scheme. The inset shows the energy levels of QDs/CBP/LiF/Al. (b) J-V characteristics of EODs with ZnO and FZnO. (c) TRPL signal from the QD layer in the EODs with ZnO and FZnO without bias. (d) The τ_1 values extracted from the TRPL signal under the different bias levels. The error bars indicate the standard deviation in the data collected from 6 samples in each group. Schematic images of exciton dynamics in EODs with (e) ZnO and (f) FZnO.

5.2.2 Probing Charge Accumulation and Annihilation within QLED during Device Operation

Capacitance-voltage-luminance (C-V-L) measurements can be helpful for probing charge accumulation and annihilation effects within QLEDs. It is therefore used to compare the C-V-L characteristics of the FZnO-QLEDs and ZnO-QLEDs to further elucidate the impact of the increased electron concentration in the QDs on the interaction with holes in the QDs and/or at the QDs/CBP interface. The C-V characteristics are analyzed with the equivalent circuit model shown in Figure 5.6 (a). The total capacitance across the QLED can be modeled as a set of individual capacitors connected in series, each representing one of the device layers, such that the total reciprocal capacitance of the devices is equal to the sum of each individual layer's reciprocal capacitance. The geometric capacitance of each layer is calculated by the thickness, cross-sectional area and dielectric constant of each layer using dielectric constant values of 10.5 for ZnO[177], 6.2 for QDs[178], and 3 for CBP[179]. Calculations give a total geometric capacitance of 1.23 nF which is comparable to the experimentally measured capacitance of 1.38 nF at voltages below V_{on} in both devices as can be shown in Figure 5.6 (b), indicating that charge injection from the contacts at these low voltages is negligible. Above V_{on}, the capacitance begins to increase pointing to charge injection and accumulation within the device stack, eventually reaching a peak. The slightly lower voltage for the onset of capacitance increase in case of the ZnO-QLED suggests that the presence of a larger number of oxygen vacancies facilitates electron injection from ITO into ZnO. Both QLEDs reach their peak

capacitance at around 3.8 V and have comparable peak capacitance values (1.95 nF and 2.0 nF for ZnO-QLED and FZnO-QLED, respectively) which is close to the geometric capacitance of CBP (1.8 nF) indicating that the electrons reach the QD/HTL interface to form a parallel plate capacitor-like distribution across the CBP layer at this voltage in both devices (The slightly higher peak capacitance of the FZnO-QLED might be due to the higher electron concentration at the QD/HTL interface of this device as was concluded earlier although the difference in capacitance is small and falls within the experimental error and therefore is understandably unreliable to serve as a verification). At biases exceeding 3.8 V the capacitance of both QLEDs decreases, indicating that charges are annihilated by the recombination process therefore leading to the dissipation of the electric double layer[8]. Interestingly, the capacitance decreases much faster with voltage in case of the FZnO-QLED pointing to a faster removal of electrons at the QDs/CBP interface. The C-V-L characteristics suggest that enriching the QDs/HTL interface with electrons facilitates a faster annihilation of charges at the interface. The ZnO-QLED, in contrast, exhibits a slower charge annihilation process.

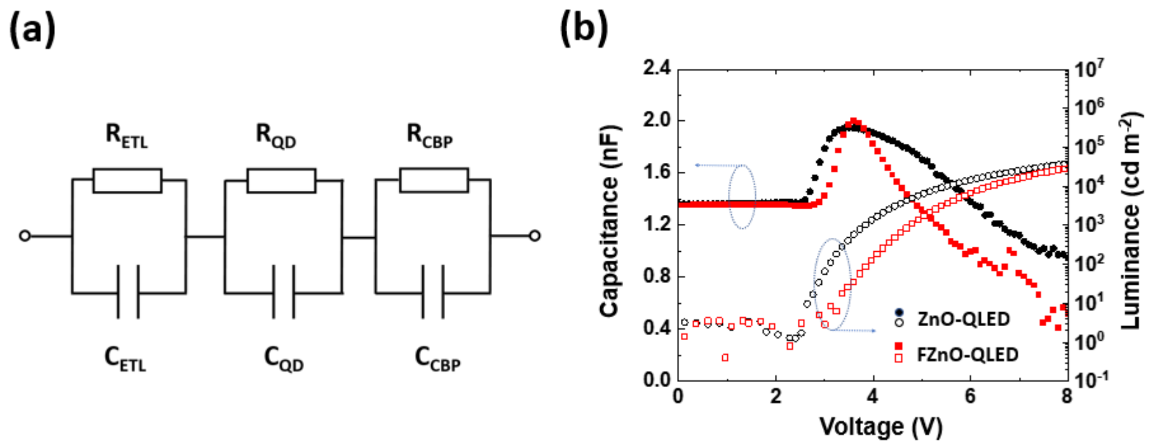

Figure 5.6 (a) The equivalent circuit model used for the C-V analysis. (b) C-V-L characteristics of the QLEDs.

5.2.3 Electron-hole Recombination at the QD EML/HTL Interface

The conclusion that there is a greater electron concentration within the QD EML in case of FZnO may seem at odds with the lower electron currents in the FZnO-EOD *vs.* the ZnO-EOD and is also somewhat counterintuitive from the perspective of charge balance in QLEDs considering that electron transport and injection into the QD is generally easier than that of holes. It should however be noted that conductivity in ZnO depends on two factors; the number of intrinsic carriers (electrons) and their mobility, both of which are affected by defect states but in opposite fashions. Therefore, although passivating defect states will reduce the number of electrons in ZnO, it can be expected to improve their mobility due to a reduction in scattering events by defects which may facilitate the arrival of electrons into the QD EML and at the QD/CBP interface. Increasing electron concentration in the QD EML can in turn help facilitate hole injection at the QD/HTL interface by Coulombic interactions[12,14,15], and thereby reduce the accumulation of holes at the interface due to the interdependence between the two injection processes. One should note that the lower current density at any given voltage in the J-V characteristics of the FZnO-device versus the ZnO-devices in Figure 4.4 (b) does not rule out the possibility that electron concentration in the QD EML of the earlier device may be higher, since the J-V characteristics could be more strongly governed by carrier concentrations in the ETLs (and where the electron concentration is significantly lower in case of FZnO than in case of ZnO) than by their concentrations in the EML especially also considering that the ETLs are somewhat thicker (40 nm *vs.* 30 nm). Therefore, to investigate if the FZnO ETL can indeed lead to a higher electron concentration in the QD EML or at the QD/HTL interface, the ETLs in QLEDs that contain a luminescent marking layer at the QD/HTL interface are compared. For this purpose, QLEDs containing a 5 nm thick luminescent marking layer made of CBP doped with 5% FIrpic are fabricated and tested. The structure of these devices is shown schematically in Figure 5.7 (a) and consists of: ITO/ETL/QDs/CBP (5nm)/ CBP:FIrpic (5 nm)/CBP (40 nm)/MoO_3/Al. FIrpic was selected due to its comparable energy structure to CBP which avoids major perturbation of charge distribution at QD/HTL but higher PLQY and thus

a more readily detectable luminescence from any exciton recombination within the HTL. Effectively, the marking layer probes changes in the e-h recombination zone due to changes in charge distribution in the device stacks due to the use of FZnO *vs.* ZnO ETLs. Figure 5.7 (b) shows the EL spectra obtained from these QLEDs as well as from ZnO-QLED without the FIrpic layer to serve as a reference. As can be seen, EL from FIrpic is observed in the two devices and is higher in case of the FZnO-QLED relative to the ZnO-QLED. The higher FIrpic EL emission points to increased e-h recombination within the HTL in case of the FZnO-QLED device which indicates that the electron concentration in the HTL must be higher indicating that their concentrations in the QD EML and at the QD/HTL interface must also be higher. One may expect the higher electron concentrations in the HTLs in case of the FZnO-QLED to possibly induce new degradation mechanisms, a phenomenon that may be behind the different values of the accelerator coefficients in the FZnO- *vs.* ZnO-device observed in Figure 4.5 (c). The mechanism of accumulated charge annihilation for these highly stable QLEDs is schematically depicted in Figure 5.7 (c and d).

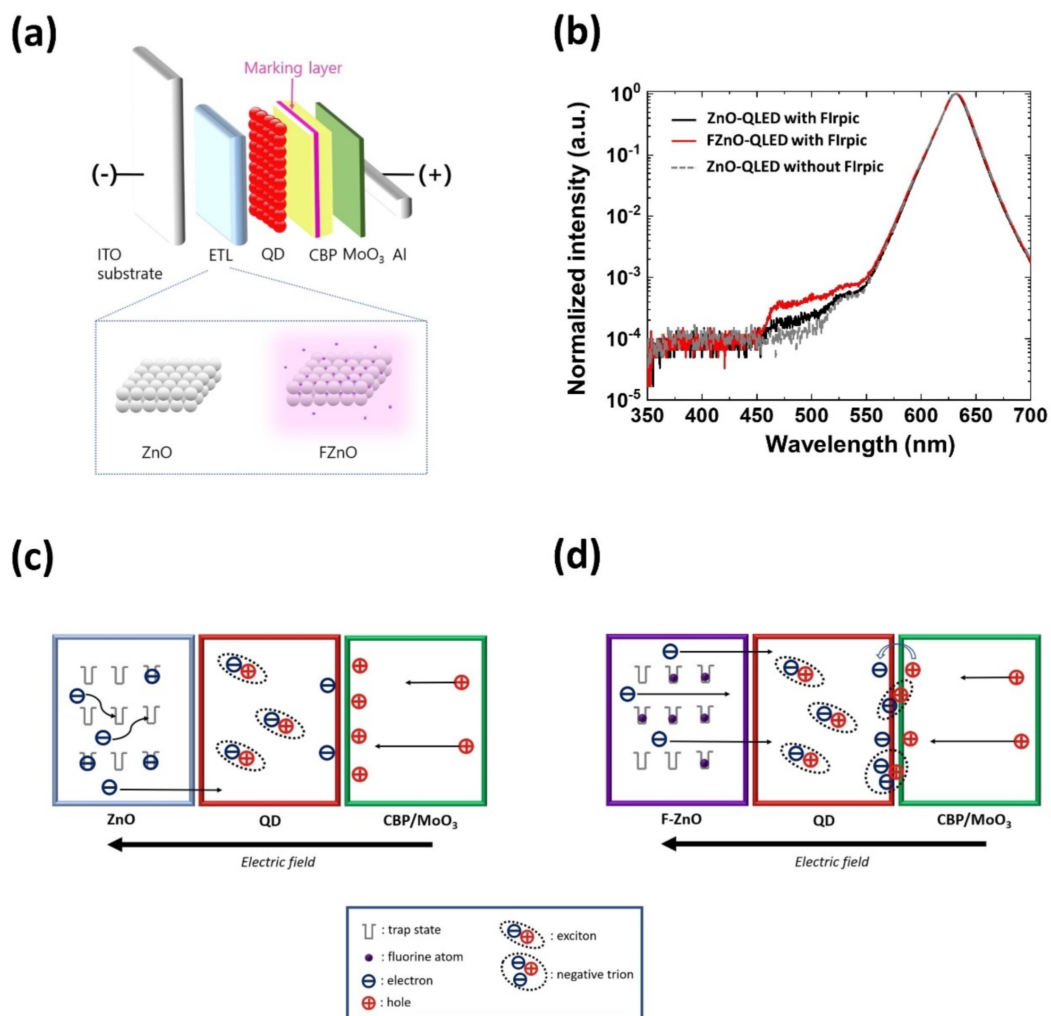

Figure 5.7 (a) Schematic diagram depicting the structure of the QLEDs with the FIrpic marking layer. (b) EL spectra from the same QLEDs under 20 mA cm^{-2}. A spectrum from a ZnO-QLED without the marking layer is also included for comparison. Schematic images of device operation in QLEDs with (c) ZnO and (d) FZnO.

5.3 Chapter Summary

In QLEDs, in general, due to the large energy barrier between the valence band maximum of Cd-based QDs and the highest occupied molecular orbital (HOMO) energy level of the HTL, holes accumulate on HTL molecules at the QDs/HTL interface. This accumulation of holes can lead to device degradation through a variety of processes. It is therefore quite possible that the increase in the number of electrons at QDs/HTL interface as a result of using ZnO:PEI and FZnO ETL results in a decrease in the number of hole that accumulate at the QDs/HTL interface, hence the device stability enhancement. This notion is also well supported by the observations from the marking layer devices that showed that using ZnO ETL modification approaches proposed here results in a more efficient e-h recombination at the interface evident in the stronger EL intensity from FIrpic marking layer. The results here therefore reveal and underscore the importance of properly managing charge concentrations at the QDs/HTL interface for QLED stability.

Chapter 6 Suppressing QLED Degradation via Reducing Positive Charges in the ZnO

This work has been published in DS Chung et al., Advanced Optical Materials, 2300686, 2023. It has been reproduced in part with permission from the publisher.

Seeing the significant effect of adding I_2 and $FeCl_3$ to the ZnO ETL on the EL stability behavior of the QLEDs as discussed in the Chapter 4 and the Section 4.2, the major factor for the EL stability improvement is investigated in this Chapter. The incorporating I_2 and $FeCl_3$ as halide dopants into ZnO ETL increases the LT50 of red QLEDs by 2.2× and 3.6×, respectively, demonstrating 124.3 hours and 206.1 hours instead of 56.9 hours in devices with undoped ZnO, all tested at 20 mA cm^{-2} and from an initial luminance of ~3,000 cd m^{-2}. In the sub-section 6.1.1, the charge transfer at the ZnO/QDs interface is investigated and compared it to the halide:ZnO/QDs interface. Moving on to the sub-section 6.1.2, the impact of halide dopants in ZnO on the changes in the L-J characteristics of the QLEDs by electrical aging is discussed. In the sub-section 6.1.3, XPS studies on the QLEDs is explored to reveal the role of the halide dopants in the changes in electronic state by electrical aging.

6.1 The Role of Halides in Nanostructures

6.1.1 Investigating Charge Transfer at ZnO/QDs Interface

Oxygen vacancies (V_o) in ZnO, the predominant type of intrinsic defects in these materials, produce a state with energy typically 1.16 eV above the valence band maximum of ZnO[74-76] (-6.3 eV, relative to vacuum level), placing them close to the highest occupied quantum-confined orbital level of CdSe/ZnS QDs (-6.2 eV, relative to vacuum level). These states can, therefore, act as hole traps promoting spontaneous charge transfer at the ZnO/QDs interface and resulting in a population of holes trapped on these defects in the ZnO. The presence of such charged defect states can reduce the efficiency of the radiative relaxation pathway of excitons on QDs[180]. Seeing that adding I_2 and $FeCl_3$ in the ZnO ETL increases EL

lifetime, their effect on the photoluminescence (PL) characteristics of the QDs is investigated. Figure 6.1 (a) shows PL spectra collected from QD films coated on ZnO, I_2:ZnO, and $FeCl_3$:ZnO films. All peak heights are normalized to the height of the PL spectrum collected from the QDs coated on the undoped ZnO. As seen, the QDs coated on the I_2:ZnO or the $FeCl_3$:ZnO exhibit ~ 10 % higher PL intensity than that on the ZnO. While the increase in PL clearly shows that the presence of dopants in ZnO helps reduce exciton quenching, such increase is smaller than that observed in a previous work where the ZnO was doped with fluorine[45] which suggests that, unlike F_2, doping with I_2 and $FeCl_3$ does not completely passivate the V_o states. This may perhaps be due to the relatively large atomic radii of iodine, chlorine, and iron atoms when compared to oxygen, which reduces their ability to occupy and fill oxygen vacancies. The limited V_o passivation effect of I_2 and $FeCl_3$ suggests that their role in improving the EL stability is due to a different mechanism, possibly associated with influencing or reducing interfacial charge transfer or their (i.e., the charges) trapping on these defects. In order to study possible changes in charge transfer at the ETL/QD interfaces due to the use of the dopants, and, at the same time avoid these effects becoming confounded by the flow of current, the layers are studied in metal-insulator-semiconductor (MIS)-type devices, of structures as schematically depicted in Figure 6.1 (b). In these devices the ETLs and QDs are coated on ITO-coated substrates in the same fashion as in the QLEDs and then a layer of polymethylmethacrylate (PMMA) is coated in-between the QD layer and the Al counter electrode in order to prevent current flow and charge injection from the electrode when bias is applied. In order to optically excite the QDs without producing a significant population of photo-generated carriers in the ETLs, 550 nm wavelength illumination is used for excitation. This wavelength can be absorbed by the QDs but is longer than the absorption edge of ZnO (3.46 eV, as extracted from the Tauc plots in Figure S6.1). Figure 6.1 (c) shows the intensity of the PL collected from the QDs in the MIS devices over time under continuous illumination, normalized to the initial intensity. As can be seen, the PL intensity decreases by ~5 % within 10 minutes of illumination in case of the ZnO-ETL MIS but decreases much less, if any, in the other two devices. Notably also, the decrease in the PL intensity from the ZnO MIS gradually

subsides and plateaus after about 15 minutes. We then test the effect of applying 4V bias (both forward (FWD) and reverse (REV), where the bias directions are as described in Figure 6.1 (b) with forward bias corresponding to ITO being held at a more negative potential relative to the Al electrodes) on the PL intensity. Figure 6.1 (d-f) show the PL intensity versus time collected from the MIS-devices under bias. In these Figures, time 0 on the x-axis corresponds to the moment the bias is applied, which is approximately 30 minutes after the illumination begins (and exceeds the time for the PL intensity decrease in case of the ZnO MIS observed in Figure 6.1 (c) to subside and plateau). As seen, all devices show an instantaneous PL drop when the bias is applied. Such sudden drop in PL can in general be attributed to : (i) electric field-induced exciton dissociation, and/or (ii) Auger quenching due to the presence of charges that accumulate in the QD layer and/or at the ETL/QDs as a result of the transient charge injection in the MIS when the bias is applied. One notable observation is that the magnitude of QD PL intensity drop in case of the ZnO-device exhibits a strong dependence on the bias polarity, dropping by 11 % for forward bias and 32 % for reverse bias (seen in Figure 6.1 (d)). No such significant polarity dependence is observed in the other two devices, with the I_2:ZnO-device exhibiting a PL drop of ~35 % PL for both FWD and REV biases (in Figure 6.1 (e)), and the $FeCl_3$:ZnO-device exhibiting a PL drop of both ~15 % for FWD and REV biases, respectively (Figure 6.1 (f)). The different responses of the PL intensity to the bias and its polarity among the devices suggests that charging (and subsequent Auger quenching) is playing a role in these effects since one would expect electric field induced quenching effects to be similar in all devices. This is also in consideration of the very similar J-V characteristics of the ZnO-, I_2:ZnO-, and $FeCl_3$:ZnO-QLEDs (presented in Figure 4.6 (b)) which indicates that the conductivity in the three ETLs must be similar, suggesting that electric field distribution, and hence any PL quenching due to electric field-induced exciton dissociation, cannot be very dissimilar among the devices. In this context, the gradual decrease in QD PL observed in case of the ZnO MIS before the bias is applied (Figure 6.1 (c)) can be the result of exciton dissociation as a result of efficient transfer of photo-generated holes from the QD layer to the ZnO layer, i.e., interfacial charge transfer, where they will preferentially reside on V_o states

because of their favorable energy. The presence of such positively charged states in the ZnO could lead to QD PL quenching observed in the ~ 5 % lower PL intensity observed in case of the ZnO MIS in the longer term. When forward bias is applied and electrons are temporarily injected from the ITO into the ZnO, some of these holes will be annihilated by e-h recombination. Since a reverse bias would not similarly help reduce the positively charged states in ZnO, the magnitude of the PL drop under reverse and forward bias is different. In contrast, the similar PL drop produced by the reverse and forward in the other two devices suggests that the effect is primarily due to electric field-induced exciton dissociation and that charging does not play a significant role, suggesting that the presence of halides in ZnO may prevent interfacial charge transfer at the ZnO/QDs interface and the accumulation of positive charges in the V_o states.

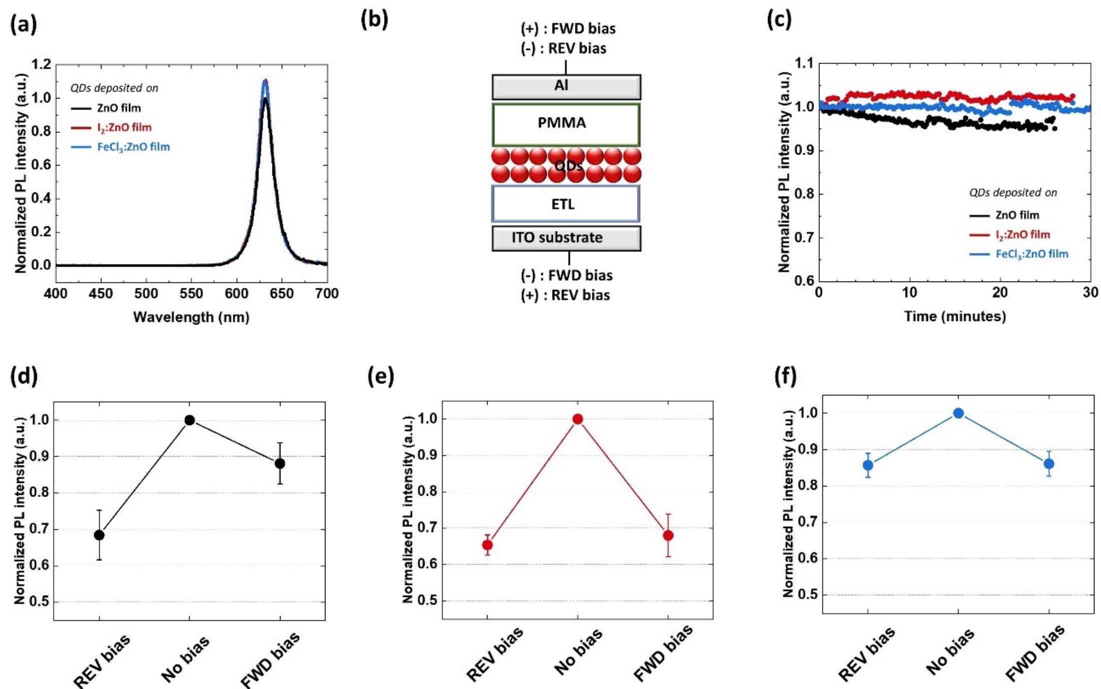

Figure 6.1 (a) PL spectra of QDs deposited on ZnO, I_2:ZnO, and $FeCl_3$:ZnO. The PL peak heights are normalized to the height of the peak of the ZnO sample (b) A schematic diagram of the structure of the

MIS-device and the polarities for forward and reverse bias. (c) QD PL intensity changes over time with ZnO, I_2:ZnO, and $FeCl_3$:ZnO without bias. QD PL intensity without bias and with FWD and REV bias with (d) ZnO, (e) I_2:ZnO, and (f) $FeCl_3$:ZnO. In each case, the QD PL intensities for FWD and REV bias are normalized to the PL intensity at no bias.

6.1.2 Changes in Electroluminescent Characteristics over QLED Aging

Seeing the significant effect of adding I_2 and $FeCl_3$ to the ZnO ETL on the EL stability behavior of the QLEDs, especially in the first 30 hours of electrical stress, changes in the J-V-L characteristics of the devices with aging are studied. Figure 6.2 (a-c) show the J-V-L characteristics before (fresh) and after electrical aging under 20 mA cm^{-2} constant current driving for 20 hours and after reaching LT50s (which corresponds to 100 hours, 120 hours, and 250 hours for the ZnO-QLED, I_2:ZnO-QLED, and $FeCl_3$:ZnO-QLED, respectively). As can be seen in Figure 6.2 (a), the sub-threshold current (current below 2.2 V) as well as the current at high voltages (> 3 V) both increase after 20 hours of electrical stress in case of the ZnO-QLED. The J-V characteristics, however, hardly change after further electrical aging for 100 hours. These changes in the J-V characteristics are consistent with the increase in charge conduction observed in Figure 4.7 (c) and confirm that the underlying changes occur primarily only within the first 20 hours of electrical stress. The L-V characteristics also show changes after the electrical aging, consistent with the decrease in the EL over time observed in Figure 4.7 (b). The changes in the J-V-L characteristics of the I_2:ZnO- and the $FeCl_3$:ZnO-QLEDs by aging however differ from the case of the ZnO-QLED, as shown in Figure 6.2 (b) and (c), respectively. In these devices, the increase in the sub-threshold current after electrical aging is much less (hardly detectable in case of the $FeCl_3$:ZnO-QLED). Also, in contrast to the ZnO-QLED where the J-V characteristics do not change appreciably after the first 20 hours, here we observe an increase in current in the high voltage range (i.e., > 3V) take place in the longer term. Since the main differences between the stability behavior among the devices seem to stem primarily from the differences in the rate of EL loss in the short term (i.e., < 30 hours) as opposed to the long term (from Figure 4.7 (d)), we give more attention here to the changes

observed after the first 20 hours of electrical stress, which are primarily changes in the sub-threshold currents. In general, sub-threshold currents correspond to unipolar transport across the QD layer (because they occur at voltages below the onset of electroluminescence) and therefore are dominated by leakage currents of either electrons to the HTL or holes to the ETL. An increase in the sub-threshold current could therefore be due to increased leakage of electrons to the HTL, however, if this is the case, a noticeable emission band in the 350 to 450 nm range, corresponding to emission from CBP that would result from e-h recombination in the HTL would be observed, which is not the case. Barring that, the sub-threshold current at these low electric fields can then be attributed to hole leakage and subsequent trap state-mediated e-h recombination in the ETL as explained in equation (4.1 to 4.3), in which case the observed increase in sub-threshold currents could be due to an increase in trap density in the ZnO ETL. Figure 6.2 (d-f) show the L-J characteristics of the devices on a log-log scale. Considering the power law dependence of LEDs described by[181]

$$L \propto J^n \tag{6.1}$$

one can see that while the characteristics are generally linear (i.e., with a slope corresponding to $n = 1$), they somewhat deviate from linearity at low currents, exhibiting an $n > 1$, and that the value of increases further after aging at these low currents for all devices, with n becoming ~ 1.3, ~1.15 and ~1.17 for the ZnO-QLED, I_2:ZnO-QLED and $FeCl_3$:ZnO-QLED, respectively, after the devices are aged to LT50. Since the deviation from linearity at low currents arises primarily from an increase in shunt currents[14,181] that cause the EL to decrease disproportionately faster than the corresponding decrease in current, the increase in the value of n after electrical aging points to a deterioration in carrier confinement in the QD EML and an increase in the fraction of charges (i.e., holes) that escape to the ETL without recombination.

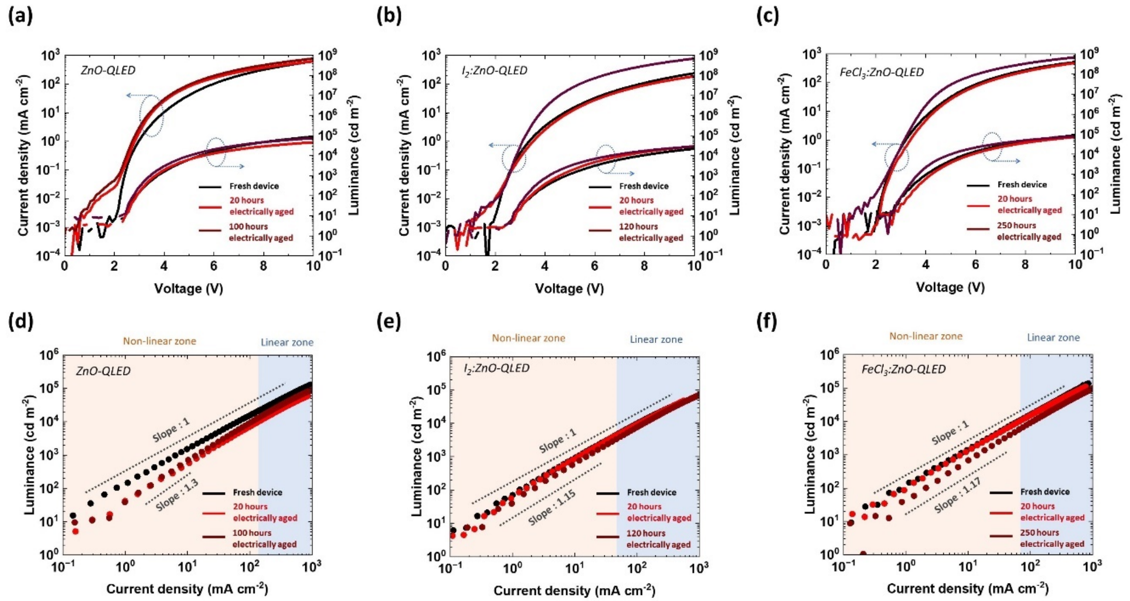

Figure 6.2 J-V-L characteristics before (fresh), after electrical aging under 20 mA cm^{-2} constant current driving for 20 hours, and after reaching LT50s of the QLEDs with (a) ZnO, (b) I_2:ZnO, and (c) $FeCl_3$:ZnO. (d-f) The same J-V-L characteristics presented on log-log scales.

6.1.3 Reducing Formation of Positively Charged ZnO Species by Halides

Seeing that doping ZnO with I_2 and $FeCl_3$ can have an influence on interfacial charge transfer between ZnO and QDs without necessarily filling the V_o states, their effects on the electronic structure of QD EML and ZnO ETL are investigated in order to understand their role in improving the EL stability of the devices. Under normal bias conditions (i.e., with ITO at a more negative potential relative to the Al as is usually the case during device operation), when electrons are injected into the ZnO, one can expect interactions between electrons and the I_2 and $FeCl_3$ to produce halide negative ions through reduction process of the following general schemes:

$$I_2 + 2e^- \rightarrow 2I^-$$

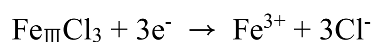

$$Fe_{III}Cl_3 + 3e^- \rightarrow Fe^{3+} + 3Cl^-$$

The hysteresis in the J-V-Ls of the I_2:ZnO- and $FeCl_3$:ZnO-QLEDs in Figure 6.3 may be evidence for the presence of such ionic species. As seen, the devices with doped ZnO show some hysteresis. The hysteresis suggests the presence of ionic species that is capable of migrating (i.e., on off-lattice sites) under the influence of the electric field[182]. The bias would cause the negative halide ions (anions) to gradually migrate towards the ETL/QD EML. With a large number of these negative ions (anions) at the interface, one can expect them to act as efficient scavengers[162,183,184] for any holes that may escape the QD EML and reach the ETL thereby reducing the number of holes that may get trapped on ZnO defect sites (i.e., V_o states). Instead, as negatively charged scavengers, they may facilitate the neutralization and annihilation of these holes[185]. It should be noted that while the presence of cationic iron species has been reported to influence the radiative transition in Cd-based QDs, their effect is usually observed only at extremely low temperatures which may explain their negligible effect on QLED efficiency at room temperature[186].

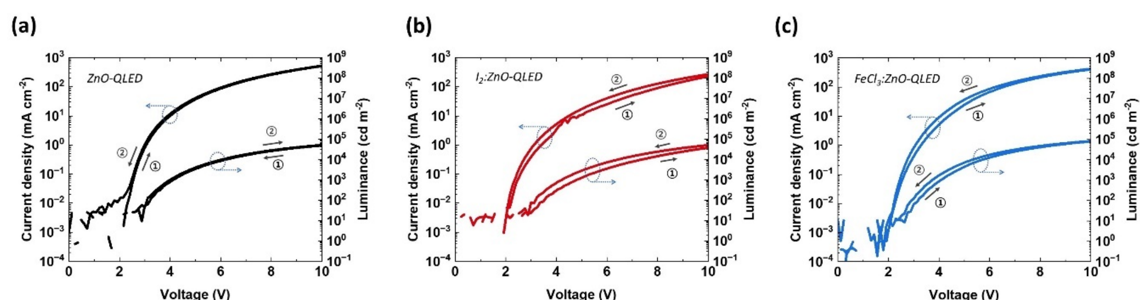

Figure 6.3 J-V-L characteristics measured under two sweep directions (i.e., 0 V to 10 V and 10 V to 0 V) of QLEDs with (a) ZnO, (b) I_2:ZnO, and (c) $FeCl_3$:ZnO, with the second sweep starting immediately following the first sweep.

In order to test if adding these dopants at these low concentrations may indeed alter charge concentrations in the ZnO and other device layer, we use device simulation to compare charge concentrations in the doped and undoped ZnO-QLEDs. In these simulations, SCAPS (version 3.3.10) simulation tool[187] is used to investigate the effects of introducing I_2 and $FeCl_3$ as dopants in the ZnO ETL at concentrations of between 0.1 and 0.3 mg mL^{-1}, which corresponds to a dopant molar density of 2 to 9×10^{17} cm^{-3}, on charge distribution across the device. Electron donor (hole acceptor) type defects are introduced into ZnO ETL, which mimics the hole scavenging effect of the dopants in ZnO ETL. The defect density is assumed to be equal to the molar concentrations of the dopants in the ZnO. The energy level of the donor is assumed to be comparable to the hole trapping energy of the oxygen vacancies, 1.2 eV above valence band maximum of ZnO[76]. All the donors are assumed to be fully ionized. Table S6.1 (a) shows simulation parameters of each layer and (b) shows parameters of the donor defect states. The bias condition used in this simulation is lower than that in the actual devices due to simulation limitation, which may lead to deviation between simulations and experimental conditions[98,188]. Nonetheless, the used bias condition exceeds the flat band condition of layers, and thus represents conditions of charge injection from both contacts. Figure 6.4 (a) shows electron and hole density across the various layers of the QLED for different doping concentration in the ZnO ETL. As seen in Figure 6.4 (b), the presence of the dopants at these concentrations can lead to a reduction in the density of holes in the ZnO ETLs by almost two orders of magnitude.

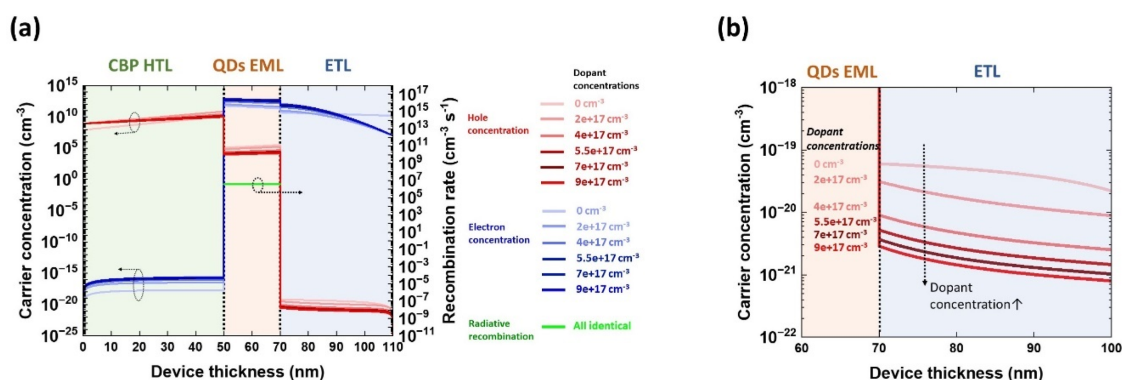

Figure 6.4 (a) Simulation result showing charge distribution and radiative recombination rate in QLEDs with different dopant concentrations. (b) The hole concentration in ETL with different dopant concentrations.

XPS depth-profile measurements on fresh- and electrically aged-QLEDs with ZnO, I_2:ZnO, and $FeCl_3$:ZnO ETLs are performed in order to probe possible changes in chemical and electronic states in the QDs and ETLs due to the presence of the dopants. The electrically aged devices are aged under 20 mA cm^{-2} constant current flow for 20 hours. The Al electrodes are then peeled-off using scotch-tape in order to allow probing the underlying layers by XPS, as schematically depicted in Figure 6.6 (a). Ar sputtering is used for etching the layers in order to obtain XPS scans at different depths down the device stacks.

In XPS, while the majority of the ejected photoelectrons are generated from within the top 10 nm from the surface of the layer, a significant fraction of them (i.e., the photoelectrons) can originate from greater depth[189]. This is especially true for disordered and low-density materials, like in case of the organic and colloidal QD materials used in the HTLs and EMLs of the QLEDs, where a larger number of photoelectrons from greater depths can escape the solid and reach the detector which reduces the depth resolution of the measurements. (The limited depth resolution can be seen, for example, in Figure 6.5 (a) and (b), where a significant

signal from Zn 2p and Cd 3d core level electrons can be detected from the sample surface even before any sputtering is done). This makes it difficult to determine – from looking at a spectrum collected after a certain period of sputtering – the depth or layer that the spectrum corresponds to or if a certain interface in the sample has been reached. Therefore, to circumvent this limitation, we measure changes in the signal from the Zn 2p, Cd 3d and In 3d core level electrons at all sputtering times, and use the results to construct "calibration curves" that correlate the sputter time with depth. These curves are presented in Figure 6.5 (a and b). Given the clear inflection points in the Cd 3d intensity in Figure 6.5 (b), we can conclude with a high level of confidence that spectra collected between 100 s and 200 s of sputtering correspond to the QDs and those collected between 200s and 500s of sputtering correspond to the ETLs, with the ITO substrate being reached after 500s of sputtering. We should note that all the spectra in this experiment are charge-corrected by shifting their positions with respect to the C-C bond peak binding energy in C 1s spectra (shown in Figure 6.5 (d-i)) taken to be 284.8 eV[190]. We also note the relatively higher binding energies of Zn 2p electrons measured here in comparison to previous reports. The higher value may be due to charging effects from Ar ions. Considering that all QLED samples are measured under the same conditions and using the same sputtering cycles, the measured higher binding energy does not affect the comparisons among the devices.

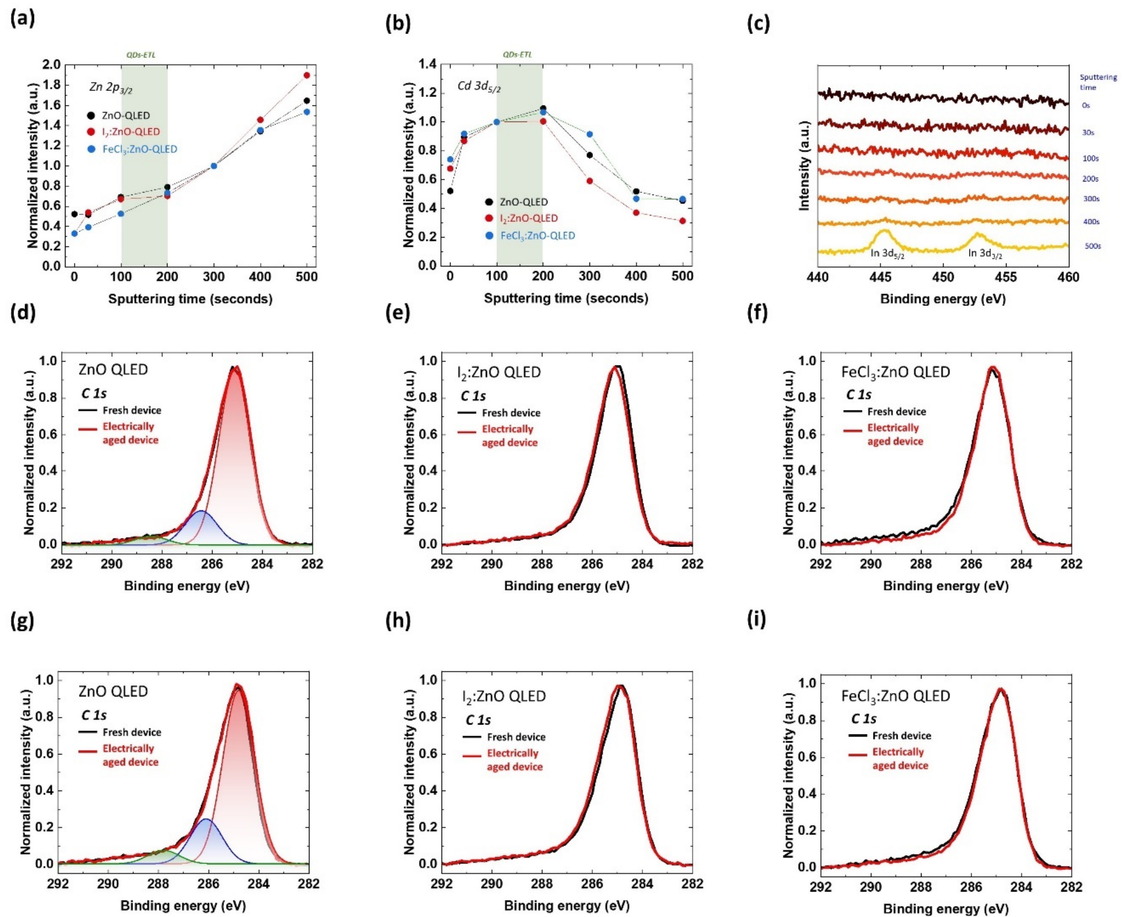

Figure 6.5 Normalized peak intensity of (a) Zn $2p_{3/2}$ and (b) Cd $3d_{5/2}$ XPS spectra for calibration curves. (c) XPS spectra of In 3d core level electrons from 0 s to 500 s sputtering time. XPS spectra of C 1s core level electrons in fresh- and electrically aged-QLEDs measured after 100 s and 300 s sputtering time with (d and g) ZnO, (e and h) I_2:ZnO, and (f and i) $FeCl_3$:ZnO.

Figure 6.6 (b-d) and (e-g) show the XPS spectra of Cd $3d_{5/2}$ core level electrons collected from the fresh- and electrically aged-QLEDs, respectively, collected after 100 s of sputtering. Since the shapes of the spectra do not correspond to Gaussian functions, Gaussian

peak function fitting is used to deconvolute the spectra into their constituent Gaussian bands. In case of the fresh QLEDs, the Cd $3d_{5/2}$ core level electrons spectra consist of two bands with maxima at 405.5 eV and 406.2 eV. The 405.5 eV band can be attributed to Cd in CdSe, whereas the 406.2 eV band, which has a lower intensity, can be ascribed to a higher oxidation state of Cd[191]. In the electrically aged-QLEDs, as can be shown in Figure 6.6 (e-g), the shapes of these spectra are somewhat different and their peak positions are shifted to higher binding energy, by ~ 0.2 eV for the ZnO-QLEDs and by > 0.1 eV (but less than 0.2 eV) for the devices with the doped ETLs. A shift in the binding energy of the electrons to higher values may point to positive charging in the samples after aging, and is higher in case of ZnO-QLED than in the I_2:ZnO-QLED or $FeCl_3$:ZnO-QLED. Also notably, the relative height of the 406.2 eV band becomes higher in all aged devices, pointing to an increase in oxidized Cd. While the exact mechanism behind the increase in oxidized Cd during electrical aging is unclear, it may have to do with the presence of holes in the QD EML during device operation which can lead to the formation of unstable QD cationic states; the latter recently found to play a role in device degradation in the long term according to several reports[44,192].

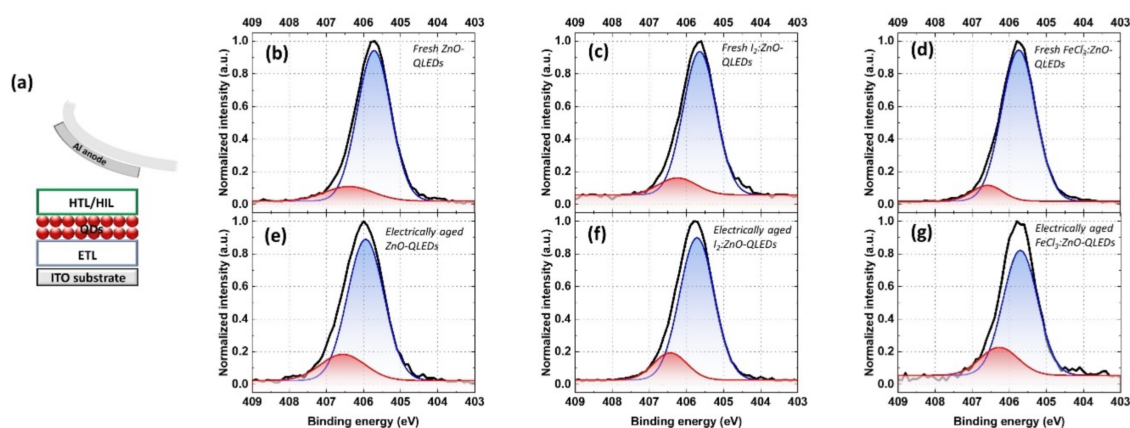

Figure 6.6 (a) Schematic diagram of the QLED sample used for the XPS measurements showing the removal of the Al electrode by scotch tape after device aging has been completed in order to allow testing the underlying layers by XPS. XPS spectra of Cd $3d_{5/2}$ core level electrons in fresh QLEDs with

(b) ZnO, (c) I_2:ZnO, and (d) $FeCl_3$:ZnO and in electrically aged QLEDs with (e) ZnO, (f) I_2:ZnO, and (g) $FeCl_3$:ZnO.

While the presence of oxidized Cd species in QD EML could be involved in device degradation, the fact that all three devices – regardless of the differences in their ETLs or LT50 values – exhibit similar changes in their Cd spectra indicates that an additional mechanism is affecting the stability behavior of the devices and its improvement by the halide dopants in the ETLs. We therefore study the XPS spectra of Zn $2p_{3/2}$ core level electrons collected after 300s of sputtering, and thus from the ETLs, in the fresh and aged QLEDs. Figure 6.7 (a-c) show the spectra collected from the fresh-QLEDs with (a) ZnO, (b) I_2:ZnO, and (c) $FeCl_3$:ZnO. As seen, all the spectra can be deconvoluted into two Gaussian bands with slightly varying peak binding energies among the QLEDs; 1022.5 eV and 1023.9 eV for ZnO-QLED, 1022.6 eV and 1024 eV for I_2:ZnO-QLED, and 1022.8 eV and 1024.2 eV for $FeCl_3$:ZnO. The 0.1~ 0.3 eV higher energy in the I_2:ZnO and the $FeCl_3$:ZnO relative the ZnO can be ascribed to the high electronegativity of halogens[45,149], which indicates that the presence of the halides in ZnO (see also Figure 6.7 (g) and (h)) affects its electronic structure. In all these spectra, the lower energy bands correspond to Zn in ZnO lattice, whereas the higher energy bands can be ascribed to Zn species in higher oxidation states[193-196]. Remarkably, as can be seen in Figure 6.7 (d-f), these higher energy bands change after electrical aging, but to significantly varying extents among the devices. In case of the ZnO-QLED device, the height of this band significantly increases. In contrast, in the I_2:ZnO-QLED, the height of this band increases but to a much lesser extent, whereas in case of the $FeCl_3$:ZnO-QLED, its intensity hardly changes. The results clearly show that electrical aging leads to a significant increase in Zn species in higher oxidative states (i.e., higher cationic states), and that the use of dopants helps suppress the formation of this species, with $FeCl_3$ being more effective than I_2 in that regard. Figure 6.7 (i) shows the areal ratio of the higher energy band to the lower energy band before and after aging in each case. The areal ratio increases by 40.6%, 14.9%, and 1.0% in the QLEDs with ZnO, I_2:ZnO, and $FeCl_3$:ZnO, respectively, after aging. The Figure also shows the rate of EL loss in the first 20 hours of

electrical aging of the corresponding devices (i.e., ΔL in the first 20 hours of electrical stress from the data in Figure 4.7 (a) divided by 20 hours, where 20 hours are selected here because it corresponds to the electrical aging time of the XPS samples). One can see a clear negative correlation between the extent of the areal ratio increase after electrical aging and the rate of EL loss in the devices, with devices exhibiting the largest increase in the height of the Zn higher cationic states also exhibiting the fastest EL degradation. The incorporation of halide ions in nanocrystals is known to produce shallow states, providing more favorable sites for holes[159,197,198]. Therefore, we believe that the larger suppression of Zn higher cationic states formation by the I_2 and $FeCl_3$, and especially the latter, to their shallower energy states, thereby providing more favorable energy states for holes escaping from QD EML to be trapped on them instead of holes residing on Zn sites where they would form the Zn cations. These results suggest that doping by halides influences the accumulation of holes in the ETL during device operation and suppresses the oxidation process, leading to EL lifetime enhancement.

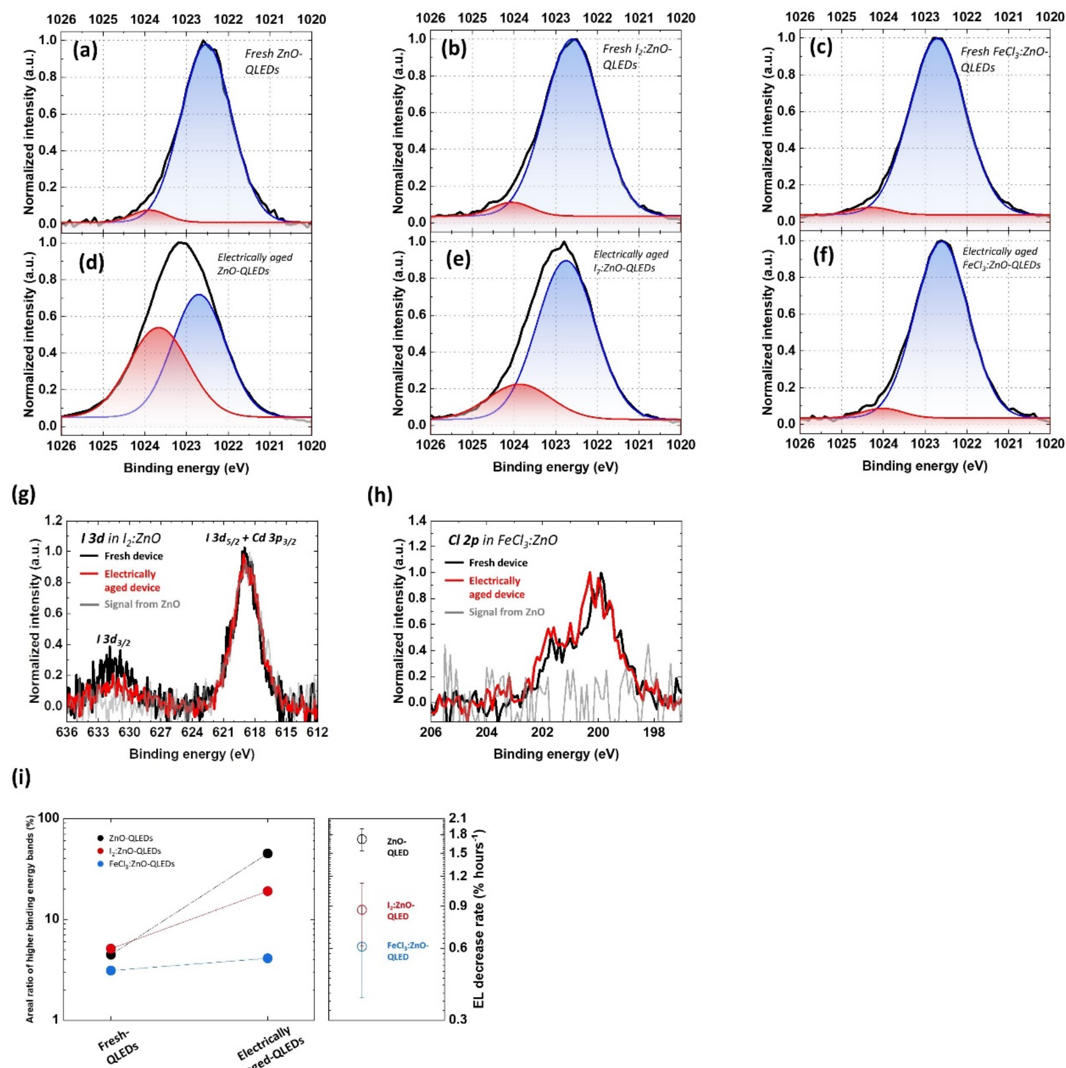

Figure 6.7 XPS spectra of Zn $2p_{3/2}$ core level electrons in fresh QLEDs with (a) ZnO, (b) I_2:ZnO, and (c) $FeCl_3$:ZnO and in electrically aged QLEDs with (d) ZnO, (e) I_2:ZnO, and (f) $FeCl_3$:ZnO. XPS spectra of (g) I 3d collected from I_2:ZnO-QLEDs, and (h) Cl 2p in QLEDs with $FeCl_3$:ZnO. The signals collected from ZnO-QLEDs are displayed for comparisons. All the XPS spectra are measured after 300 s sputtering time. (i) Areal ratio changes of higher oxidation state bands in XPS Zn $2p_{3/2}$ spectra between

fresh- and electrically aged-QLEDs with the EL decrease rate within 20 hours of the QLEDs. The rate of EL loss in the first 20 hours of each QLED is also presented.

Seeing the effect of electrical aging on the electronic states of Zn and its dependence on doping, we similarly investigate the effect of the aging on the O states. Figure 6.8 (a) shows the XPS spectra of the O 1s core level electrons collected after 300 s of sputtering, and thus from the ETLs, from the fresh ZnO-, I_2:ZnO-, and $FeCl_3$:ZnO-QLEDs. As seen, the shapes and peak positions of all spectra are essentially the same regardless of the ETL doping. The spectra can be deconvoluted into three bands[148]. The lowest energy band (O_i, at 531.6 eV) can be ascribed to lattice oxygen, whereas the middle (O_{ii}, at 532.7 eV) and the highest energy bands (O_{iii}, at 533.7 eV) correspond to electronic states associated with oxygen vacancies and hydroxyl groups, respectively. Notably, the relative height of the O_{ii} to the other two bands is essentially the same in all cases. This is different from what is usually observed when dopants with similar or smaller atomic radii in comparison to oxygen are used where the intensity of the O_{ii} band usually decreases[199-201]. This result supports the notion that the I_2 and $FeCl_3$ ions do not fill the V_o vacancies, and, therefore, that the increase in EL lifetime observed in this work is not mainly due to the filling of the V_o states by the dopants. Figure 6.8 (b-d) compare the spectra in the fresh- and electrically aged-QLEDs for each ETL case. As can be seen in Figure 7b, the peak position of the O 1s spectrum shows a 0.4 shift towards higher binding energy in the ZnO-QLED case after aging. Such shift again suggests the presence of positive charges in the ZnO after aging. In contrast, no similar shift is observed in the I_2:ZnO-QLED or the $FeCl_3$:ZnO-QLEDs (Figures 6.8 (c) and (d) respectively) again indicating that the presence of the halide dopants reduces the accumulation of positive charges in the ZnO ETL. The mechanism is schematically illustrated in Figure 6.8 (e).

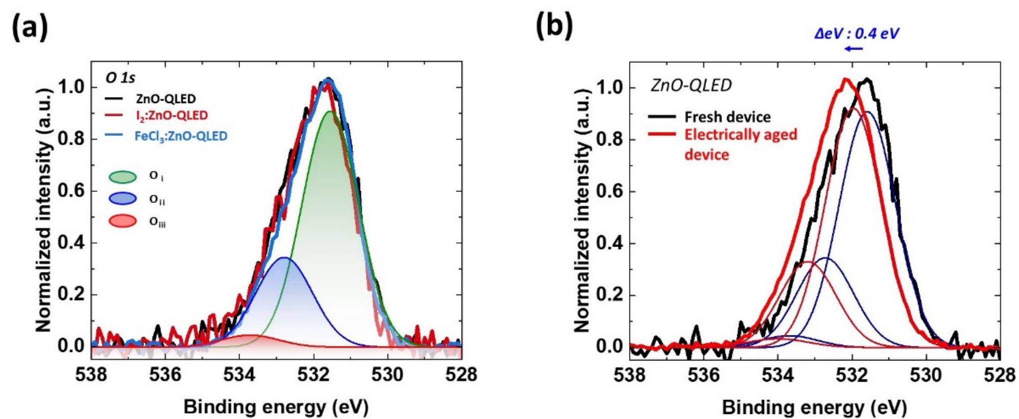

(a)
O 1s
ZnO-QLED
I_2:ZnO-QLED
$FeCl_3$:ZnO-QLED
O_I
O_{II}
O_{III}
Normalized intensity (a.u.)
Binding energy (eV)
(b)
ΔeV : 0.4 eV
ZnO-QLED
Fresh device
Electrically aged device
Normalized intensity (a.u.)
Binding energy (eV)

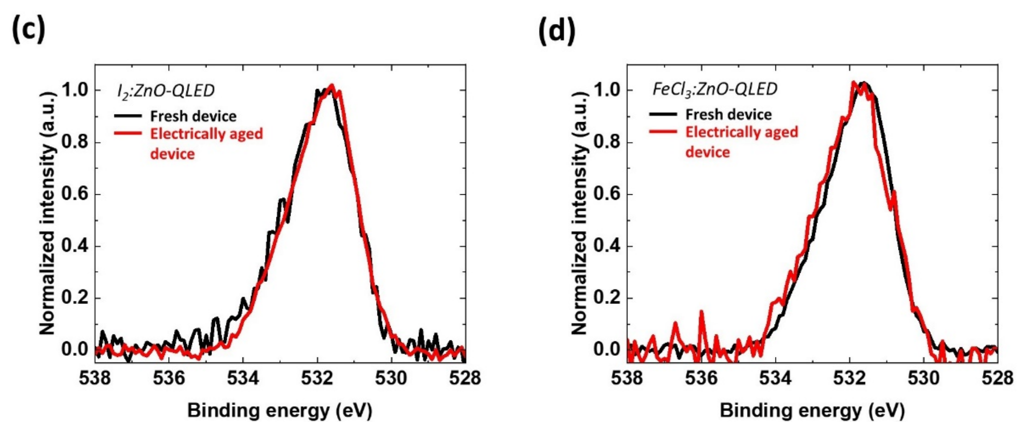

(c)
I_2:ZnO-QLED
Fresh device
Electrically aged device
Normalized intensity (a.u.)
Binding energy (eV)
(d)
$FeCl_3$:ZnO-QLED
Fresh device
Electrically aged device
Normalized intensity (a.u.)
Binding energy (eV)

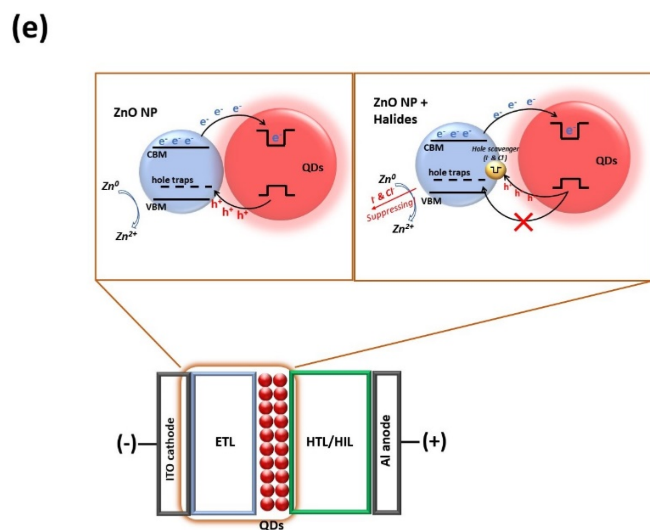

(e)
ZnO NP
CBM
hole traps
VBM
QDs
Zn^0
Zn^{2+}
ZnO NP + Halides
Hole scavenger
Suppressing
(-)
ITO cathode
ETL
QDs
HTL/HIL
Al anode
(+)

Figure 6.8 (a) XPS spectra of O 1s core level electrons from the QLEDs with different ETLs. XPS spectra comparison of fresh- and electrically aged-QLEDs with (b) ZnO, (c) I_2:ZnO, and (d) $FeCl_3$:ZnO. (e) Schematic illustration of the effect of halides on the accumulation of holes in the ETL during device operation.

6.2 Chapter Summary

In this work, the effect of adding I_2 and $FeCl_3$ to ZnO ETL on QLED stability is investigated. By incorporating I_2 and $FeCl_3$ as halide dopants into ZnO ETL, the LT50 of red QLEDs increases by 2.2× and 3.6×, respectively, demonstrating 124.3 hours and 206.1 hours instead of only 56.9 hours in devices with undoped ZnO, all tested at 20 mA cm^{-2} and from an initial luminance of ~3,000 cd m^{-2}. Results show the LT50 enhancement is primarily due to changes in the EL loss rate in the early stages of the electrical aging behavior of the devices (in the first 50 hours of electrical aging). An analysis of changes in the L-J characteristics of the devices by electrical aging reveals that the fast initial EL loss is associated with an increase in trap density in the ZnO ETLs as well as in the number of holes that leak to the ETL, both of which are reduced by the use of the halide dopants. PL measurements show that interfacial charge transfer at the ZnO/QDs interface occurs, leading to the formation of positively charged defect states (likely oxygen vacancies) in ZnO, subsequently leading to luminance quenching. The measurements also show that using the halide dopants reduces this interfacial charge transfer possibly due to their role in acting as hole scavengers that trap and efficiently neutralize holes in ZnO. XPS studies show that electrical aging of QLEDs leads to an increase in the concentration of ZnO species with higher oxidative states and that a correlation between the magnitude of EL loss and the concentration of these species exists. The studies also show that using the halide dopants significantly reduces the formation of these species as well as positive charging in the ETL during electrical stress. Our findings underscore the significant role that managing positive charges in ZnO plays in EL lifetime and provide an effective strategy for achieving highly stable QLED.

Chapter 7 Investigating the Effect of Halide Treatment on ETL in Green- and Blue-QLED Performance

This work has been published in DS Chung et al., Advanced Optical Materials, 2300686, 2023. It has been reproduced in part with permission from the publisher.

While the investigations have primarily focused on the red QLED, it naturally becomes interesting to test the effect of the dopants in the QLEDs of other colors. In this Chapter, we therefore also investigate the use of these dopants in green and blue QLEDs where EL stability is known to be generally much lower.

7.1 Doping ZnO by Halides for Inverted Green-QLED

The effect of I_2 and $FeCl_3$ doping in ZnO ETL on EL characteristics of green-QLED is investigated. The inverted QLED structure is used in this experiment in the same order to the inverted red-QLED except green emitting CdSe/ZnS QDs (from Mesolight Inc.) : ITO/ETL/green QD EML/CBP/MoO_3/Al, as schematically shown in Figure 7.1 (a). ZnO, I_2:ZnO, and $FeCl_3$:ZnO provide ETL whereas CBP and MoO_3 are used for HTL and HIL, respectively. Unlike the red QLED showing a minor change in the J-V-L characteristic as shown in Figure 7.1 (b), the J-V-L characteristic of green-QLED is largely affected by the I_2 and $FeCl_3$ in ZnO. As seen, the green-I_2:ZnO-QLED increases current density at any given bias than the green-ZnO-QLED, whereas the green-$FeCl_3$:ZnO-QLED decreases its current density compared to the green-ZnO-QLED. In addition, the I_2:ZnO decreases V_{on} while maintaining similar V_{th} to the control device, suggesting enhancement of radiative recombination. This suggests that I_2 may improve an electron injection into the green-QD EML. The $FeCl_3$:ZnO slightly increases V_{on}. On the other hand, V_{th} of the QLED may not be changed by the $FeCl_3$:ZnO. EL spectra show strong emission from the green-QDs at 526 nm wavelength with negligible parasitic emission, as can be seen in Figure 7.1 (c). Current efficiency *vs.* current density of the green-QLEDs is shown in Figure 7.1 (d). The current efficiency at 20

mA cm^{-2} shows the minor decrease in case of the I_2:ZnO-QLED in comparison with the ZnO-QLED. The $FeCl_3$:ZnO may affect the current efficiency of the QLED, showing significant efficiency roll-off above 10 mA cm^{-2}. Nevertheless, all the green-QLEDs have the similar current efficiency value under 20 mA cm^{-2} current flowing. Figure 7.1 (e) shows EL decay curves of the green-QLEDs with different ETLs. The EL decay is measured under 20 mA cm^{-2} constant current flowing in the QLEDs. The initial luminance values of the green-QLEDs with different ETLs are 3,900 cd m^{-2}, 3,810 cd m^{-2}, and 3,770 cd m^{-2}, for ZnO, I_2:ZnO, and $FeCl_3$:ZnO, respectively, indicating the minor difference of current efficiency at 20 mA cm^{-2}. The ZnO-QLED has LT50 value of 0.6 hours. The I_2:ZnO and the $FeCl_3$:ZnO both increase LT50 by 1.2, and 2.5 hours, respectively. The factor of the LT50 improvement in the green-QLED is 2.0× and 4.2× by I_2 and $FeCl_3$, respectively. The factors of improvement are coincided with the red-QLEDs, exhibiting the 2.2× and 3.6× by I_2 and $FeCl_3$, respectively. The LT50 results imply the similar role to the red-QLED from I_2 and $FeCl_3$ dopants in ZnO ETL in the EL stability in the green-QLED.

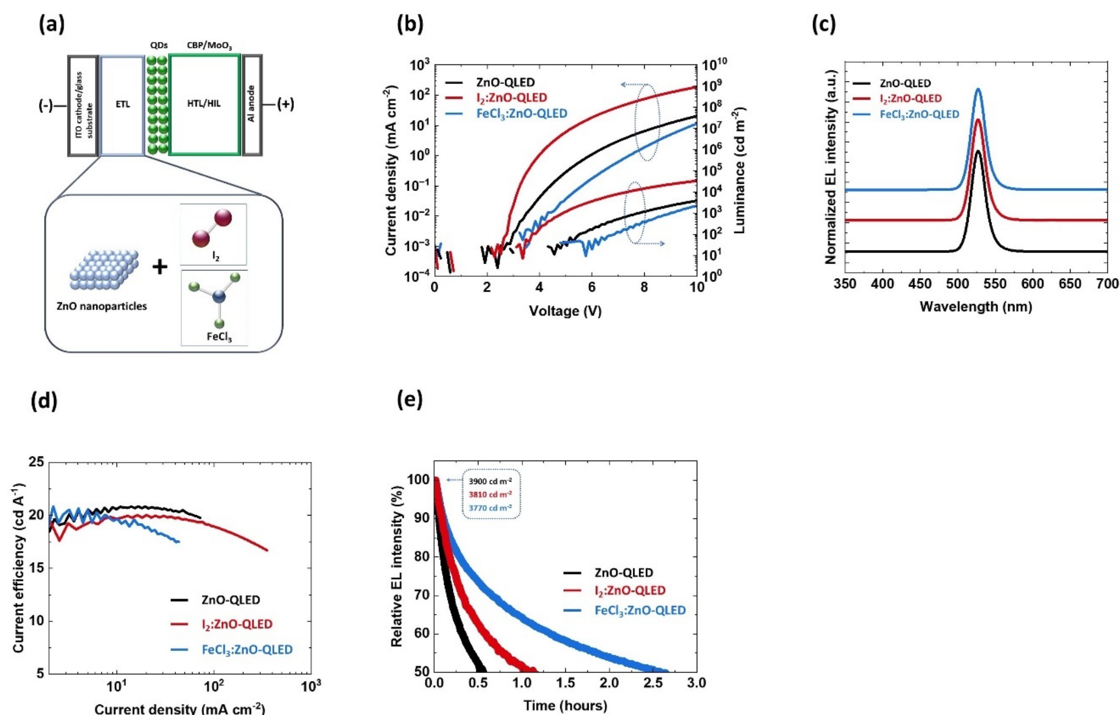

Figure 7.1 (a) Schematic diagram of the structure of the green inverted QLEDs. (b) J-V-L characteristics, (c) EL spectra, (d) current efficiency *vs.* current density, and (e) EL *vs.* time under 20 mA cm^{-2} constant current driving of the QLEDs.

7.2 The Halide Treatment on ETL for Upright Blue-QLED

7.2.1 Doping ZnO by Halides for Upright Blue-QLED

The use of the I_2 and $FeCl_3$ in ZnO in the blue-QLED is investigated. The EL stability of the blue-QLED is generally much lower than the other colors. Unlike the red-QLED where high efficiencies can be obtained in the inverted architecture, the high efficiency from blue QLED requires the use of the upright architecture and an encapsulation process in order to achieve the efficient electron injection. The upright device of the following structure with ZnO,

I_2:ZnO, and $FeCl_3$:ZnO are fabricated and tested : ITO/PEDOT:PSS/TFB/blue QDs/ETLs/Al, as depicted in Figure 7.2 (a). In these devices, the ITO and Al are used as an anode and cathode for injecting holes and electrons, respectively, whereas the PEDOT:PSS and TFB, both coated by spin-coating, function as hole injection and hole transport layers, respectively. In the QD EML, blue emitting CdSe/ZnS QDs (from Mesolight Inc.) are used. The devices are encapsulated using a UV-curable resin immediately after fabrication. All the EL characteristics are measured in 24 hours after the encapsulation, reaching their optimal device efficiencies. Figure 7.2 (b) shows the J-V-L characteristics of the blue-QLEDs with the ZnO, I_2:ZnO, and $FeCl_3$:ZnO. Above V_{th}, current density of the $FeCl_3$:ZnO-QLED decreases compared to the ZnO-QLED whereas the I_2:ZnO-QLED shows minor decrease. Noticeable, the subthreshold current of the blue-QLEDs is reduced by the I_2 and $FeCl_3$, which may be the similar effect of reduction in the subthreshold current in the red-QLED case as discussed in Figure 6.2. Unlike the negligible impact on luminance by the I_2, the $FeCl_3$ reduces the luminance in the blue-QLED, implying negative impact on radiative recombination within QD EML. Nonetheless, the major emission of photon at 470 nm wavelength should take place within QD EML as no discernable parasitic emission in the EL emission spectra in Figure 7.2 (c). Figure 7.2 (d) shows current efficiency of the blue-QLEDs with different ETLs. The result shows the somewhat increase in the current efficiency by the I_2:ZnO below 100 mA cm^{-2} whereas the $FeCl_3$:ZnO significantly reduces the current efficiency at any given current density. Because, in the upright architecture, the ZnO ETL is coated on top of the QD EML, additional constraints related to which dopants can be used without negatively affecting the QD EML arise. This investigation shows that using $FeCl_3$ as a dopant in ZnO in upright architectures reduces device efficiency and therefore is not suitable. The EL lifetime, therefore, is measured in blue-QLEDs with and without I_2 in ZnO. Figure 7.2 (e) shows EL stability test results from the blue-QLEDs with ZnO, and I_2:ZnO. As can be seen, while the EL lifetime is clearly limited, doping the ZnO with I_2 leads to 2~3 times longer LT50. The short EL lifetime indicates that additional degradation mechanisms must be at play and limiting the EL lifetime of these devices. The LT50 improvement, however, clearly demonstrates the benefits of using halide dopants for

addressing one of the degradation mechanisms in the upright blue-QLED and improving device stability.

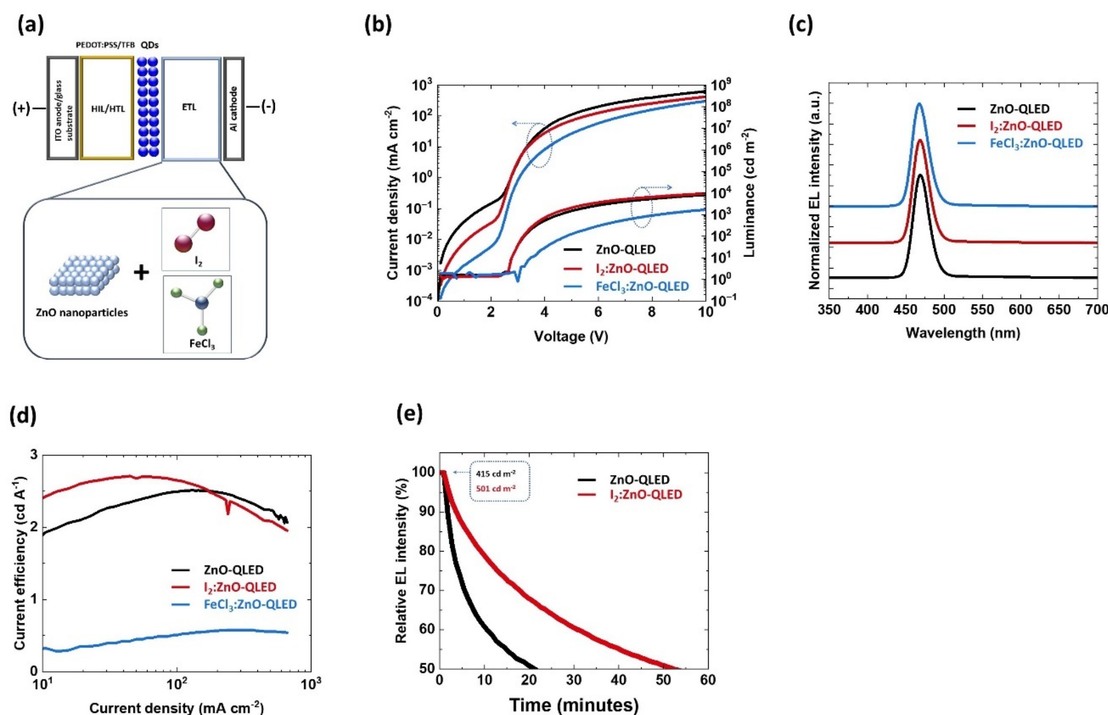

Figure 7.2 (a) Schematic diagram of the structure of the blue upright QLEDs with ZnO, I_2:ZnO, and $FeCl_3$:ZnO. (b) J-V-L characteristics, (c) EL spectra, (d) current efficiency *vs.* current density, and (e) EL *vs.* time under 20 mA cm^{-2} constant current driving of the QLEDs.

7.2.2 Doping ZnMgO by Halides for Upright Blue-QLED

Recent publications reported that ZnMgO can provide blue-QLED with higher device efficiency than ZnO. Therefore, most of blue-QLEDs has been using the ZnMgO ETL. It becomes interesting to test the effect of halide dopants in the ZnMgO on the blue-QLED stability. The investigation in sub-section 7.2.1 shows that using $FeCl_3$ as a dopant in ZnO in the upright blue-QLED reduces device efficiency. The investigation of using I_2 in the ZnMgO

is, therefore, performed in this sub-section. The upright blue-QLED of the following structure with ZnMgO, and I_2:ZnMgO are fabricated and tested : ITO/PEDOT:PSS/TFB/blue-QD EML/ETLs/Al, as depicted in Figure 7.3 (a). The devices are encapsulated using UV-curable resin immediately after fabrication. All the EL characteristics are measured in 24 hours after the encapsulation in order to achieve high device efficiency.

Figure 7.3 (b) shows the J-V-L characteristics of the blue-QLEDs with ZnMgO, and I_2:ZnMgO. The J-V-L curves of two devices have almost identical shape, implying the negligible impact from I_2 on electrical property of ZnMgO. Also, the majority of EL emission at 470 nm wavelength without discernable parasitic emission is observed in the EL emission spectra shown in Figure 7.3 (c). Figure 7.3 (d) shows current efficiency *vs.* current density of the blue-QLEDs with ZnMgO and I_2:ZnMgO. It shows the sudden increase of the efficiency above 26 mA cm^{-2} in both devices. This may be due to the micro-short effect during electrical measurement that temporarily reduces resistivity possibly at the interfaces. Nonetheless, the two devices have identical value of current efficiency at 20 mA cm^{-2}. Figure 7.3 (e) shows EL stability test results from the blue-QLEDs with ZnMgO, and I_2:ZnMgO. Unlike the improvement in EL lifetime in case of blue-QLED with I_2:ZnO compared to ZnO, I_2 do not increase EL stability of the blue QLED using ZnMgO ETL.

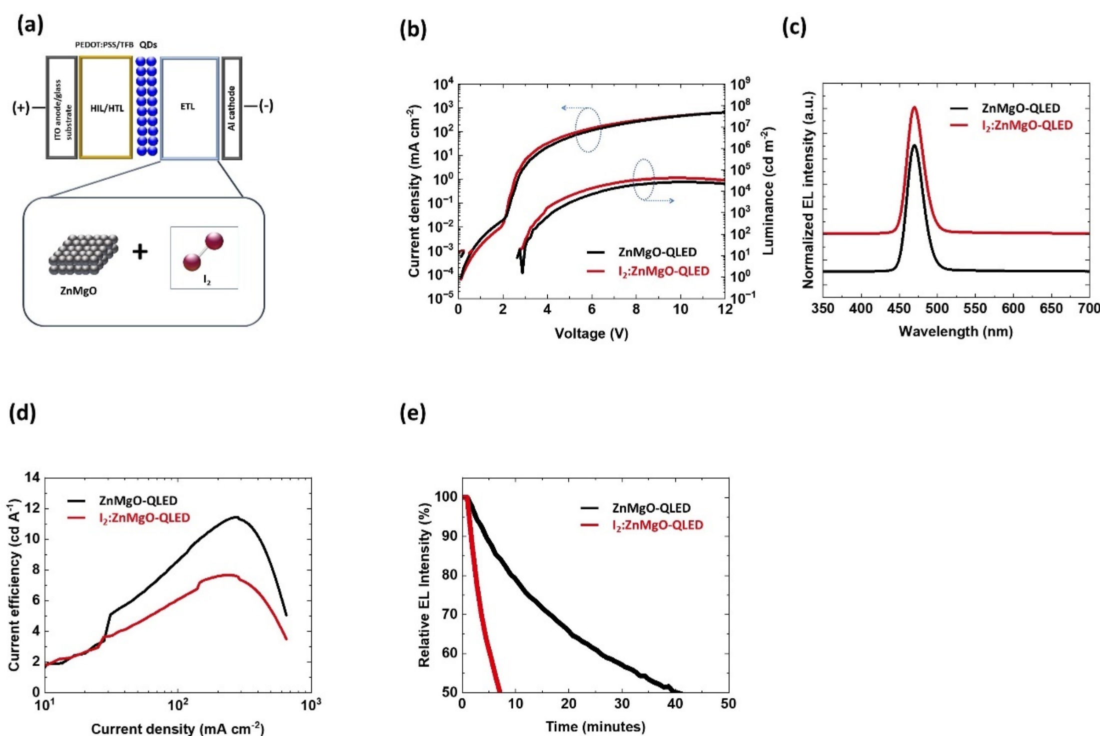

Figure 7.3 (a) Schematic diagram of the structure of the blue upright QLEDs with ZnMgO, and I_2:ZnMgO. (b) J-V-L characteristics, (c) EL spectra, (d) current efficiency *vs.* current density, and (e) EL *vs.* time under 20 mA cm^{-2} constant current driving of the QLEDs.

The limited effect from I_2 in the ZnMgO on the QLED stability is possibly due to the presence of Mg that can reduce the density of oxygen vacancies in ZnO. Figure 7.4 shows XPS spectra of O 1s core level electrons of ZnO and ZnMgO. As seen in Figure 7.4 (a), the XPS spectra of O 1s core level electrons in the ZnO can be deconvoluted into three bands. The lowest energy band (O_i, at 531.6 eV) can be ascribed to lattice oxygen, whereas the middle (O_{ii}, at 532.7 eV) and the highest energy bands (O_{iii}, at 533.7 eV) correspond to electronic states associated with oxygen vacancies and hydroxyl groups, respectively[148]. The XPS spectrum of O 1s core level electrons of the ZnMgO is also deconvoluted into three bands in the same

manner.[202] As shown in Figure 7.4 (b), O_{ii} band is reduced in the ZnMgO compared to the ZnO. This suggests that Mg reduces the density of oxygen vacancies. According to the investigation, the halide dopants suppress the degradation originated from the presence of V_O. The V_O passivation effect of Mg may limit the effects from the halide treatment. The XPS spectra as well as the results of the EL characteristics indicate that the halide dopant in ZnMgO may not induce significant improvement in the stability of the upright blue-QLED using ZnMgO ETL.

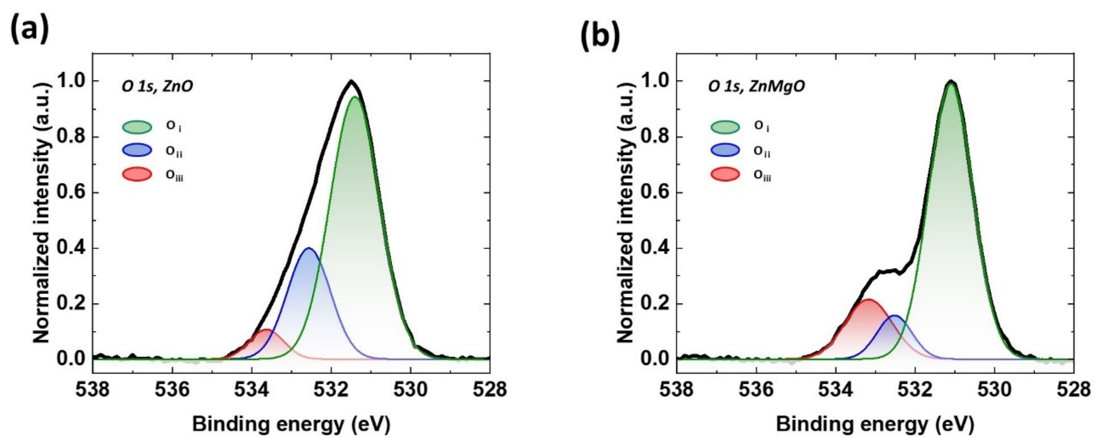

Figure 7.4 XPS spectra of O 1s core level electrons from (a) ZnO, and (b) ZnMgO.

7.3 Chapter Summary

The effect of I_2 and $FeCl_3$ dopants in ZnO ETL on inverted green-QLED is discussed. Unlike the inverted red-QLED, the J-V-L characteristic of the green-QLED is changed by introducing I_2 and $FeCl_3$ in ZnO, indicating that the halides affect electron injection property. On the other hand, current efficiency values of the green-QLEDs with the different ETLs are similar under 20 mA cm^{-2} current flowing. The inverted green-QLED with ZnO demonstrates the LT50 value of 0.6 hours. Both I_2:ZnO and $FeCl_3$:ZnO increase LT50, with I_2 leading to 2.0× and $FeCl_3$ resulting in 4.2× enhancement.

The use of the I_2 and $FeCl_3$ in ZnO is also explored for the upright blue-QLED. While I_2:ZnO has negligibly impact on the current efficiency, $FeCl_3$:ZnO reduces the current efficiency significantly. The LT50 of the upright blue-QLED with I_2:ZnO is nearly three times longer than with neat ZnO. The influence of I_2 dopant in ZnMgO and its effect on the upright blue-QLED are also discussed. The result shows the limited effect on the QLED stability possibly due to the presence of Mg that could reduce the density of oxygen vacancies in ZnO.

The results demonstrate that the halide treatment of ZnO ETL holds the potential to attain high EL stability of green- and blue-QLEDs.

Chapter 8 Summary and Suggestions for Future Work

8.1 Summary

This thesis discusses new approaches for ZnO modifications and investigation of their impact on QLED performance, generally focused on the EL stability. QLEDs have been receiving enormous attention from the research community as a strong candidate for a next generation EL devices. At the present, the efficiency of QLEDs is comparable to state-of-the art OLEDs. For successful commercialization, very high EL stability, on par with that of state-of-the-art OLED, is also required. However, unlike the factors that govern efficiency, a clear understanding of degradation mechanisms in these devices and of the factors that limit device lifetime is still lacking. This is due – at least in part - to the difficulty of diagnosing the exact causes of device degradation during long-term operation amid numerous external conditions. In stacked QLED structure with multiple materials, charge concentrations and their build-up in the layers, bulk, and at interlayer interfaces directly influence excitonic phenomena and the efficiency of the radiative processes within the QD EML. Therefore, optimizing charge distribution across QLED as well as charge injection and transport in the QD EML and the CTL is crucial for device efficiency and stability. ZnO has become the material of choice for their ETLs almost universally due to its good electron transport and injection properties well matched with QDs. Electrical properties, and stoichiometric and structural defect states in ZnO, however, can induce device degradation via various processes.

The main findings derived from the experiments and analysis presented in this thesis are as follows:

Blending Polyethylenimine and ZnO for New Form of Electron Transport Layer

1. Adding PEI to ZnO to form a blended ZnO:PEI ETL improves device efficiency by more than 50 % compared to QLED with only ZnO ETL. The ZnO:PEI ETL has a significant advantage in terms of improving device stability. A device with a ZnO:PEI ETL containing 0.3 wt% PEI exhibits an LT50 of 153,735 hours (for L_0 of 100 cd m^{-2}), almost 10× longer

than a ZnO ETL control device.

2. J-V characteristics from electron-only devices and delayed EL measurements show that the ZnO:PEI ETL alters charge distribution in the HTLs changing the nature of residual charges that remain unrecombined in the device from ones that are more mobile to ones that are more strongly trapped, corroborating the conclusion that the stability enhancement is associated with reduced charge accumulation at the QD/HTL interface.

3. Tests on devices that contain a CBP:FIrpic marking layer reveal that the ZnO:PEI ETL results in a deeper penetration of electrons into the HTL in comparison to ZnO/PEI or ZnO ETLs, likely due to changes in electric field distribution that also facilitate hole injection from the HTL to the QD. The electrons can neutralize accumulated holes at the QDs/CBP interface, which removes one of the main causes of device degradation.

CF_4-plasma Treatment on ZnO Nanoparticles

1. The results demonstrate that chemically treating the ZnO NP ETLs of QLEDs by F plasmas, using carbon tetrafluoride (CF_4) as a source gas, is found to bring about significant improvements in device EL stability, demonstrating an LT50 at 100 cd m^{-2} of 2,370,000 hours in red inverted devices, 47× longer than untreated ZnO. It also leads to 15 % higher EQE.

2. XPS, TOF-SIMS and PL measurements reveal that the treatment results in the incorporation of F across the entire bulk of the ZnO film, leading to the passivation of the sub-band gap states, commonly associated with oxygen vacancies in ZnO films.

3. Electrical measurements on full devices as well as on electron only devices show a decrease in recombination currents and an earlier onset of trap-filled conduction when the treated films are used, both pointing to the role of F in passivating defect states.

4. TRPL measurements show a longer QD exciton lifetime in devices with FZnO ETLs confirming the defect passivation effect. Additional TRPL measurements under bias reveal

that QD exciton lifetime changes differently with current flow in devices with FZnO *vs.* ZnO, suggesting that the F treatment leads to increased electron concentration and trion formation in the QD layers.

5. The higher electron concentration in the QD layer is verified from tests on devices containing a FIrpic luminescent layer, which also show that the use of FZnO increases e-h recombination at the QD/HTL interface.

6. C-V-L measurements give further evidence of the increased e-h recombination rate at the QD/HTL interface in QLEDs with FZnO ETL, and of a subsequent decrease in hole accumulation at the interface, the latter known to be a major cause of degradation in these devices, suggesting that the significant stability improvement upon using FZnO is caused by a modulation of electron distribution across the device that leads to a reduction in hole accumulation.

Introducing I_2 and $FeCl_3$ dopants into ZnO Nanoparticles

1. By introducing I_2 and $FeCl_3$ as halide dopants into ZnO ETL, the LT50 of red QLEDs increases by 2.2× and 3.6×, respectively, demonstrating 124.3 hours and 206.1 hours instead of only 56.9 hours in devices with undoped ZnO, all tested at 20 mA cm^{-2} and from an initial luminance of ~3,000 cd m^{-2}.

2. Results show the LT50 enhancement is primarily due to changes in the EL loss rate in the early stages of the electrical aging behavior of the devices (in the first 50 hours of electrical aging). An analysis of changes in the L-J characteristics of the devices by electrical aging reveals that the fast initial EL loss is associated with an increase in trap density in the ZnO ETLs as well as in the number of holes that leak to the ETL, both of which are reduced by the use of the halide dopants.

3. PL measurements show that interfacial charge transfer at the ZnO/QDs interface occurs, leading to the formation of positively charged defect states (likely oxygen vacancies) in

ZnO, subsequently leading to luminance quenching. The measurements also show that using the halide dopants reduces this interfacial charge transfer possibly due to their role in acting as hole scavengers that trap and efficiently neutralize holes in ZnO.

4. XPS studies show that electrical aging of QLEDs leads to an increase in the concentration of ZnO species with higher oxidative states and that a correlation between the magnitude of EL loss and the concentration of these species exists. The studies show that using the halide dopants significantly reduces the formation of these species as well as positive charging in the ETL during electrical stress.

The investigations reveal the significant roles of the ZnO modifications in the device stability improvement. Incorporating PEI changes the electrical conductivity of the QLED, leading to reduction of the energy barrier at the QDs/HTL interface. This facilitates electron penetration into HTL, increasing higher electron density near the QD EML/HTL interface. Fluorine effectively passivates the trap states due to its comparable atomic size to the oxygen vacancy. The fluorine treatment leads to increased electron concentration in the QD EML and near the QD EML/HTL interface by reducing the electron trap states in the ZnO. The primary factor contributing to the device stability improvement in the QLEDs with ZnO:PEI and FZnO is revealed to share a common mechanism: the increase in electron concentration near the QD EML/HTL interface, and thereby reducing the concentration of positive space charge within the HTL. Another major factor for increasing device stability is observed by the investigation of the effect of I_2 and $FeCl_3$ dopants in ZnO ETL. Unlike the fluorine, the iodine and chlorine perhaps do not completely occupy and fill oxygen vacancies due to the relatively large atomic radii. Instead, the presence of these dopants reduces positive charge accumulation in the ZnO due to their role in acting as hole scavengers that efficiently neutralizes holes in ZnO.

In summary, these findings introduce novel and effective strategies for achieving highly stable QLEDs, providing a valuable contribution to the research field. The findings in this work provide new insights into the critical roles of managing trap states in ZnO and

optimizing charge distribution and accumulation across the layers within QLED, as well as the significant role of managing positive charges in ZnO and across the QLED for achieving high EL stability.

8.2 Future Work

Although the research and development on CdSe-based QDs have reached a mature stage and have successfully demonstrated their potential as an EML for LED structures, the use of Cd has been restricted in manufacturing due to its toxicity. For example, as a market of wearable device applications has been growing, the demand for toxic-free materials has significantly increased. InP[92], carbon dot[203] and lead-free perovskite QD[204] materials have been proposed and developed for potential alternatives of Cd-based QDs; however, their device efficiency and stability still need to be improved. One of the factors to limited device performance with these materials is the presence of excessive charges and intrinsic trap states, which can adversely affect device performance via various processes[44,92,205,206]. Therefore, effective methods for managing these charges are crucial in order to achieve high performance QLEDs with such materials.

Halides are reactive elements that have been utilized in various nanomaterials to manipulate physical properties. For example, the halides passivate trap states, effectively modulate the electrical property and charge distribution, and prevent the formation of charged species in nanoparticles during device operation. Exploring the impact of incorporating halide dopants into Cd-free QDs holds significant value for the development of such QD material-based device applications. Particularly, this strategy can be valuable for materials, such as InP and perovskite QDs, that have suffered from poor stability due to excessive charges or intrinsic trap states.

Furthermore, it could be anticipated that the importance of optimizing device architecture is increasing once the PL stability of these QD materials approaches a stable state. This includes finding improved and suitable materials for functional materials and engineering

CTLs, as exemplified in the progression of CdSe-QLED. The study in this thesis has identified the fundamental limitations of the materials, particularly ZnO ETL, and proposed potential strategies to address the challenges. The strategies proposed in the thesis can be extrapolated to other forms of metal oxides and materials, offering a effective method to manipulate their electrical properties.

References

1. Yi, J. Introduction to Display Engineering. **2019**.
2. Krüger, A.; Kuflik, T. *Ubiquitous Display Environments*; Springer: 2012.
3. Park, Y.-J. Display Technologies for Immersive Devices and Electronic Skin. *Electronics and Telecommunications Trends* **2019,** *34,* 10-18.
4. Palomaki, P. Quantum Dots+ Oled= Your Next Tv: Formerly Rival Technologies Will Come Together in New Samsung Displays. *IEEE Spectrum* **2022,** *59,* 52-53.
5. Marnocha, J. C. Effect of Wannier-Mott Exciton on Semiconductor Quantum Dot Photo-Absorption Spectra. **2017**.
6. Pietryga, J. M.; Park, Y.-S.; Lim, J.; Fidler, A. F.; Bae, W. K.; Brovelli, S.; Klimov, V. I. Spectroscopic and Device Aspects of Nanocrystal Quantum Dots. *Chemical reviews* **2016,** *116,* 10513-10622.
7. García de Arquer, F. P.; Talapin, D. V.; Klimov, V. I.; Arakawa, Y.; Bayer, M.; Sargent, E. H. Semiconductor Quantum Dots: Technological Progress and Future Challenges. *Science* **2021,** *373,* eaaz8541.
8. Anderson, B.; Anderson, R. *Fundamentals of Semiconductor Devices*; McGraw-Hill, Inc.: 2004.
9. So, F. *Organic Electronics: Materials, Processing, Devices and Applications*; CRC press: 2009.
10. Yersin, H. *Highly Efficient Oleds with Phosphorescent Materials*; John Wiley & Sons: 2008.
11. Ishii, H.; Sugiyama, K.; Ito, E.; Seki, K. Energy Level Alignment and Interfacial Electronic Structures at Organic/Metal and Organic/Organic Interfaces. *Advanced materials* **1999,** *11,* 605-625.
12. Deng, Y.; Lin, X.; Fang, W.; Di, D.; Wang, L.; Friend, R. H.; Peng, X.; Jin, Y. Deciphering Exciton-Generation Processes in Quantum-Dot Electroluminescence. *Nature communications* **2020,** *11,* 1-8.
13. Kim, J.; Hahm, D.; Bae, W. K.; Lee, H.; Kwak, J. Transient Dynamics of Charges and Excitons in Quantum Dot Light-Emitting Diodes. *Small* **2022,** *18,* 2202290.
14. Lee, H.; Jeong, B. G.; Bae, W. K.; Lee, D. C.; Lim, J. Surface State-Induced Barrierless Carrier Injection in Quantum Dot Electroluminescent Devices. *Nature communications* **2021,** *12,* 1-9.
15. Lim, J.; Park, Y.-S.; Klimov, V. I. Optical Gain in Colloidal Quantum Dots Achieved with Direct-Current Electrical Pumping. *Nature Materials* **2018,** *17,* 42-49.
16. Colvin, V. L.; Schlamp, M. C.; Alivisatos, A. P. Light-Emitting Diodes Made from Cadmium Selenide Nanocrystals and a Semiconducting Polymer. *Nature* **1994,** *370,* 354-357.
17. Coe, S.; Woo, W.-K.; Bawendi, M.; Bulović, V. Electroluminescence from Single Monolayers of Nanocrystals in Molecular Organic Devices. *Nature* **2002,** *420,* 800-803.
18. Mueller, A. H.; Petruska, M. A.; Achermann, M.; Werder, D. J.; Akhadov, E. A.; Koleske, D. D.; Hoffbauer, M. A.; Klimov, V. I. Multicolor Light-Emitting Diodes Based on Semiconductor Nanocrystals Encapsulated in Gan Charge Injection Layers. *Nano Letters* **2005,** *5,* 1039-1044.
19. Caruge, J.-M.; Halpert, J. E.; Bulović, V.; Bawendi, M. G. Nio as an Inorganic Hole-Transporting Layer in Quantum-Dot Light-Emitting Devices. *Nano letters* **2006,** *6,* 2991-2994.
20. Song, J.; Wang, O.; Shen, H.; Lin, Q.; Li, Z.; Wang, L.; Zhang, X.; Li, L. S. Over 30% External Quantum Efficiency Light-Emitting Diodes by Engineering Quantum Dot-Assisted Energy Level Match for Hole Transport Layer. *Advanced Functional Materials* **2019,** *29,* 1808377.

21. Dai, X.; Zhang, Z.; Jin, Y.; Niu, Y.; Cao, H.; Liang, X.; Chen, L.; Wang, J.; Peng, X. Solution-Processed, High-Performance Light-Emitting Diodes Based on Quantum Dots. *Nature* **2014,** *515,* 96-99.
22. Manders, J. R.; Qian, L.; Titov, A.; Hyvonen, J.; Tokarz-Scott, J.; Acharya, K. P.; Yang, Y.; Cao, W.; Zheng, Y.; Xue, J. High Efficiency and Ultra-Wide Color Gamut Quantum Dot Leds for Next Generation Displays. *Journal of the Society for Information Display* **2015,** *23,* 523-528.
23. Deng, Y.; Peng, F.; Lu, Y.; Zhu, X.; Jin, W.; Qiu, J.; Dong, J.; Hao, Y.; Di, D.; Gao, Y.; Sun, T.; Zhang, M.; Liu, F.; Wang, L.; Ying, L.; Huang, F.; Jin, Y. Solution-Processed Green and Blue Quantum-Dot Light-Emitting Diodes with Eliminated Charge Leakage. *Nature Photonics* **2022**.
24. Kim, T.; Kim, K.-H.; Kim, S.; Choi, S.-M.; Jang, H.; Seo, H.-K.; Lee, H.; Chung, D.-Y.; Jang, E. Efficient and Stable Blue Quantum Dot Light-Emitting Diode. *Nature* **2020,** *586,* 385-389.
25. Wang, O.; Wang, L.; Li, Z.; Xu, Q.; Lin, Q.; Wang, H.; Du, Z.; Shen, H.; Li, L. S. High-Efficiency, Deep Blue Zncds/Cd X Zn 1− X S/Zns Quantum-Dot-Light-Emitting Devices with an Eqe Exceeding 18%. *Nanoscale* **2018,** *10,* 5650-5657.
26. Mashford, B. S.; Stevenson, M.; Popovic, Z.; Hamilton, C.; Zhou, Z.; Breen, C.; Steckel, J.; Bulovic, V.; Bawendi, M.; Coe-Sullivan, S. High-Efficiency Quantum-Dot Light-Emitting Devices with Enhanced Charge Injection. *Nature photonics* **2013,** *7,* 407-412.
27. Schlamp, M.; Peng, X.; Alivisatos, A.-l. Improved Efficiencies in Light Emitting Diodes Made with Cdse (Cds) Core/Shell Type Nanocrystals and a Semiconducting Polymer. *Journal of applied physics* **1997,** *82,* 5837-5842.
28. Murawski, C.; Leo, K.; Gather, M. C. Efficiency Roll-Off in Organic Light-Emitting Diodes. *Advanced Materials* **2013,** *25,* 6801-6827.
29. Kim, H.-M.; Youn, J.-H.; Seo, G.-J.; Jang, J. Inverted Quantum-Dot Light-Emitting Diodes with Solution-Processed Aluminium–Zinc Oxide as a Cathode Buffer. *Journal of Materials chemistry c* **2013,** *1,* 1567-1573.
30. Kim, T.-H.; Cho, K.-S.; Lee, E. K.; Lee, S. J.; Chae, J.; Kim, J. W.; Kim, D. H.; Kwon, J.-Y.; Amaratunga, G.; Lee, S. Y. Full-Colour Quantum Dot Displays Fabricated by Transfer Printing. *Nature photonics* **2011,** *5,* 176-182.
31. Hofbeck, T.; Monkowius, U.; Yersin, H. Highly Efficient Luminescence of Cu (I) Compounds: Thermally Activated Delayed Fluorescence Combined with Short-Lived Phosphorescence. *Journal of the American Chemical Society* **2015,** *137,* 399-404.
32. Stouwdam, J. W.; Janssen, R. A. Red, Green, and Blue Quantum Dot Leds with Solution Processable Zno Nanocrystal Electron Injection Layers. *Journal of Materials Chemistry* **2008,** *18,* 1889-1894.
33. Znaidi, L. Sol–Gel-Deposited Zno Thin Films: A Review. *Materials Science and Engineering: B* **2010,** *174,* 18-30.
34. Gurylev, V.; Perng, T. P. Defect Engineering of Zno: Review on Oxygen and Zinc Vacancies. *Journal of the European Ceramic Society* **2021,** *41,* 4977-4996.
35. Casteleiro, C.; Gomes, H. L.; Stallinga, P.; Bentes, L.; Ayouchi, R.; Schwarz, R. Study of Trap States in Zinc Oxide (Zno) Thin Films for Electronic Applications. *Journal of non-crystalline solids* **2008,** *354,* 2519-2522.
36. Liu, L.; Mei, Z.; Tang, A.; Azarov, A.; Kuznetsov, A.; Xue, Q.-K.; Du, X. Oxygen Vacancies: The Origin of N-Type Conductivity in Zno. *Physical Review B* **2016,** *93,* 235305.
37. Chicot, G.; Muret, P.; Santailler, J.-L.; Feuillet, G.; Pernot, J. Oxygen Vacancy and Ec− 1 Ev Electron Trap in Zno. *Journal of Physics D: Applied Physics* **2014,** *47,* 465103.

38. Qian, L.; Zheng, Y.; Xue, J.; Holloway, P. H. Stable and Efficient Quantum-Dot Light-Emitting Diodes Based on Solution-Processed Multilayer Structures. *Nature photonics* **2011,** *5,* 543-548.
39. Bae, W. K.; Padilha, L. A.; Park, Y.-S.; McDaniel, H.; Robel, I.; Pietryga, J. M.; Klimov, V. I. Controlled Alloying of the Core–Shell Interface in Cdse/Cds Quantum Dots for Suppression of Auger Recombination. *ACS Nano* **2013,** *7,* 3411-3419.
40. Aziz, H.; Popovic, Z. D.; Hu, N.-X. Organic Light Emitting Devices with Enhanced Operational Stability at Elevated Temperatures. *Applied physics letters* **2002,** *81,* 370-372.
41. Chen, S.; Cao, W.; Liu, T.; Tsang, S.-W.; Yang, Y.; Yan, X.; Qian, L. On the Degradation Mechanisms of Quantum-Dot Light-Emitting Diodes. *Nature communications* **2019,** *10,* 1-9.
42. Davidson-Hall, T.; Aziz, H. The Role of Excitons within the Hole Transporting Layer in Quantum Dot Light Emitting Device Degradation. *Nanoscale* **2019,** *11,* 8310-8318.
43. Doe, T.; Kitano, K.; Yamamoto, S.; Yamamoto, M.; Goto, K.; Sakakibara, Y.; Kobashi, T.; Yamada, H.; Ueda, M.; Ryowa, T. Evaluation of Degradation Behavior in Quantum Dot Light-Emitting Diode with Different Hole Transport Materials Via Transient Electroluminescence. *Applied Physics Letters* **2021,** *118,* 203503.
44. Kim, K.; Hahm, D.; Baek, G. W.; Lee, T.; Shin, D.; Lim, J.; Bae, W. K.; Kwak, J. Effect of Excess Carriers on the Degradation of Inp-Based Quantum-Dot Light-Emitting Diodes. *ACS Applied Electronic Materials* **2022**.
45. Chung, D. S.; Davidson-Hall, T.; Cotella, G.; Lyu, Q.; Chun, P.; Aziz, H. Significant Lifetime Enhancement in Qleds by Reducing Interfacial Charge Accumulation Via Fluorine Incorporation in the Zno Electron Transport Layer. *Nano-Micro Letters* **2022,** *14,* 212.
46. Chung, D. S.; Davidson-Hall, T.; Yu, H.; Samaeifar, F.; Chun, P.; Lyu, Q.; Cotella, G.; Aziz, H. Significant Enhancement in Quantum-Dot Light Emitting Device Stability Via a Zno: Polyethylenimine Mixture in the Electron Transport Layer. *Nanoscale Advances* **2021,** *3,* 5900-5907.
47. Ding, S.; Wu, Z.; Qu, X.; Tang, H.; Wang, K.; Xu, B.; Sun, X. W. Impact of the Resistive Switching Effects in Znmgo Electron Transport Layer on the Aging Characteristics of Quantum Dot Light-Emitting Diodes. *Applied Physics Letters* **2020,** *117,* 093501.
48. Davidson-Hall, T.; Aziz, H. Perspective: Toward Highly Stable Electroluminescent Quantum Dot Light-Emitting Devices in the Visible Range. *Applied Physics Letters* **2020,** *116,* 010502.
49. Moon, H.; Lee, C.; Lee, W.; Kim, J.; Chae, H. Stability of Quantum Dots, Quantum Dot Films, and Quantum Dot Light-Emitting Diodes for Display Applications. *Advanced Materials* **2019,** *31,* 1804294.
50. Dupont's Oled Material Hits Million-Hour Lifetime. *Nature Photonics* **2009,** *3,* 441-441.
51. Lee, T.; Kim, B. J.; Lee, H.; Hahm, D.; Bae, W. K.; Lim, J.; Kwak, J. Bright and Stable Quantum Dot Light-Emitting Diodes. *Advanced Materials* **2022,** *34,* 2106276.
52. Nirmal, M.; Dabbousi, B. O.; Bawendi, M. G.; Macklin, J.; Trautman, J.; Harris, T.; Brus, L. E. Fluorescence Intermittency in Single Cadmium Selenide Nanocrystals. *Nature* **1996,** *383,* 802-804.
53. Mahler, B.; Spinicelli, P.; Buil, S.; Quelin, X.; Hermier, J.-P.; Dubertret, B. Towards Non-Blinking Colloidal Quantum Dots. *Nature materials* **2008,** *7,* 659-664.
54. Galland, C.; Ghosh, Y.; Steinbrück, A.; Sykora, M.; Hollingsworth, J. A.; Klimov, V. I.; Htoon, H. Two Types of Luminescence Blinking Revealed by Spectroelectrochemistry of Single Quantum Dots. *Nature* **2011,** *479,* 203-207.
55. Efros, A. L.; Nesbitt, D. J. Origin and Control of Blinking in Quantum Dots. *Nature Nanotechnology* **2016,** *11,* 661-671.

56. Yuan, G.; Gomez, D. E.; Kirkwood, N.; Boldt, K.; Mulvaney, P. Two Mechanisms Determine Quantum Dot Blinking. *ACS nano* **2018,** *12,* 3397-3405.
57. McGuire, J. A.; Sykora, M.; Joo, J.; Pietryga, J. M.; Klimov, V. I. Apparent Versus True Carrier Multiplication Yields in Semiconductor Nanocrystals. *Nano Letters* **2010,** *10,* 2049-2057.
58. Hu, Z.; Liu, S.; Qin, H.; Zhou, J.; Peng, X. Oxygen Stabilizes Photoluminescence of Cdse/Cds Core/Shell Quantum Dots Via Deionization. *Journal of the American Chemical Society* **2020,** *142,* 4254-4264.
59. Hu, Z.; Shu, Y.; Qin, H.; Hu, X.; Peng, X. Water Effects on Colloidal Semiconductor Nanocrystals: Correlation of Photophysics and Photochemistry. *Journal of the American Chemical Society* **2021,** *143,* 18721-18732.
60. Lim, J.; Park, Y.-S.; Wu, K.; Yun, H. J.; Klimov, V. I. Droop-Free Colloidal Quantum Dot Light-Emitting Diodes. *Nano letters* **2018,** *18,* 6645-6653.
61. Ye, Y.; Zheng, X.; Chen, D.; Deng, Y.; Chen, D.; Hao, Y.; Dai, X.; Jin, Y. Design of the Hole-Injection/Hole-Transport Interfaces for Stable Quantum-Dot Light-Emitting Diodes. *The Journal of Physical Chemistry Letters* **2020,** *11,* 4649-4654.
62. Aziz, H.; Popovic, Z. D.; Hu, N.-X.; Hor, A.-M.; Xu, G. Degradation Mechanism of Small Molecule-Based Organic Light-Emitting Devices. *Science* **1999,** *283,* 1900-1902.
63. Chang, J. H.; Park, P.; Jung, H.; Jeong, B. G.; Hahm, D.; Nagamine, G.; Ko, J.; Cho, J.; Padilha, L. A.; Lee, D. C. Unraveling the Origin of Operational Instability of Quantum Dot Based Light-Emitting Diodes. *ACS nano* **2018,** *12,* 10231-10239.
64. Pu, C.; Dai, X.; Shu, Y.; Zhu, M.; Deng, Y.; Jin, Y.; Peng, X. Electrochemically-Stable Ligands Bridge the Photoluminescence-Electroluminescence Gap of Quantum Dots. *Nature Communications* **2020,** *11,* 937.
65. Green, M. The Nature of Quantum Dot Capping Ligands. *Journal of Materials Chemistry* **2010,** *20,* 5797-5809.
66. Munro, A. M.; Bardecker, J. A.; Liu, M. S.; Cheng, Y.-J.; Niu, Y.-H.; Plante, I. J.-L.; Jen, A. K.-Y.; Ginger, D. S. Colloidal Cdse Quantum Dot Electroluminescence: Ligands and Light-Emitting Diodes. *Microchimica Acta* **2008,** *160,* 345-350.
67. Blauth, C.; Mulvaney, P.; Hirai, T. Transient Overshoot and Storage of Charge Carriers on Ligands in Quantum Dot Leds. *Journal of Applied Physics* **2019,** *126,* 075501.
68. Karon, K.; Lapkowski, M. Carbazole Electrochemistry: A Short Review. *Journal of Solid State Electrochemistry* **2015,** *19,* 2601-2610.
69. Zeng, H.; Duan, G.; Li, Y.; Yang, S.; Xu, X.; Cai, W. Blue Luminescence of Zno Nanoparticles Based on Non-Equilibrium Processes: Defect Origins and Emission Controls. *Advanced Functional Materials* **2010,** *20,* 561-572.
70. Jaziri, S., Electric Field Effect on Frenkel-Wannier-Mott Exciton States in Organic-Inorganic Semiconductor Quantum Wells. In *Science and Technology of Polymers and Advanced Materials: Emerging Technologies and Business Opportunities*, Prasad, P. N.; Mark, J. E.; Kandil, S. H.; Kafafi, Z. H., Eds. Springer US: Boston, MA, 1998; pp 251-258.
71. Lee, E. M.; Tisdale, W. A. Determination of Exciton Diffusion Length by Transient Photoluminescence Quenching and Its Application to Quantum Dot Films. *The Journal of Physical Chemistry C* **2015,** *119,* 9005-9015.
72. Davidson-Hall, T.; Aziz, H. The Role of Polyethylenimine in Enhancing the Efficiency of Quantum Dot Light-Emitting Devices. *Nanoscale* **2018,** *10,* 2623-2631.

73. Asok, A.; Gandhi, M. N.; Kulkarni, A. Enhanced Visible Photoluminescence in Zno Quantum Dots by Promotion of Oxygen Vacancy Formation. *Nanoscale* **2012,** *4,* 4943-4946.
74. Penfold, T. J.; Szlachetko, J.; Santomauro, F. G.; Britz, A.; Gawelda, W.; Doumy, G.; March, A. M.; Southworth, S. H.; Rittmann, J.; Abela, R.; Chergui, M.; Milne, C. J. Revealing Hole Trapping in Zinc Oxide Nanoparticles by Time-Resolved X-Ray Spectroscopy. *Nature Communications* **2018,** *9,* 478.
75. Chen, Z.; Wang, J.; Wu, H.; Yang, J.; Wang, Y.; Zhang, J.; Bao, Q.; Wang, M.; Ma, Z.; Tress, W. A Transparent Electrode Based on Solution-Processed Zno for Organic Optoelectronic Devices. *Nature Communications* **2022,** *13,* 1-12.
76. Vempati, S.; Mitra, J.; Dawson, P. One-Step Synthesis of Zno Nanosheets: A Blue-White Fluorophore. *Nanoscale research letters* **2012,** *7,* 1-10.
77. Keating, L. P.; Lee, H.; Rogers, S. P.; Huang, C.; Shim, M. Charging and Charged Species in Quantum Dot Light-Emitting Diodes. *Nano Letters* **2022**.
78. Chen, D.; Ma, L.; Chen, Y.; Zhou, X.; Xing, S.; Deng, Y.; Hao, Y.; Pu, C.; Kong, X.; Jin, Y. Electrochemically Stable Ligands of Zno Electron-Transporting Layers for Quantum-Dot Light-Emitting Diodes. *Nano Letters* **2023**.
79. Liu, J.; Zhang, J. Nanointerface Chemistry: Lattice-Mismatch-Directed Synthesis and Application of Hybrid Nanocrystals. *Chemical reviews* **2020,** *120,* 2123-2170.
80. Reiss, P.; Carayon, S.; Bleuse, J.; Pron, A. Low Polydispersity Core/Shell Nanocrystals of Cdse/Znse and Cdse/Znse/Zns Type: Preparation and Optical Studies. *Synthetic Metals* **2003,** *139,* 649-652.
81. Tinjod, F.; Gilles, B.; Moehl, S.; Kheng, K.; Mariette, H. Ii–Vi Quantum Dot Formation Induced by Surface Energy Change of a Strained Layer. *Applied Physics Letters* **2003,** *82,* 4340-4342.
82. Fitzmorris, B. C.; Cooper, J. K.; Edberg, J.; Gul, S.; Guo, J.; Zhang, J. Z. Synthesis and Structural, Optical, and Dynamic Properties of Core/Shell/Shell Cdse/Znse/Zns Quantum Dots. *The Journal of Physical Chemistry C* **2012,** *116,* 25065-25073.
83. Park, Y.-S.; Bae, W. K.; Padilha, L. A.; Pietryga, J. M.; Klimov, V. I. Effect of the Core/Shell Interface on Auger Recombination Evaluated by Single-Quantum-Dot Spectroscopy. *Nano letters* **2014,** *14,* 396-402.
84. Pinchetti, V.; Meinardi, F.; Camellini, A.; Sirigu, G.; Christodoulou, S.; Bae, W. K.; De Donato, F.; Manna, L.; Zavelani-Rossi, M.; Moreels, I.; Klimov, V. I.; Brovelli, S. Effect of Core/Shell Interface on Carrier Dynamics and Optical Gain Properties of Dual-Color Emitting Cdse/Cds Nanocrystals. *ACS Nano* **2016,** *10,* 6877-6887.
85. Park, Y.-S.; Bae, W. K.; Baker, T.; Lim, J.; Klimov, V. I. Effect of Auger Recombination on Lasing in Heterostructured Quantum Dots with Engineered Core/Shell Interfaces. *Nano Letters* **2015,** *15,* 7319-7328.
86. Park, Y.-S.; Bae, W. K.; Pietryga, J. M.; Klimov, V. I. Auger Recombination of Biexcitons and Negative and Positive Trions in Individual Quantum Dots. *ACS Nano* **2014,** *8,* 7288-7296.
87. Lim, J.; Jeong, B. G.; Park, M.; Kim, J. K.; Pietryga, J. M.; Park, Y. S.; Klimov, V. I.; Lee, C.; Lee, D. C.; Bae, W. K. Influence of Shell Thickness on the Performance of Light-Emitting Devices Based on Cdse/Zn1-Xcdxs Core/Shell Heterostructured Quantum Dots. *Advanced Materials* **2014,** *26,* 8034-8040.
88. Fedin, I.; Goryca, M.; Liu, D.; Tretiak, S.; Klimov, V. I.; Crooker, S. A. Enhanced Emission from Bright Excitons in Asymmetrically Strained Colloidal Cdse/Cdxzn1–Xse Quantum Dots. *ACS Nano* **2021,** *15,* 14444-14452.

89. Ahn, N.; Park, Y. S.; Livache, C.; Du, J.; Gungor, K.; Kim, J.; Klimov, V. I. Optically Excited Lasing in a Cavity-Based, High-Current-Density Quantum Dot Electroluminescent Device. *Advanced Materials* **2023,** *35,* 2206613.
90. Cragg, G. E.; Efros, A. L. Suppression of Auger Processes in Confined Structures. *Nano letters* **2010,** *10,* 313-317.
91. Simon, S. H. *The Oxford Solid State Basics*; OUP Oxford: 2013.
92. Won, Y.-H.; Cho, O.; Kim, T.; Chung, D.-Y.; Kim, T.; Chung, H.; Jang, H.; Lee, J.; Kim, D.; Jang, E. Highly Efficient and Stable Inp/Znse/Zns Quantum Dot Light-Emitting Diodes. *Nature* **2019,** *575,* 634-638.
93. Cao, W.; Xiang, C.; Yang, Y.; Chen, Q.; Chen, L.; Yan, X.; Qian, L. Highly Stable Qleds with Improved Hole Injection Via Quantum Dot Structure Tailoring. *Nature communications* **2018,** *9,* 2608.
94. Sun, Y.; Su, Q.; Zhang, H.; Wang, F.; Zhang, S.; Chen, S. Investigation on Thermally Induced Efficiency Roll-Off: Toward Efficient and Ultrabright Quantum-Dot Light-Emitting Diodes. *ACS nano* **2019,** *13,* 11433-11442.
95. McArthur, E. A.; Morris-Cohen, A. J.; Knowles, K. E.; Weiss, E. A. Charge Carrier Resolved Relaxation of the First Excitonic State in Cdse Quantum Dots Probed with near-Infrared Transient Absorption Spectroscopy. *The Journal of Physical Chemistry B* **2010,** *114,* 14514-14520.
96. Wang, L.; Lv, Y.; Lin, J.; Zhao, J.; Liu, X.; Zeng, R.; Wang, X.; Zou, B. Surface Organic Ligand-Passivated Quantum Dots: Toward High-Performance Light-Emitting Diodes with Long Lifetimes. *Journal of Materials Chemistry C* **2021,** *9,* 2483-2490.
97. Lee, S. H.; Kitano, K.; Doe, T.; Iwata, N.; Izumi, M.; Arakawa, Y.; Tatsuma, T. Fluoride Ligand Exchange for Quantum Dot Light-Emitting Diodes with Improved Efficiency and Stability. *Applied Physics Letters* **2022,** *121,* 231105.
98. Li, X.; Zhao, Y.-B.; Fan, F.; Levina, L.; Liu, M.; Quintero-Bermudez, R.; Gong, X.; Quan, L. N.; Fan, J.; Yang, Z. Bright Colloidal Quantum Dot Light-Emitting Diodes Enabled by Efficient Chlorination. *Nature Photonics* **2018,** *12,* 159-164.
99. Zhang, H.; Jang, J.; Liu, W.; Talapin, D. V. Colloidal Nanocrystals with Inorganic Halide, Pseudohalide, and Halometallate Ligands. *ACS nano* **2014,** *8,* 7359-7369.
100. Yun, H. J.; Paik, T.; Edley, M. E.; Baxter, J. B.; Murray, C. B. Enhanced Charge Transfer Kinetics of Cdse Quantum Dot-Sensitized Solar Cell by Inorganic Ligand Exchange Treatments. *ACS applied materials & interfaces* **2014,** *6,* 3721-3728.
101. Schnitzenbaumer, K. J.; Dukovic, G. Comparison of Phonon Damping Behavior in Quantum Dots Capped with Organic and Inorganic Ligands. *Nano letters* **2018,** *18,* 3667-3674.
102. Davidson-Hall, T.; Aziz, H. Significant Enhancement in Quantum Dot Light-Emitting Device Stability Via a Cascading Hole Transport Layer. *ACS applied materials & interfaces* **2020,** *12,* 16782-16791.
103. Rhee, S.; Chang, J. H.; Hahm, D.; Jeong, B. G.; Kim, J.; Lee, H.; Lim, J.; Hwang, E.; Kwak, J.; Bae, W. K. Tailoring the Electronic Landscape of Quantum Dot Light-Emitting Diodes for High Brightness and Stable Operation. *Acs Nano* **2020,** *14,* 17496-17504.
104. Chen, H.; Ding, K.; Fan, L.; Liu, W.; Zhang, R.; Xiang, S.; Zhang, Q.; Wang, L. All-Solution-Processed Quantum Dot Light Emitting Diodes Based on Double Hole Transport Layers by Hot Spin-Coating with Highly Efficient and Low Turn-on Voltage. *ACS applied materials & interfaces* **2018,** *10,* 29076-29082.

105. Zhu, B.; Ji, W.; Duan, Z.; Sheng, Y.; Wang, T.; Yuan, Q.; Zhang, H.; Tang, X.; Zhang, H. Low Turn-on Voltage and Highly Bright Ag–in–Zn–S Quantum Dot Light-Emitting Diodes. *Journal of Materials Chemistry C* **2018,** *6,* 4683-4690.
106. Kathirgamanathan, P.; Kumaraverl, M.; Bramananthan, N.; Ravichandran, S. High Efficiency and Highly Saturated Red Emitting Inverted Quantum Dot Devices (Qleds): Optimisation of Their Efficiencies with Low Temperature Annealed Sol–Gel Derived Zno as the Electron Transporter and a Novel High Mobility Hole Transporter and Thermal Annealing of the Devices. *Journal of Materials Chemistry C* **2018,** *6,* 11622-11644.
107. Ding, K.; Chen, H.; Fan, L.; Wang, B.; Huang, Z.; Zhuang, S.; Hu, B.; Wang, L. Polyethylenimine Insulativity-Dominant Charge-Injection Balance for Highly Efficient Inverted Quantum Dot Light-Emitting Diodes. *ACS applied materials & interfaces* **2017,** *9,* 20231-20238.
108. Ji, W.; Lv, Y.; Jing, P.; Zhang, H.; Wang, J.; Zhang, H.; Zhao, J. Highly Efficient and Low Turn-on Voltage Quantum Dot Light-Emitting Diodes by Using a Stepwise Hole-Transport Layer. *ACS Applied Materials & Interfaces* **2015,** *7,* 15955-15960.
109. Ghorbani, A.; Chen, J.; Samaeifar, F.; Azadinia, M.; Chun, P.; Lyu, Q.; Cotella, G.; Aziz, H. Stability Improvement in Quantum-Dot Light-Emitting Devices Via a New Robust Hole Transport Layer. *The Journal of Physical Chemistry C* **2022,** *126,* 18144-18151.
110. Cho, S.-Y.; Oh, N.; Nam, S.; Jiang, Y.; Shim, M. Enhanced Device Lifetime of Double-Heterojunction Nanorod Light-Emitting Diodes. *Nanoscale* **2017,** *9,* 6103-6110.
111. Li, Y.; Fan, X.; Shen, C.; Shi, X.; Li, P.; Hui, K. N.; Fan, J.; Kang, K.; Zhang, T.; Qian, L. Charge Balance in Red Qleds for High Efficiency and Stability Via Ionic Liquid Doping. *Advanced Functional Materials* **2022,** 2203641.
112. Ashrafi, A.; Jagadish, C. Review of Zincblende Zno: Stability of Metastable Zno Phases. *Journal of Applied Physics* **2007,** *102,* 4.
113. Jiang, J.; Olsen, J.; Gerward, L.; Frost, D.; Rubie, D.; Peyronneau, J. Structural Stability in Nanocrystalline Zno. *Europhysics Letters* **2000,** *50,* 48.
114. Fu, Y.; Jiang, W.; Kim, D.; Lee, W.; Chae, H. Highly Efficient and Fully Solution-Processed Inverted Light-Emitting Diodes with Charge Control Interlayers. *ACS applied materials & interfaces* **2018,** *10,* 17295-17300.
115. Li, Z. Enhanced Performance of Quantum Dots Light-Emitting Diodes: The Case of Al2o3 Electron Blocking Layer. *Vacuum* **2017,** *137,* 38-41.
116. Jin, H.; Moon, H.; Lee, W.; Hwangbo, H.; Yong, S. H.; Chung, H. K.; Chae, H. Charge Balance Control of Quantum Dot Light Emitting Diodes with Atomic Layer Deposited Aluminum Oxide Interlayers. *RSC advances* **2019,** *9,* 11634-11640.
117. Kim, D.; Fu, Y.; Kim, S.; Lee, W.; Lee, K.-H.; Chung, H. K.; Lee, H.-J.; Yang, H.; Chae, H. Polyethylenimine Ethoxylated-Mediated All-Solution-Processed High-Performance Flexible Inverted Quantum Dot-Light-Emitting Device. *ACS nano* **2017,** *11,* 1982-1990.
118. Yuan, Y.; Xue, X.; Wang, T.; Chi, X.; Wang, R.; Ji, W. Polyethylenimine Modified Sol-Gel Zno Electron-Transporting Layers for Quantum-Dot Light-Emitting Diodes. *Organic Electronics* **2022,** *100,* 106393.
119. Alexandrov, A.; Zvaigzne, M.; Lypenko, D.; Nabiev, I.; Samokhvalov, P. Al-, Ga-, Mg-, or Li-Doped Zinc Oxide Nanoparticles as Electron Transport Layers for Quantum Dot Light-Emitting Diodes. *Scientific reports* **2020,** *10,* 1-11.
120. Lee, Y.; Jeong, B. G.; Roh, H.; Roh, J.; Han, J.; Lee, D. C.; Bae, W. K.; Kim, J. Y.; Lee, C. Enhanced Lifetime and Efficiency of Red Quantum Dot Light-Emitting Diodes with Y-Doped Zno

Sol–Gel Electron-Transport Layers by Reducing Excess Electron Injection. *Advanced Quantum Technologies* **2018,** *1,* 1700006.
121. Jing, J.; Lin, L.; Yang, K.; Hu, H.; Guo, T.; Li, F. Highly Efficient Inverted Quantum Dot Light-Emitting Diodes Employing Sol-Gel Derived Li-Doped Zno as Electron Transport Layer. *Organic Electronics* **2022,** *103,* 106466.
122. Chrzanowski, M.; Kuchowicz, M.; Szukiewicz, R.; Sitarek, P.; Misiewicz, J.; Podhorodecki, A. Enhanced Efficiency of Quantum Dot Light-Emitting Diode by Sol-Gel Derived Zn1-Xmgxo Electron Transport Layer. *Organic Electronics* **2020,** *80,* 105656.
123. Rana, N.; Chand, S.; Gathania, A. K. Band Gap Engineering of Zno by Doping with Mg. *Physica Scripta* **2015,** *90,* 085502.
124. Shan, F.; Kim, B.; Liu, G.; Liu, Z.; Sohn, J.; Lee, W.; Shin, B.; Yu, Y. Blueshift of near Band Edge Emission in Mg Doped Zno Thin Films and Aging. *Journal of Applied Physics* **2004,** *95,* 4772-4776.
125. Huang, K.; Tang, Z.; Zhang, L.; Yu, J.; Lv, J.; Liu, X.; Liu, F. Preparation and Characterization of Mg-Doped Zno Thin Films by Sol–Gel Method. *Applied Surface Science* **2012,** *258,* 3710-3713.
126. Yu, X.; Yu, X.; Yan, M.; Weng, T.; Chen, L.; Zhou, Y.; Wei, J. Lowering Oxygen Vacancies of Zno Nanorods Via Mg-Doping and Their Effect on Polymeric Diode Behavior. *Sensors and Actuators A: Physical* **2020,** *312,* 112163.
127. Singh, V.; Rath, C. Passivation of Native Defects of Zno by Doping Mg Detected through Various Spectroscopic Techniques. *RSC Advances* **2015,** *5,* 44390-44397.
128. Lee, Y.; Kim, H.-M.; Kim, J.; Jang, J. Remarkable Lifetime Improvement of Quantum-Dot Light Emitting Diodes by Incorporating Rubidium Carbonate in Metal-Oxide Electron Transport Layers. *Journal of Materials Chemistry C* **2019,** *7,* 10082-10091.
129. Zhang, W.; Zhang, Q.; Zhang, Y.; Li, F.; Chang, C.; Sun, H.; Yang, M.; Yanto, S.; Zhang, Z.; Yang, L. Cdse/Zns Quantum-Dot Light-Emitting Diodes with Spiro-Ometad as Buffer Layer. *IEEE Transactions on Electron Devices* **2019,** *66,* 4901-4906.
130. Jin, X.; Chang, C.; Zhao, W.; Huang, S.; Gu, X.; Zhang, Q.; Li, F.; Zhang, Y.; Li, Q. Balancing the Electron and Hole Transfer for Efficient Quantum Dot Light-Emitting Diodes by Employing a Versatile Organic Electron-Blocking Layer. *ACS applied materials & interfaces* **2018,** *10,* 15803-15811.
131. Kim, H.-M.; Cho, S.; Kim, J.; Shin, H.; Jang, J. Li and Mg Co-Doped Zinc Oxide Electron Transporting Layer for Highly Efficient Quantum Dot Light-Emitting Diodes. *ACS applied materials & interfaces* **2018,** *10,* 24028-24036.
132. Zhang, Q.; Gu, X.; Zhang, Q.; Jiang, J.; Jin, X.; Li, F.; Chen, Z.; Zhao, F.; Li, Q. Znmgo: Zno Composite Films for Fast Electron Transport and High Charge Balance in Quantum Dot Light Emitting Diodes. *Optical Materials Express* **2018,** *8,* 909-918.
133. Chen, M.; Chen, X.; Ma, W.; Sun, X.; Wu, L.; Lin, X.; Yang, Y.; Li, R.; Shen, D.; Chen, Y. Highly Stable Sno2-Based Quantum-Dot Light-Emitting Diodes with the Conventional Device Structure. *ACS nano* **2022**.
134. Liu, Y.; Wei, S.; Wang, G.; Tong, J.; Li, J.; Pan, D. Quantum-Sized Sno2 Nanoparticles with Upshifted Conduction Band: A Promising Electron Transportation Material for Quantum Dot Light-Emitting Diodes. *Langmuir* **2020,** *36,* 6605-6609.
135. Kim, H. Y.; Park, Y. J.; Kim, J.; Han, C. J.; Lee, J.; Kim, Y.; Greco, T.; Ippen, C.; Wedel, A.; Ju, B. K. Transparent Inp Quantum Dot Light-Emitting Diodes with Zro2 Electron Transport Layer and Indium Zinc Oxide Top Electrode. *Advanced Functional Materials* **2016,** *26,* 3454-3461.

136. Ji, W.; Jing, P.; Zhao, J.; Liu, X.; Wang, A.; Li, H. Inverted Cdse/Cds/Zns Quantum Dot Light Emitting Devices with Titanium Dioxide as an Electron-Injection Contact. *Nanoscale* **2013,** *5,* 3474-3480.
137. Goswami, M.; Adhikary, N. C.; Bhattacharjee, S. Effect of Annealing Temperatures on the Structural and Optical Properties of Zinc Oxide Nanoparticles Prepared by Chemical Precipitation Method. *Optik* **2018,** *158,* 1006-1015.
138. Brunner, K.; Van Dijken, A.; Börner, H.; Bastiaansen, J. J.; Kiggen, N. M.; Langeveld, B. M. Carbazole Compounds as Host Materials for Triplet Emitters in Organic Light-Emitting Diodes: Tuning the Homo Level without Influencing the Triplet Energy in Small Molecules. *Journal of the American Chemical Society* **2004,** *126,* 6035-6042.
139. Popovic, Z. D.; Aziz, H. In *Delayed Electroluminescence: A New Tool for Studies of Oled Fundamental Properties*, Organic Light-Emitting Materials and Devices IX, SPIE: 2005; pp 126-132.
140. Stolz, S.; Zhang, Y.; Lemmer, U.; Hernandez-Sosa, G.; Aziz, H. Degradation Mechanisms in Organic Light-Emitting Diodes with Polyethylenimine as a Solution-Processed Electron Injection Layer. *ACS applied materials & interfaces* **2017,** *9,* 2776-2785.
141. Shi, Y.-L.; Liang, F.; Hu, Y.; Zhuo, M.-P.; Wang, X.-D.; Liao, L.-S. High Performance Blue Quantum Dot Light-Emitting Diodes Employing Polyethylenimine Ethoxylated as the Interfacial Modifier. *Nanoscale* **2017,** *9,* 14792-14797.
142. Ye, Z.; Wong, M. Characteristics of Plasma-Fluorinated Zinc Oxide Thin-Film Transistors. *IEEE electron device letters* **2012,** *33,* 1147-1149.
143. Seo, J.-S.; Jeon, J.-H.; Hwang, Y. H.; Park, H.; Ryu, M.; Park, S.-H. K.; Bae, B.-S. Solution-Processed Flexible Fluorine-Doped Indium Zinc Oxide Thin-Film Transistors Fabricated on Plastic Film at Low Temperature. *Scientific reports* **2013,** *3,* 1-9.
144. Pandey, R.; Wie, C. H.; Lin, X.; Lim, J. W.; Kim, K. K.; Hwang, D. K.; Choi, W. K. Fluorine Doped Zinc Tin Oxide Multilayer Transparent Conducting Oxides for Organic Photovoltaic′ S Cells. *Solar Energy Materials and Solar Cells* **2015,** *134,* 5-14.
145. Ammaih, Y.; Hartiti, B.; Ridah, A.; Lfakir, A.; Soucase, B. M.; Thevenin, P. In *Effect of F-Doping on Structural, Electrical, and Optical Properties of Zno Thin Films for Optoelectronic Application*, 2016 International Renewable and Sustainable Energy Conference (IRSEC), IEEE: 2016; pp 208-211.
146. Choi, Y.-J.; Park, H.-H. A Simple Approach to the Fabrication of Fluorine-Doped Zinc Oxide Thin Films by Atomic Layer Deposition at Low Temperatures and an Investigation into the Growth Mode. *Journal of Materials Chemistry C* **2014,** *2,* 98-108.
147. Han, W.; Oh, S.; Lee, C.; Kim, J.; Park, H.-H. Zno Nanocrystal Thin Films for Quantum-Dot Light-Emitting Devices. *ACS Applied Nano Materials* **2020,** *3,* 7535-7542.
148. Choi, Y.-J.; Kang, K.-M.; Park, H.-H. Anion-Controlled Passivation Effect of the Atomic Layer Deposited Zno Films by F Substitution to O-Related Defects on the Electronic Band Structure for Transparent Contact Layer of Solar Cell Applications. *Solar Energy Materials and Solar Cells* **2015,** *132,* 403-409.
149. Polydorou, E.; Zeniou, A.; Tsikritzis, D.; Soultati, A.; Sakellis, I.; Gardelis, S.; Papadopoulos, T. A.; Briscoe, J.; Palilis, L. C.; Kennou, S. Surface Passivation Effect by Fluorine Plasma Treatment on Zno for Efficiency and Lifetime Improvement of Inverted Polymer Solar Cells. *Journal of Materials Chemistry A* **2016,** *4,* 11844-11858.
150. Lieberman, M. A.; Lichtenberg, A. J. *Principles of Plasma Discharges and Materials Processing*; John Wiley & Sons: 2005.

151. Chen, G.; Zhang, J.; Yang, S. Fabrication of Hydrophobic Fluorinated Amorphous Carbon Thin Films by an Electrochemical Route. *Electrochemistry communications* **2008,** *10,* 7-11.
152. Kim, H. H.; Lee, Y.; Lee, Y. J.; Jeong, J.; Yi, Y.; Park, C.; Yim, S.-Y.; Angadi, B.; Ko, K.-J.; Kang, J.-W. Realization of Excitation Wavelength Independent Blue Emission of Zno Quantum Dots with Intrinsic Defects. *ACS Photonics* **2020,** *7,* 723-734.
153. Xu, Y.; Bo, B.; Gao, X.; Qiao, Z. Passivation Effect on Zno Films by Sf6 Plasma Treatment. *Crystals* **2019,** *9,* 236.
154. Rodnyi, P.; Khodyuk, I. Optical and Luminescence Properties of Zinc Oxide. *Optics and Spectroscopy* **2011,** *111,* 776-785.
155. Pramanik, S.; Mukherjee, S.; Dey, S.; Mukherjee, S.; Das, S.; Ghosh, T.; Ghosh, P.; Nath, R.; Kuiri, P. K. Cooperative Effects of Zinc Interstitials and Oxygen Vacancies on Violet-Blue Photoluminescence of Zno Nanoparticles: Uv Radiation Induced Enhanced Latent Fingerprint Detection. *Journal of Luminescence* **2022,** *251,* 119156.
156. Sadaiyandi, K.; Kennedy, A.; Sagadevan, S.; Chowdhury, Z. Z.; Johan, M.; Bin, R.; Aziz, F. A.; Rafique, R. F.; Thamiz Selvi, R. Influence of Mg Doping on Zno Nanoparticles for Enhanced Photocatalytic Evaluation and Antibacterial Analysis. *Nanoscale research letters* **2018,** *13,* 1-13.
157. Würfel, U.; Neher, D.; Spies, A.; Albrecht, S. Impact of Charge Transport on Current–Voltage Characteristics and Power-Conversion Efficiency of Organic Solar Cells. *Nature communications* **2015,** *6,* 1-9.
158. Chung, D. S.; Lyu, Q.; Cotella, G. F.; Chun, P.; Aziz, H. Suppressing Degradation in Qleds Via Doping Zno Electron Transport Layer by Halides. *Advanced Optical Materials* **2023,** 2300686.
159. Ghosh, S.; Manna, L. The Many "Facets" of Halide Ions in the Chemistry of Colloidal Inorganic Nanocrystals. *Chemical reviews* **2018,** *118,* 7804-7864.
160. Rodríguez-Fernández, J.; Pérez-Juste, J.; Mulvaney, P.; Liz-Marzán, L. M. Spatially-Directed Oxidation of Gold Nanoparticles by Au (Iii)− Ctab Complexes. *The Journal of Physical Chemistry B* **2005,** *109,* 14257-14261.
161. Vogtenhuber, D.; Podloucky, R.; Redinger, J.; Hebenstreit, E. L.; Hebenstreit, W.; Diebold, U. Ab Initio and Experimental Studies of Chlorine Adsorption on the Rutile Tio 2 (110) Surface. *Physical Review B* **2002,** *65,* 125411.
162. Patrick, B.; Kamat, P. Photophysics and Photochemistry of Quantized Zno Colloids. *J. Phys. Chem* **1992,** *96,* 1423-1427.
163. Chung, D. S.; Aziz, H. In *Modulation in Charge Distribution Via Polyethylenimine-Incorporation into Zno Electron Transport Layer and Its Impact on Quantum-Dots Light Emitting Device Stability*, Organic and Hybrid Light Emitting Materials and Devices XXVI, SPIE: 2022; pp 23-28.
164. Luo, Y.; Aziz, H. Correlation between Triplet–Triplet Annihilation and Electroluminescence Efficiency in Doped Fluorescent Organic Light-Emitting Devices. *Advanced Functional Materials* **2010,** *20,* 1285-1293.
165. Jou, J.-H.; Kumar, S.; Singh, M.; Chen, Y.-H.; Chen, C.-C.; Lee, M.-T. Carrier Modulation Layer-Enhanced Organic Light-Emitting Diodes. *Molecules* **2015,** *20,* 13005-13030.
166. Zhang, Z.; Guan, X.; Kang, Z.; Zhang, H.; Zeng, Q.; Yu, R.; Wang, R.; Ji, W. A Direct Evidence for the Energy Transfer from Phosphorescent Molecules to Quantum Dots in a Driving Light Emitting Diode. *Organic Electronics* **2019,** *73,* 337-341.
167. Huang, J.; Yin, Z.; Zheng, Q. Applications of Zno in Organic and Hybrid Solar Cells. *Energy & Environmental Science* **2011,** *4,* 3861-3877.

168. Chung, Y.; Kim, K. S.; Jung, J. W. On the Role of Carboxylated Polythiophene in Defect Passivation of Cspbi2br Surface for Efficient and Stable All-Inorganic Perovskite Solar Cells. *International Journal of Energy Research* **2021**.
169. Mandoc, M.; De Boer, B.; Paasch, G.; Blom, P. Trap-Limited Electron Transport in Disordered Semiconducting Polymers. *Physical Review B* **2007,** *75,* 193202.
170. Caglar, Y.; Caglar, M.; Ilican, S.; Yakuphanoglu, F. Thermally Stimulated Current and Space Charge Limited Current Mechanism in Film of the Gold/Zinc Oxide/Gold Type. *Physica B: Condensed Matter* **2007,** *392,* 99-103.
171. Shendre, S.; Sharma, V. K.; Dang, C.; Demir, H. V. Exciton Dynamics in Colloidal Quantum-Dot Leds under Active Device Operations. *ACS Photonics* **2018,** *5,* 480-486.
172. Rinehart, J. D.; Schimpf, A. M.; Weaver, A. L.; Cohn, A. W.; Gamelin, D. R. Photochemical Electronic Doping of Colloidal Cdse Nanocrystals. *Journal of the American Chemical Society* **2013,** *135,* 18782-18785.
173. Jha, P. P.; Guyot-Sionnest, P. Trion Decay in Colloidal Quantum Dots. *ACS nano* **2009,** *3,* 1011-1015.
174. Bozyigit, D.; Yarema, O.; Wood, V. Origins of Low Quantum Efficiencies in Quantum Dot Leds. *Advanced Functional Materials* **2013,** *23,* 3024-3029.
175. Rowland, C. E.; Susumu, K.; Stewart, M. H.; Oh, E.; Mäkinen, A. J.; O'Shaughnessy, T. J.; Kushto, G.; Wolak, M. A.; Erickson, J. S.; L. Efros, A. Electric Field Modulation of Semiconductor Quantum Dot Photoluminescence: Insights into the Design of Robust Voltage-Sensitive Cellular Imaging Probes. *Nano letters* **2015,** *15,* 6848-6854.
176. Szafran, B.; Chwiej, T.; Peeters, F. M.; Bednarek, S.; Adamowski, J.; Partoens, B. Exciton and Negative Trion Dissociation by an External Electric Field in Vertically Coupled Quantum Dots. *Physical Review B* **2005,** *71,* 205316.
177. Langton, N.; Matthews, D. The Dielectric Constant of Zinc Oxide over a Range of Frequencies. *British Journal of Applied Physics* **1958,** *9,* 453.
178. Casas Espínola, J.; Hernández Contreras, X. Effect of Dielectric Constant on Emission of Cdse Quantum Dots. *Journal of Materials Science: Materials in Electronics* **2017,** *28.*
179. Hughes, M. P.; Rosenthal, K. D.; Ran, N. A.; Seifrid, M.; Bazan, G. C.; Nguyen, T. Q. Determining the Dielectric Constants of Organic Photovoltaic Materials Using Impedance Spectroscopy. *Advanced Functional Materials* **2018,** *28,* 1801542.
180. Wang, A.; Fu, L.; Rao, T.; Cai, W.; Yuen, M.-F.; Zhong, J. Effect of Metal Ions on the Quenching of Photoluminescent Cdte Qds and Their Recovery. *Optical Materials* **2015,** *42,* 548-552.
181. Martil, I.; Redondo, E.; Ojeda, A. Influence of Defects on the Electrical and Optical Characteristics of Blue Light-Emitting Diodes Based on Iii–V Nitrides. *Journal of applied physics* **1997,** *81,* 2442-2444.
182. Zhang, L.; Zhu, L.; Li, X.; Xu, Z.; Wang, W.; Bai, X. Resistive Switching Mechanism in the One Diode-One Resistor Memory Based on P+-Si/N-Zno Heterostructure Revealed by in-Situ Tem. *Scientific Reports* **2017,** *7,* 45143.
183. Hippargi, G.; Mangrulkar, P.; Chilkalwar, A.; Labhsetwar, N.; Rayalu, S. Chloride Ion: A Promising Hole Scavenger for Photocatalytic Hydrogen Generation. *International Journal of Hydrogen Energy* **2018,** *43,* 6815-6823.
184. Iguchi, S.; Teramura, K.; Hosokawa, S.; Tanaka, T. Effect of the Chloride Ion as a Hole Scavenger on the Photocatalytic Conversion of Co 2 in an Aqueous Solution over Ni–Al Layered Double Hydroxides. *Physical Chemistry Chemical Physics* **2015,** *17,* 17995-18003.

185. Arotsky, J.; Symons, M. Halogen Cations. *Quarterly Reviews, Chemical Society* **1962,** *16,* 282-297.
186. Smoleński, T.; Kazimierczuk, T.; Goryca, M.; Pacuski, W.; Kossacki, P. Fine Structure of an Exciton Coupled to a Single Fe 2+ Ion in a Cdse/Znse Quantum Dot. *Physical Review B* **2017,** *96,* 155411.
187. Burgelman, M.; Nollet, P.; Degrave, S. Modelling Polycrystalline Semiconductor Solar Cells. *Thin solid films* **2000,** *361,* 527-532.
188. Lee, S.; Park, S. M.; Jung, E. D.; Zhu, T.; Pina, J. M.; Anwar, H.; Wu, F.-Y.; Chen, G.-L.; Dong, Y.; Cui, T. Dipole Engineering through the Orientation of Interface Molecules for Efficient Inp Quantum Dot Light-Emitting Diodes. *Journal of the American Chemical Society* **2022,** *144,* 20923-20930.
189. Shard, A. G. Detection Limits in Xps for More Than 6000 Binary Systems Using Al and Mg Kα X-Rays. *Surface and Interface Analysis* **2014,** *46,* 175-185.
190. Biesinger, M. C. Accessing the Robustness of Adventitious Carbon for Charge Referencing (Correction) Purposes in Xps Analysis: Insights from a Multi-User Facility Data Review. *Applied Surface Science* **2022,** 153681.
191. Zeng, C.; Ramos-Ruiz, A.; Field, J. A.; Sierra-Alvarez, R. Cadmium Telluride (Cdte) and Cadmium Selenide (Cdse) Leaching Behavior and Surface Chemistry in Response to Ph and O2. *Journal of Environmental Management* **2015,** *154,* 78-85.
192. Qu, X.; Liu, W.; Li, D.; Ma, J.; Gu, M.; Jia, S.; Xiang, G.; Sun, X. W. Does Interfacial Exciton Quenching Exist in High-Performance Quantum Dot Light-Emitting Diodes? *Nanoscale* **2023**.
193. Gerischer, H.; Mindt, W. The Mechanisms of the Decomposition of Semiconductors by Electrochemical Oxidation and Reduction. *Electrochimica Acta* **1968,** *13,* 1329-1341.
194. Diler, E.; Lescop, B.; Rioual, S.; Vien, G. N.; Thierry, D.; Rouvellou, B. Initial Formation of Corrosion Products on Pure Zinc and Mgzn2 Examinated by Xps. *Corrosion Science* **2014,** *79,* 83-88.
195. Feliu, S.; Barranco, V. Xps Study of the Surface Chemistry of Conventional Hot-Dip Galvanised Pure Zn, Galvanneal and Zn–Al Alloy Coatings on Steel. *Acta Materialia* **2003,** *51,* 5413-5424.
196. Nguyen, D. L. T.; Jee, M. S.; Won, D. H.; Jung, H.; Oh, H.-S.; Min, B. K.; Hwang, Y. J. Selective Co2 Reduction on Zinc Electrocatalyst: The Effect of Zinc Oxidation State Induced by Pretreatment Environment. *ACS Sustainable Chemistry & Engineering* **2017,** *5,* 11377-11386.
197. Greaney, M. J.; Couderc, E.; Zhao, J.; Nail, B. A.; Mecklenburg, M.; Thornbury, W.; Osterloh, F. E.; Bradforth, S. E.; Brutchey, R. L. Controlling the Trap State Landscape of Colloidal Cdse Nanocrystals with Cadmium Halide Ligands. *Chemistry of Materials* **2015,** *27,* 744-756.
198. Buin, A.; Comin, R.; Xu, J.; Ip, A. H.; Sargent, E. H. Halide-Dependent Electronic Structure of Organolead Perovskite Materials. *Chemistry of Materials* **2015,** *27,* 4405-4412.
199. Yao, Z.; Tang, K.; Xu, Z.; Ye, J.; Zhu, S.; Gu, S. The Luminescent Inhomogeneity and the Distribution of Zinc Vacancy-Related Acceptor-Like Defects in N-Doped Zno Microrods. *Nanoscale Research Letters* **2016,** *11,* 1-9.
200. Khanum, R.; Das, N. M.; Moirangthem, R. S. Defect Engineered Zno Whispering Gallery Modes Via Doping with Alkali Metal Ions for Label-Free Optical Sensors. *Journal of Applied Physics* **2019,** *125,* 173107.
201. Zhang, X.; Qin, J.; Hao, R.; Wang, L.; Shen, X.; Yu, R.; Limpanart, S.; Ma, M.; Liu, R. Carbon-Doped Zno Nanostructures: Facile Synthesis and Visible Light Photocatalytic Applications. *The Journal of Physical Chemistry C* **2015,** *119,* 20544-20554.

202. Chen, J.; Ghorbani, A.; Chung, D. S.; Azadinia, M.; Davidson-Hall, T.; Chun, P.; Lyu, Q.; Cotella, G.; Song, D.; Xu, Z.; Aziz, H. Influence of Encapsulation on the Efficiency and Positive Aging Behavior in Blue Quantum Dot Light-Emitting Devices. *ACS Applied Materials & Interfaces* **2023,** *15,* 34240-34248.
203. Zhao, B.; Tan, Z. a. Fluorescent Carbon Dots: Fantastic Electroluminescent Materials for Light-Emitting Diodes. *Advanced Science* **2021,** *8,* 2001977.
204. Li, X.; Gao, X.; Zhang, X.; Shen, X.; Lu, M.; Wu, J.; Shi, Z.; Colvin, V. L.; Hu, J.; Bai, X. Lead-Free Halide Perovskites for Light Emission: Recent Advances and Perspectives. *Advanced science* **2021,** *8,* 2003334.
205. Zhang, F.; Ma, Z.; Shi, Z.; Chen, X.; Wu, D.; Li, X.; Shan, C. Recent Advances and Opportunities of Lead-Free Perovskite Nanocrystal for Optoelectronic Application. *Energy Material Advances* **2021**.
206. Pan, J.; Li, X.; Gong, X.; Yin, J.; Zhou, D.; Sinatra, L.; Huang, R.; Liu, J.; Chen, J.; Dursun, I. Halogen Vacancies Enable Ligand-Assisted Self-Assembly of Perovskite Quantum Dots into Nanowires. *Angewandte Chemie International Edition* **2019,** *58,* 16077-16081.
207. Yakovlev, G.; Zubkov, V. Integration of Electrochemical Capacitance–Voltage Characteristics: A New Procedure for Obtaining Free Charge Carrier Depth Distribution Profiles with High Resolution. *Journal of Solid State Electrochemistry* **2021,** *25,* 797-802.
208. Kartopu, G.; Phillips, L. J.; Barrioz, V.; Irvine, S. J.; Hodgson, S. D.; Tejedor, E.; Dupin, D.; Clayton, A. J.; Rugen-Hankey, S. L.; Durose, K. Progression of Metalorganic Chemical Vapour-Deposited Cdte Thin-Film Pv Devices Towards Modules. *Progress in Photovoltaics: Research and Applications* **2016,** *24,* 283-291.
209. Ranga, P.; Rishinaramangalam, A.; Varley, J.; Bhattacharyya, A.; Feezell, D.; Krishnamoorthy, S. Si-Doped B-(Al0. 26ga0. 74) 2o3 Thin Films and Heterostructures Grown by Metalorganic Vapor-Phase Epitaxy. *Applied Physics Express* **2019,** *12,* 111004.
210. Miyashita, N.; Ahsan, N.; Okada, Y. Generation and Collection of Photocarriers in Dilute Nitride Gainnassb Solar Cells. *Progress in Photovoltaics: Research and Applications* **2016,** *24,* 28-37.
211. Maragliano, C.; Lilliu, S.; Dahlem, M. S.; Chiesa, M.; Souier, T.; Stefancich, M. Quantifying Charge Carrier Concentration in Zno Thin Films by Scanning Kelvin Probe Microscopy. *Scientific Reports* **2014,** *4,* 4203.
212. Look, D. C.; Reynolds, D. C.; Sizelove, J.; Jones, R.; Litton, C. W.; Cantwell, G.; Harsch, W. Electrical Properties of Bulk Zno. *Solid state communications* **1998,** *105,* 399-401.
213. Sun, Y.; Yan, X.; Zheng, X.; Liu, Y.; Shen, Y.; Zhang, Y. Influence of Carrier Concentration on the Resistive Switching Characteristics of a Zno-Based Memristor. *Nano Research* **2016,** *9,* 1116-1124.
214. Fan, Y.; Zheng, W.; Zhu, S.; Cheng, L.; Qi, H.; Li, L.; Huang, F. Extraction of Carrier Concentration and Mobility of Zno by Mid-Infrared Reflectance Spectroscopy. *Journal of Luminescence* **2021,** *239,* 118365.
215. Layek, A.; Manna, B.; Chowdhury, A. Carrier Recombination Dynamics through Defect States of Zno Nanocrystals: From Nanoparticles to Nanorods. *Chemical Physics Letters* **2012,** *539,* 133-138.
216. Chen, Z.; Su, Q.; Qin, Z.; Chen, S. Effect and Mechanism of Encapsulation on Aging Characteristics of Quantum-Dot Light-Emitting Diodes. *Nano Research* **2021,** *14,* 320-327.

217. Liu, D.; Cao, S.; Wang, S.; Wang, H.; Dai, W.; Zou, B.; Zhao, J.; Wang, Y. Highly Stable Red Quantum Dot Light-Emitting Diodes with Long T 95 Operation Lifetimes. *The journal of physical chemistry letters* **2020,** *11,* 3111-3115.
218. Noh, K.; Kim, M.; Lee, S.-H.; Yun, H.-S.; Lim, T.-H.; Choi, Y.; Kim, K.-J.; Jiang, Y.; Beom, K.; Kim, M. Effect of Ethanolamine Passivation of Zno Nanoparticles in Quantum Dot Light Emitting Diode Structure. *Current Applied Physics* **2019,** *19,* 998-1005.

Appendix A
Computation of Charge Trap Density

The carrier concentration of ZnO is extracted using a capacitance-voltage technique. For it, metal-insulator-semiconductor (MIS)-type device, as schematically depicted in Figure S1.1 (a), is fabricated in order : ITO glass substrate/ZnO/PMMA/Al. Carrier concentration, n_i, can be derived by the equation[8]

$$n_i(w) = \frac{2}{q \cdot \varepsilon_O \cdot \varepsilon_{ZnO} \cdot A^2 \cdot \frac{d(1/C^2)}{dV}} \tag{S1.1}$$

and depth, w, is[8]

$$w = \varepsilon_0 \cdot \varepsilon_{ZnO} \cdot A \cdot (\frac{1}{C_{ZnO}} - \frac{1}{C_{PMMA}}) \tag{S1.2}$$

where q, ε_0, ε_{ZnO}, *and* A are elementary charge, vacuum permittivity, dielectric constant of ZnO (10.5), and device area (4 mm^2, as shown in Figure 3.1 (a)), respectively. Figure S1.1 (b) shows calculated carrier concentration vs. depth (w, depletion width). The sudden increase in the large depth is a typical concentration profile of a thin-film device[207-210], which may be associated with the electrode contact. The depletion width, w, in the ZnO in this computation may be underestimated because of the dielectric constant value used in the calculation that may be deviated from that of nanoparticles. Nonetheless, the carrier concentration of ZnO is within the range of 2×10^{18} to 3×10^{18} cm^{-3}, within the range of values in the previous reports (10^{16}~10^{20} cm^{-3} based on synthesis and measurement methods[211-214]).

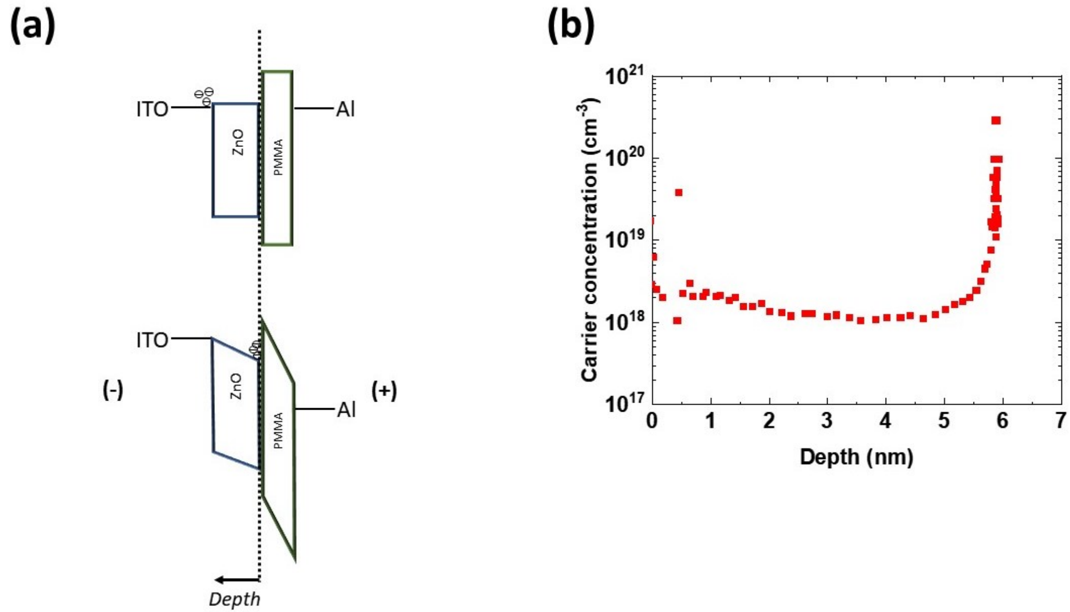

Figure S1.1 (a) Energy level diagram of the MIS-device used for the capacitance-voltage measurement in this experiment. (b) Calculated carrier concentration *vs.* depth of ZnO.

The trap density of QLED with ZnO and FZnO is computed using the current density below V_{th} shown in Figure 4.4 (b) and the equations from (4.1) to (4.3). For simplification of the computation, the SRH recombination coefficient, α_{SRH}, of both QLEDs are chosen to be 10^{-10} cm^3s^{-1}.[215] The intrinsic carrier density, n_i, is provided by the carrier concentration extracted above in Figure S1.1 and used for both ZnO- and FZnO-QLED. The trap densities of QLEDs with ZnO and FZnO *vs.* current density are plotted in Figure S1.2. The range of current density is below the V_{th} (i.e., 0 V~2.4 V), denoted in Figure 4.4 (b). As seen, FZnO-QLED shows lower trap density values than ZnO-QLED, indicating the reduction of trap states due to F-incorporation. The trap density values of both QLEDs are somewhat higher than the N_t values extracted by the EODs in Figure 5.5 (b) and equation (5.1). This probably is due to the difference in injection of holes between the full QLED structure *vs.* the EOD structure.

However, it is noteworthy that the extracted trap density values from both device structures are within a similar range, differing by only about an order of magnitude.

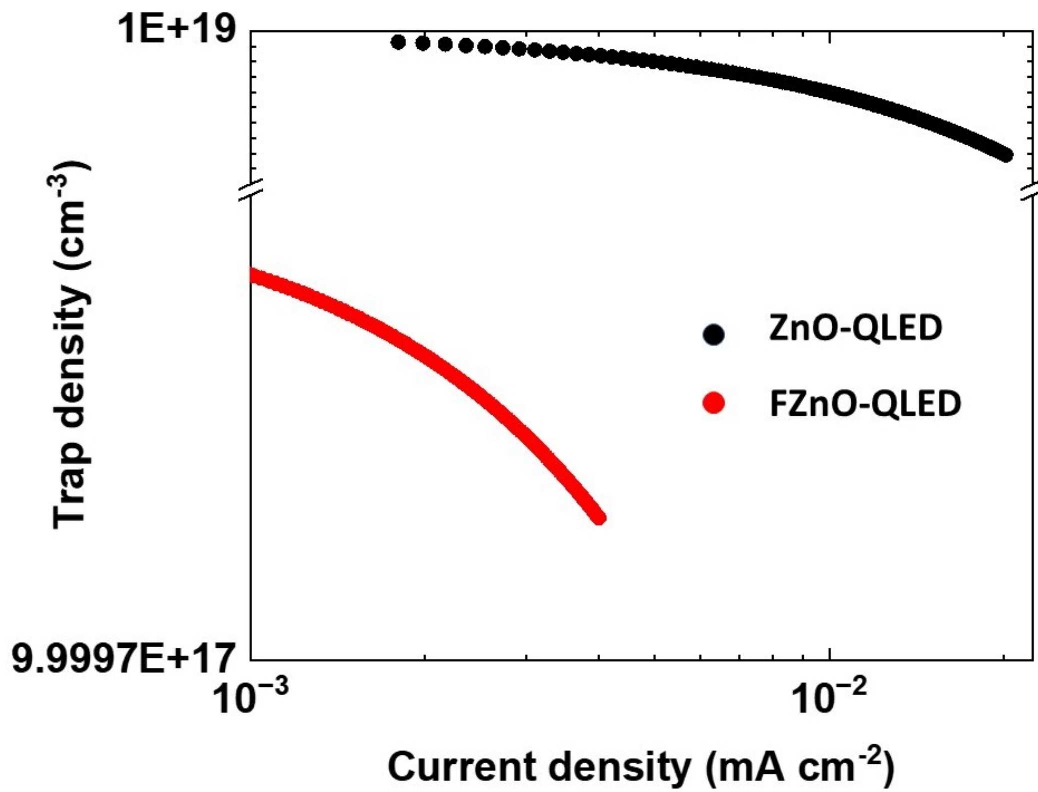

Figure S1.2 (a) Calculated trap density *vs.* current density of QLEDs with ZnO and FZnO.

Appendix B

Supplementary Information for Chapter 4

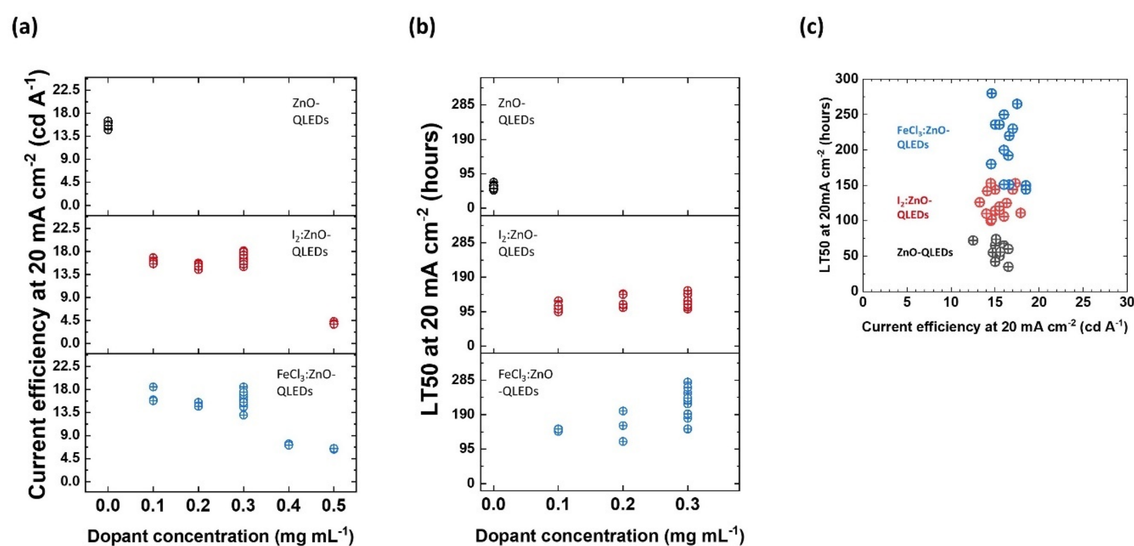

Figure S4.1 (a) Current efficiency and (b) LT50 at 20 mA cm^{-2} with various dopant concentrations, and (c) LT50 *vs.* current efficiency for each of 14 individual QLED in each group.

ETL	LT50 and L_0 at 20 mA cm^{-2}	LT50 for L_0 of 100 cd m^{-2}	Maximum EQE
ZnO	46 hours for 2,500 cd m^{-2}	15,100 hours	7.7 %
ZnO/PEI	62 hours for 3,030 cd m^{-2}	28,773 hours	11.2 %
ZnO:PEI (0.1 wt%)	140 hours for 3,000 cd m^{-2}	65,630 hours	11 %
ZnO:PEI (0.2 wt%)	101 hours for 3,050 cd m^{-2}	42,430 hours	13.8 %
ZnO:PEI (0.3 wt%)	292 hours for 3,250 cd m^{-2}	153,735 hours	12.1 %

Table S4.1 LT50 and EQE of QLEDs with different ETLs. LT50 projection for L_0=100 cd m^{-2} is calculated by lifetime relation equation (1.20). Acceleration factor n of 1.8 is used and LT50 is based on a measured value under 20 mA cm^{-2} of constant current.

ETL	QDs	HTL	Lifetime at L_0 of 100 cd m^{-2} (hours)	Reference
Fluorine:ZnO	CdSe/ZnS	CBP	LT50: 2,370,000	45
Mg:ZnO	CdSe/ZnS	TFB	LT50: 510,000	216
ZnLiMgO@MgO	CdZnSe/ZnS	TFB	N/A (LT95: 381,000)	217
Spiro-OMeTAD/ZnMgO	CdSe/ZnS	TFB	LT50: 24,400	129
TBS-PBO/ZnMgO	CdSe/CdS/ZnS	Poly-TPD	LT50: 70,000	130
Rb_2Co_3:ZnO	CdZnSeS/ZnS	TCTA	LT50: 11,000	128
PMMA/ZnO	CdSe/CdS	Poly-TPD	LT50: 420,000	21
PEI:ZnO	CdZnSe/ZnSe/CdZnS/ZnS	CBP	LT50: 154,000	46
Y:ZnO	CdSe/CdZnS	CBP	LT50: 3,700	120
Li:ZnO	CdSe/ZnS	TCTA/NPB	N/A (LT95: 11,000)	121
Ethanolamine:ZnO	CdSe/CdS/CdZnS	TFB	LT50: 2,000,000	218
SnO_2	CdSe/ZnS	TFB	N/A (LT95: 20,200)	133
TiO_2	CdSe/CdS/ZnS	CBP/TCTA	N/A (LT95: 0.3)	136

Table S4.2 Comparison of the stability performance of the QLEDs reported here with other highly stable devices with CdSe QDs via ETL modifications. LT50s not reported in the original work are estimated using equation (1.20) and an acceleration factor 1.8.

The abbreviations in Table S4.2

CBP: 4,4′-Bis(N-carbazolyl)-1,1′-biphenyl
TFB: Poly(9,9-dioctylfluorene-alt-N-(4-sec-butylphenyl)-diphenylamine)
ZnLiMgO@MgO: ZnLiMgO nanoparticles with magnesium oxide shells
Spiro-OMeTAD: 2,2',7,7'-Tetrakis(N,N-di(4-methoxyphenyl)amino)10-9,9'-spirobifluorene
TBS-PBO: tert-butyldimethylsilyl-poly(p-phenylene benzobisoxazole)
Poly-TPD: Poly(N,N′-bis(4-butylphenyl) -N,N′-bis(phenyl)-benzidine)
TCTA: tris(4-carbazoyl-9-ylphenyl)amine
PMMA: Poly(methyl methacrylate)
PEI: Polyethylenimine
NPB: N,N′-Di(1-naphthyl)-N,N′-diphenyl-(1,1′-biphenyl)-4,4′-diamine

Appendix C
Supplementary Information for Chapter 5

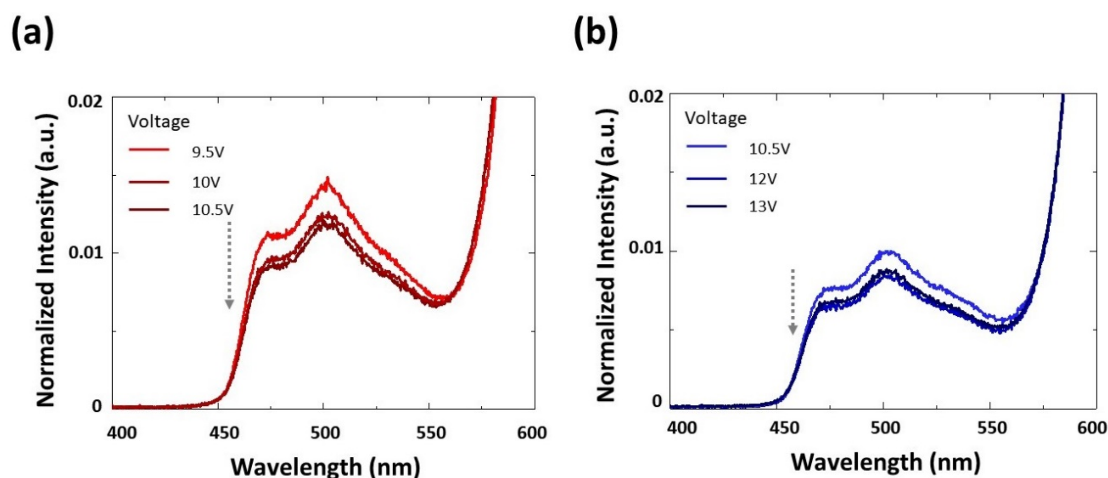

Figure S5.1 EL spectra from devices containing the CBP:FIrpic marking layer with (a) ZnO:$PEI_{0.1}$ ETL, and (b) ZnO:$PEI_{0.3}$ ETL, at higher forward bias voltages than in Figure 5.4 (e and f)

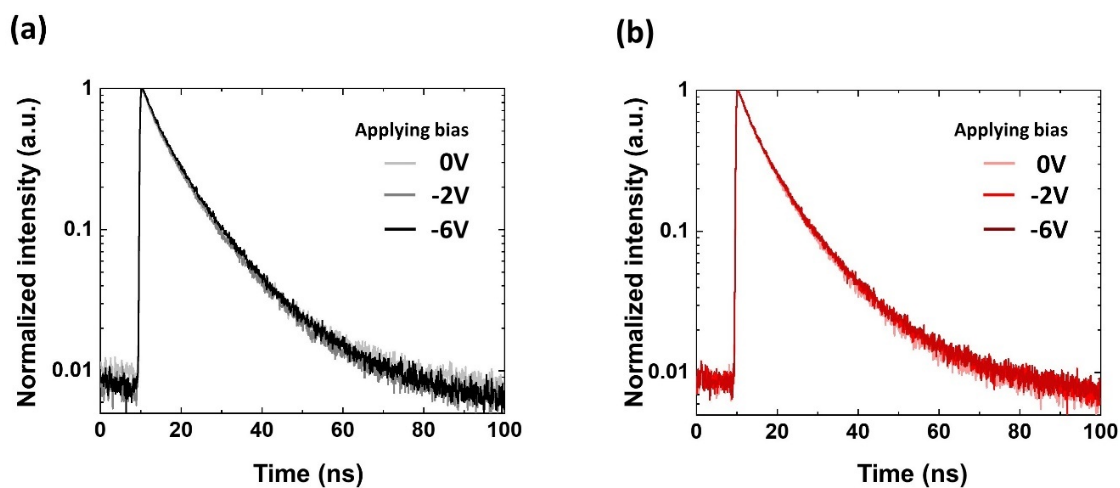

Figure S5.2 TRPL results of EODs with (a) ZnO and (b) FZnO with reverse bias.

	Bias	τ_1	A_1	τ_2	A_2	τ_3	A_3
ZnO-EOD	-6V	2.65	0.30	7.63	0.64	54.88	0.05
	-2V	2.63	0.32	9.22	0.65	52.66	0.05
	0V	2.77	0.31	8.78	0.66	55.94	0.04
	2V	2.81	0.31	7.99	0.66	56.32	0.03
	3V	2.90	0.33	8.95	0.65	58.77	0.03
	4V	3.04	0.35	9.02	0.62	53.35	0.04
	5V	3.06	0.35	9.11	0.62	53.53	0.05
	6V	3.17	0.34	9.55	0.62	52.75	0.05
FZnO-EOD	-6V	3.26	0.33	8.63	0.60	17.93	0.06
	-2V	3.21	0.37	9.22	0.62	27.21	0.02
	0V	3.19	0.43	9.33	0.57	79.62	0.02
	2V	3.02	0.39	8.51	0.60	69.29	0.02
	3V	2.81	0.33	8.56	0.65	63.56	0.03
	4V	2.87	0.35	8.86	0.62	55.88	0.04
	5V	2.90	0.35	9.05	0.62	59.5	0.05
	6V	3.08	0.34	9.45	0.62	64.05	0.05

Table S5.1 τ and A components extracted from the tri-exponential decay curves. The first two rows correspond to the measurement under reverse bias.

Appendix D

Supplementary Information for Chapter 6

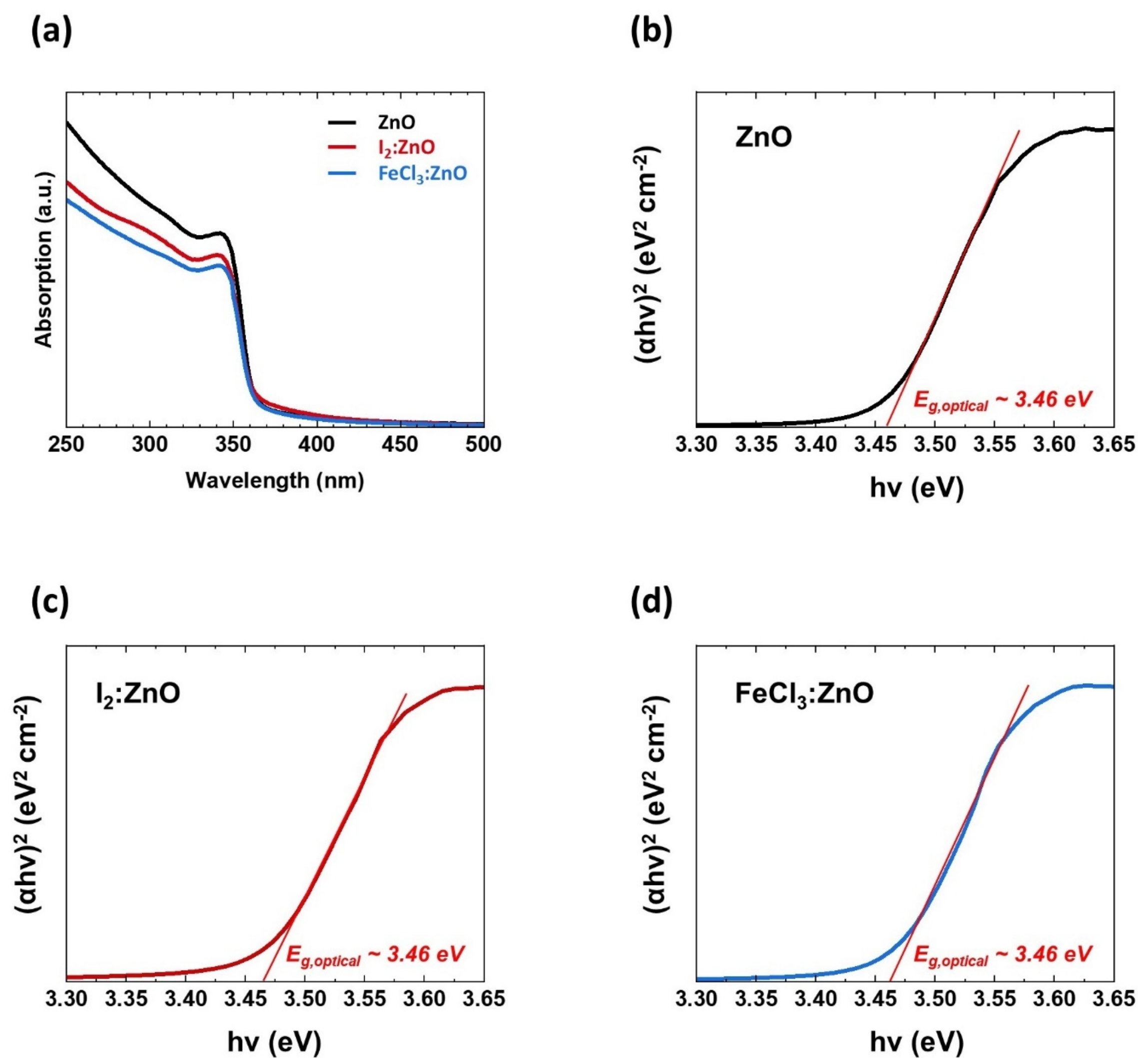

Figure S6.1 (a) UV-vis absorption spectra of ZnO, I_2:ZnO, and $FeCl_3$:ZnO films. Tauc plots of (b) ZnO, (c) I_2:ZnO, and (d) $FeCl_3$:ZnO films. The $E_{g,optical}$ is estimated from the extrapolated tangent lines of the linear parts on the Tauc plots.

(a)

	ZnO	QDs	CBP
Band gap (eV)	3.45	1.96	3.3
Electron affinity (eV)	4	4	2.3
Dielectric constant	10.5	6.2	3
Electron mobility ($cm^2 V^{-1} s^{-1}$)	2e-3	1e-4	3e-4
Hole mobility ($cm^2 V^{-1} s^{-1}$)	2e-4	1e-4	2e-3
Radiative recombination coefficient ($cm^3 s^{-1}$)	-	5e-11	-
Auger capture coefficient ($cm^6 s^{-1}$)	-	1e-26	-

(b)

	Defect parameter
Type	Donor
Energy level (eV, above Ev of ZnO)	1.2
Capture cross section electrons (cm^{-3})	-
Capture cross section holes (cm^{-3})	1e-15
Total density (cm^{-3})	0, 2e+17, 4e+17, 5.5e+17, 7e+17, 9e+17

Table S6.1 The values of the various parameters used in the SCAPS simulation for (a) ZnO ETL, QD EML, and CBP HTL, and (b) the dopants.